Analytic Model for Matched-filtered Scattered Intensity of Volume Inhomogeneities in an Ocean Waveguide Calibrated to Measured Seabed Reverberation

by

Anamaria Ignisca

Submitted to the Department of Mechanical Engineering
in partial fulfillment of the requirements for the degree of

Master of Science in Mechanical Engineering

at the

MASSACHUSETTS INSTITUTE OF TECHNOLOGY

June 2011

Author .....
Department of Mechanical Engineering
May 20, 2011

Certified by .....
Nicholas C. Makris
Professor of Mechanical Engineering
Thesis Supervisor

Accepted by .....
David E. Hardt
Graduate Officer, Department of Mechanical Engineering

Analytic Model for Matched-filtered Scattered Intensity of Volume Inhomogeneities in an Ocean Waveguide Calibrated to Measured Seabed Reverberation

by

Anamaria Ignisca

Submitted to the Department of Mechanical Engineering
on May 20, 2011, in partial fulfillment of the
requirements for the degree of
Master of Science in Mechanical Engineering

Abstract

In this thesis, we derive full theoretical expressions for the moments of the matched filtered scattered field due to volume inhomogeneities in an ocean waveguide and provide a computationally efficient time harmonic approximation to the matched filtered model. Following the approach developed by Galinde et al [6], the expressions are derived from first principles, by applying Green's theorem and the Born approximation. The scattered field and the total moment expressions are in terms of the fractional changes in the bottom compressibility and density, as well as the waveguide Green function and its gradients. The volume inhomogeneities are assumed to be statistically stationary, and assumed to be correlated in all three directions following a delta correlation function. Sound propagation in the ocean is modeled using the parabolic equation model and actual measurements of bathymetry and sound speed at the experimental locations. Monte Carlo simulations are used to account for the sound speed variability in the ocean waveguide due to internal waves or other sources of acoustic field randomization. The computationally efficient time-harmonic model is shown to provide a good approximation to the full broadband matched filtered model for a standard Pekeris waveguide. The time-harmonic model is then calibrated for ocean bottom reverberation at several frequencies in the 415-1325 Hz band, with data collected during the 2003 and 2006 ONR Geoclutter Experiments on the New Jersey continental shelf and on the northern flank of Georges Bank in the Gulf of Maine, respectively. The statistics for the inverted bottom parameters are summarized for all frequencies and experimental locations considered. The acoustically determined bottom parameters are shown to vary with approximately the wavelength cubed, suggesting that, by different frequencies selecting the scale of the acoustic inhomogeneities, the acoustic effects dominate over the geophysical effects.

Thesis Supervisor: Nicholas C. Makris
Title: Professor of Mechanical Engineering

Acknowledgments

I would like to thank my thesis advisor, Professor Nicholas C. Makris, for the support and guidance he offered on preparing this thesis and throughout my academic career at MIT. I am grateful for the lessons Professor Makris taught me and my fellow students not only in class, but also in the lab, through encouraging us to make progress one step at a time and to learn through discovery.

I would also like to thank Dr. Mark Andrews, Prof. Purnima Ratilal, and Hadi Tavakoli Nia for laying the ground work for the material in this thesis, and for the guidance and direction they offered at the onset of this endeavor.

To Geoff Fox, Leslie Regan and Joan Kravit I thank for their help with all the logistics related to preparing this thesis and completing my degree at MIT.

My colleagues and friends at MIT have also played a crucial role in the development of this work. Srinivasan Jagannathan, Ankita Deepak Jain, Dong Hoon Yi, Wenjun Zhang, Kalina Gospodinova, Audrey Maertens and Derya Akkaynak Yellin have always been there when I had questions related to acoustics or needed moral support.

Lastly, I would like to thank my parents, brother and husband for their love, support, and understanding.

Contents

List of Figures

List of Tables

Chapter 1

Introduction

The ability to accurately predict reverberation level in the ocean for different sediment types and frequency ranges is critical for remote sensing and imaging systems. The reverberation in shallow continental shelf environments for moderate sea surface wind conditions, has been shown to be mainly due to scattering from the ocean seabed [22], [19]. Several methods have been developed to model bottom scattering, including interface roughness scattering models, based on the roughness at the water-bottom interface [19], [21], [4], and volume scattering models, for scattering due to seabed volume inhomogeneities [6], [19], [23], [11], [12], [20]. For areas of relatively flat bathymetry and for the shallow grazing angles associated with low frequency long-range reverberation, it has been shown that volume scattering is the dominant factor in total bottom reverberation [17], [20], [10]. Models for scattering from volume inhomogeneities in the ocean seabed have been formulated in the literature, but have generally not included the matched filter, which is applied in remote sensing systems to "provide high-resolution imaging of the seafloor and submerged targets" [3]. The matched filter "allows for scatterers extending over multiple range resolution cells of the imaging system to be automatically localized in range, and does not require to artificially break-up the scatterers to within each range resolution cell, as in the case of time-harmonic or other broadband models" [1].

In this thesis, we derive full theoretical expressions for the moments of the matched filtered scattered field due to volume inhomogeneities and provide a computationally

efficient time harmonic approximation to the matched filtered model. Following the approach developed by Galinde et al [6], the expressions are derived from first principles, by applying Green's theorem and the Born approximation. The scattered field and the total moment expressions are in terms of the fractional changes in the bottom compressibility and density, as well as the waveguide Green function and its gradients. The volume inhomogeneities are assumed to be statistically stationary, and assumed to be correlated in all three directions following a delta correlation function. Sound propagation in the ocean is modeled using the parabolic equation model RAM [5], and actual measurements of bathymetry and sound speed at the experimental locations. Monte Carlo simulations are used to account for the sound speed variability in the ocean waveguide due to internal waves or other sources of acoustic field randomization. The computationally efficient time-harmonic model is shown to provide a good approximation to the full broadband matched filtered model for a standard Pekeris waveguide. The time-harmonic model is then calibrated for ocean bottom reverberation at several frequencies in the 415-1325 Hz band, with data collected during the 2003 and 2006 ONR Geoclutter Experiments on the New Jersey continental shelf and on the northern flank of Georges Bank in the Gulf of Maine, respectively [16], [15]. The statistics for the inverted bottom parameters are summarized for all frequencies and experimental locations considered.

This thesis is structured as follows: In Section 2, we present the analytic formulations for the moments of the matched filtered scattered field and a time harmonic approximation. In Section 3, we implement the matched filtered and time harmonic formulations to a standard Pekeris waveguide, using bottom parameters estimated by Galinde et al [6] for the New Jersey continental shelf. Here, we show that the time-harmonic model provides a good approximation to the matched filtered model and we investigate the frequency dependence of the time-harmonic model while keeping the bottom parameters constant. In Section 4, we calibrate the computationally efficient time-harmonic model to ocean reverberation data and present statistics for the inverted bottom parameters at several frequencies and at two different geographical locations.

Chapter 2

Analytic Formulation

In this section, we derive analytic expressions for the total moments of the matched filtered scattered field from random volume inhomogeneities extending over multiple resolution cells in range. We start by deriving the scattered field in terms of the single frequency f. We then apply the matched filter and use Fourier synthesis to obtain the time dependent matched filtered scattered field. Next, we derive full formulations for the total scattered field moments, and indicate that the matched filtered scattered intensity can be approximated by the incoherent term. We also provide a computationally efficient time harmonic approximation to the matched filtered scattered intensity.

We consider an ocean waveguide consisting of a water layer, located between an air halfspace above, and a bottom halfspace below. We let (x, y, z) be the coordinates of a cartesian coordinate system with origin at the air-water interface, and the z-axis pointing down. We place the source at $\mathbf{r}_0$=(x_0, y_0, z_0), the receiver at $\mathbf{r}$=(x, y, z), and the center of the inhomogeneity at $\mathbf{r}_t$=(x_t, y_t, z_t). f represents the frequency, $\omega = 2\pi f$ the angular frequency, c the sound speed, and $k = \omega/c$ is the acoustic wave number.

2.1 Matched filtered scattered field

To derive the matched filtered scattered field from random volume inhomogeneities, we follow the approach developed by Morse and Ingard [18] and Galinde et al [6], and start from the inhomogeneous Helmholtz equation for the single-frequency, time-independent acoustic field in the presence of volume inhomogeneities:

$$\begin{aligned}\nabla^2\Phi_t(\mathbf{r}_t, f) + k^2\Phi_t(\mathbf{r}_t, f) \\ = -k^2\Gamma_\kappa(\mathbf{r}_t)\Phi_t(\mathbf{r}_t, f) - \nabla \cdot [\Gamma_d(\mathbf{r}_t)\nabla\Phi_t(\mathbf{r}_t, f)].\end{aligned} \tag{2.1}$$

Here, Γ_κ is the fractional change in compressibility,

$$\Gamma_\kappa(\mathbf{r}_t) = \frac{\kappa(\mathbf{r}_t) - \bar{\kappa}}{\bar{\kappa}}, \tag{2.2}$$

and Γ_d is the fractional change in density,

$$\Gamma_d(\mathbf{r}_t) = \frac{d(\mathbf{r}_t) - \bar{d}}{d(\mathbf{r}_t)}, \tag{2.3}$$

where $\bar{\kappa}$ and $\bar{d}$ are the mean compressibility and density in the region, respectively [18], [6]. The compressibility can be expressed in terms of the density and the sound speed as $\kappa = 1/dc^2$.

Applying Green's theorem [18] to Equation 2.1 above, we obtain the scattered field $\Phi_S(\mathbf{r}_S|\mathbf{r}, \mathbf{r}_0, f)$ from inhomogeneities within V_S, a region which we choose to extend along the entire positive z-axis in depth, over the sonar resolution angle in azimuth, and over multiple sonar resolution cells in range. The region is centered at $\mathbf{r}_S$, and the source and receiver are located at $\mathbf{r}_0$ and $\mathbf{r}$, respectively:

$$\begin{aligned}\Phi_S(\mathbf{r}_S|\mathbf{r}, \mathbf{r}_0, f) = \iiint_{V_S} [k^2\Gamma_\kappa(\mathbf{r}_t)\Phi_t(\mathbf{r}_t, f)G(\mathbf{r}|\mathbf{r}_t, f) \\ + \Gamma_d(\mathbf{r}_t)\nabla\Phi_t(\mathbf{r}_t, f) \cdot \nabla G(\mathbf{r}|\mathbf{r}_t, f)]dV_t.\end{aligned} \tag{2.4}$$

$G(\mathbf{r}|\mathbf{r}_t, f)$ is the Green function describing propagation from the location of the

inhomogeneity to the receiver, and $\Phi_t(\mathbf{r}_t, f)$ is the total field at the location of the inhomogeneity. The total field can be expressed as the sum of the the incident and scattered fields [18],

$$\Phi_t(\mathbf{r}_t, f) = \Phi_i(\mathbf{r}_t|\mathbf{r}_0, f) + \Phi_S(\mathbf{r}_t, f).$$

To set the source level to 0 dB re 1 μPa at 1m, we let $\Phi_i(\mathbf{r}_t|\mathbf{r}_0, f) = (4\pi)G(\mathbf{r}_t|\mathbf{r}_0, f)$. For small fluctuations in density and compressibility, we can make the Born approximation, and approximate the total field at the inhomogeneity by the incident field [18]. Then, we can express the scattered field at the receiver as

$$\begin{aligned}\Phi_S(\mathbf{r}_S|\mathbf{r}, \mathbf{r}_0, f) =& (4\pi) \iiint_{V_S} [k^2 \Gamma_\kappa(\mathbf{r}_t) G(\mathbf{r}_t|\mathbf{r}_0, f) G(\mathbf{r}|\mathbf{r}_t, f) \\ &+ \Gamma_d(\mathbf{r}_t) \nabla G(\mathbf{r}_t|\mathbf{r}_0, f) \cdot \nabla G(\mathbf{r}|\mathbf{r}_t, f)] dV_t.\end{aligned} \tag{2.5}$$

Next, we derive the matched filtered scattered field for a source that transmits a broadband waveform $q(t)$ with Fourier transform $Q(f)$ and bandwidth B around the center frequency f_c by applying the matched filter to Equation 2.5. We express the matched filter, "a normalized replica of the original transmitted waveform" [3], as

$$H(f|t_M) = \frac{1}{\sqrt{E_0}} Q^*(f) e^{i2\pi f t_M}, \tag{2.6}$$

where t_M represents the time delay of the matched filter. The matched filter reaches a peak at $t = t_M$. The source energy is $E_0 = \int |Q(f)|^2 df$ and equals 1 for a normalized source. Then, using Fourier synthesis, we find the time-dependent matched filtered scattered field to be

$$\begin{aligned}\Phi_S(\mathbf{r}_S|\mathbf{r}, \mathbf{r}_0, t) = (4\pi) \int_{f_c - B/2}^{f_c + B/2} & \iiint_{V_S} [k^2 \Gamma_\kappa(\mathbf{r}_t) G(\mathbf{r}_t|\mathbf{r}_0, f) G(\mathbf{r}|\mathbf{r}_t, f) \\ &+ \Gamma_d(\mathbf{r}_t) \nabla G(\mathbf{r}_t|\mathbf{r}_0, f) \cdot \nabla G(\mathbf{r}|\mathbf{r}_t, f)] \\ &\times \frac{1}{\sqrt{E_0}} |Q(f)|^2 e^{-i2\pi f(t - t_M)} \, dV_t \, df.\end{aligned} \tag{2.7}$$

2.2 Full analytical expressions for the total moments of the matched filtered scattered field

Here, we derive full analytical expressions for the total moments of the matched filtered scattered field in terms of the statistical moments of fractional changes in compressibility and density and in terms of average realizations of the Green functions and gradients in a randomly fluctuating ocean waveguide. Implementation-friendly expressions for the total moments of the scattered field based on conditional moments, where we condition on a particular set of deterministic Green functions, are detailed in Appendix A of this thesis.

We assume the bottom inhomogeneities to vary randomly in space, following a stationary random process within the region V_S considered. Additionally, we assume the fluctuations in bottom properties to be independent from the fluctuations in the ocean waveguide. Thus, we can treat the random variables Γ_κ and Γ_d as independent from the medium's Green function [6]. Then, the mean matched filtered scattered field can be expressed as

$$\begin{aligned}\langle \Phi_S(\mathbf{r}_S|\mathbf{r},\mathbf{r}_0,t)\rangle = (4\pi)\int_{f_c-B/2}^{f_c+B/2}\iiint_{V_S}&[k^2\langle\Gamma_\kappa(\mathbf{r}_t)\rangle\langle G(\mathbf{r}_t|\mathbf{r}_0,f)G(\mathbf{r}|\mathbf{r}_t,f)\rangle \\ &+\langle\Gamma_d(\mathbf{r}_t)\rangle\langle\boldsymbol{\nabla}G(\mathbf{r}_t|\mathbf{r}_0,f)\cdot\boldsymbol{\nabla}G(\mathbf{r}|\mathbf{r}_t,f)\rangle] \\ &\times\frac{1}{\sqrt{E_0}}|Q(f)|^2e^{-i2\pi f(t-t_M)}\,dV_t\,df.\end{aligned} \tag{2.8}$$

The second moment of the scattered field is

$$\begin{aligned}
\langle|\Phi_S(\mathbf{r}_S|\mathbf{r},\mathbf{r}_0,t)|^2\rangle &= \langle\Phi_S(\mathbf{r}_S|\mathbf{r},\mathbf{r}_0,t_M)\Phi_S^*(\mathbf{r}_S|\mathbf{r},\mathbf{r}_0,t_M)\rangle \qquad (2.9)\\
&= \langle(4\pi)\int_{f_c-B/2}^{f_c+B/2}\iiint_{V_S}[k^2\Gamma_\kappa(\mathbf{r}_t)G(\mathbf{r}_t|\mathbf{r}_0,f)G(\mathbf{r}|\mathbf{r}_t,f)\\
&+\Gamma_d(\mathbf{r}_t)\nabla G(\mathbf{r}_t|\mathbf{r}_0,f)\cdot\nabla G(\mathbf{r}|\mathbf{r}_t,f)]\times\frac{1}{\sqrt{E_0}}|Q(f)|^2e^{-i2\pi f(t-t_M)}\,dV_t\,df\\
&\times(4\pi)\int_{f_c-B/2}^{f_c+B/2}\iiint_{V_S}[k'^2\Gamma_\kappa(\mathbf{r}_t')G^*(\mathbf{r}_t'|\mathbf{r}_0,f')G^*(\mathbf{r}|\mathbf{r}_t',f')\\
&+\Gamma_d(\mathbf{r}_t')\nabla G^*(\mathbf{r}_t'|\mathbf{r}_0,f')\cdot\nabla G^*(\mathbf{r}|\mathbf{r}_t',f')]\times\frac{1}{\sqrt{E_0}}|Q(f')|^2e^{-i2\pi f'(t-t_M)}\,dV_t'\,df'\rangle,
\end{aligned}$$

which can be written as

$$\begin{aligned}
&\langle|\Phi_S(\mathbf{r}_S|\mathbf{r},\mathbf{r}_0,t)|^2\rangle \qquad (2.10)\\
&= (4\pi)^2\int_{f_c-B/2}^{f_c+B/2}\int_{f_c-B/2}^{f_c+B/2}\iiint_{V_S}\iiint_{V_S}\\
&[k^2k'^2\langle\Gamma_\kappa(\mathbf{r}_t)\Gamma_\kappa(\mathbf{r}_t')\rangle\langle G(\mathbf{r}_t|\mathbf{r}_0,f)G(\mathbf{r}|\mathbf{r}_t,f)G^*(\mathbf{r}_t'|\mathbf{r}_0,f')G^*(\mathbf{r}|\mathbf{r}_t',f')\rangle\\
&+\langle\Gamma_d(\mathbf{r}_t)\Gamma_d(\mathbf{r}_t')\rangle\langle\nabla G(\mathbf{r}_t|\mathbf{r}_0,f)\cdot\nabla G(\mathbf{r}|\mathbf{r}_t,f)\times\nabla G^*(\mathbf{r}_t'|\mathbf{r}_0,f')\cdot\nabla G^*(\mathbf{r}|\mathbf{r}_t',f')\rangle\\
&+k^2\langle\Gamma_\kappa(\mathbf{r}_t)\Gamma_d(\mathbf{r}_t')\rangle\langle G(\mathbf{r}_t|\mathbf{r}_0,f)G(\mathbf{r}|\mathbf{r}_t,f)\nabla G^*(\mathbf{r}_t'|\mathbf{r}_0,f')\cdot\nabla G^*(\mathbf{r}|\mathbf{r}_t',f')\rangle\\
&+k'^2\langle\Gamma_\kappa(\mathbf{r}_t')\Gamma_d(\mathbf{r}_t)\rangle\langle G^*(\mathbf{r}_t'|\mathbf{r}_0,f')G^*(\mathbf{r}|\mathbf{r}_t',f')\nabla G(\mathbf{r}_t|\mathbf{r}_0,f)\cdot\nabla G(\mathbf{r}|\mathbf{r}_t,f)\rangle]\\
&\times\frac{1}{E_0}|Q(f)|^2|Q(f')|^2e^{-i2\pi(f-f')(t-t_M)}\,dV_t\,dV_t'\,df\,df'.
\end{aligned}$$

To model the statistics of the density and compressibility variations, we use a delta correlation function and assume the parameters to be correlated in all three dimensions. As we assume the parameters to follow a stationary random process, only the second order statistics are needed. Moreover, as the density and compressibility variations are assumed to be fully correlated [12], we may use only one coherence volume, V_C, for both random variables. Following the approach developed by Galinde

et al [6], we let

$$\begin{aligned}
&\langle \Gamma_\kappa(\mathbf{r}_t)\Gamma_\kappa(\mathbf{r}'_t)\rangle \qquad (2.11)\\
&\quad = V_c(\mathbf{r}_S, z_t)[\langle \Gamma^2_\kappa(\mathbf{r}_t)\rangle - |\langle \Gamma_\kappa(\mathbf{r}_t)\rangle|^2]\delta(\mathbf{r}_t - \mathbf{r}'_t) + \langle \Gamma_\kappa(\mathbf{r}_t)\rangle\langle \Gamma_\kappa(\mathbf{r}'_t)\rangle\\
&\quad = V_c(\mathbf{r}_S, z_t)\mathrm{Var}(\Gamma_\kappa(\mathbf{r}_t)\delta(\mathbf{r}_t - \mathbf{r}'_t) + \langle \Gamma_\kappa(\mathbf{r}_t)\rangle\langle \Gamma_\kappa(\mathbf{r}'_t)\rangle.
\end{aligned}$$

Similarly,

$$\begin{aligned}
&\langle \Gamma_d(\mathbf{r}_t)\Gamma_d(\mathbf{r}'_t)\rangle \qquad (2.12)\\
&\quad = V_c(\mathbf{r}_S, z_t)\mathrm{Var}(\Gamma_d(\mathbf{r}_t))\delta(\mathbf{r}_t - \mathbf{r}'_t) + \langle \Gamma_d(\mathbf{r}_t)\rangle\langle \Gamma_d(\mathbf{r}'_t)\rangle\\
&\langle \Gamma_\kappa(\mathbf{r}_t)\Gamma_d(\mathbf{r}'_t)\rangle \qquad (2.13)\\
&\quad = V_c(\mathbf{r}_S, z_t)\mathrm{Covar}(\Gamma_\kappa(\mathbf{r}_t), \Gamma_d(\mathbf{r}_t))\delta(\mathbf{r}_t - \mathbf{r}'_t) + \langle \Gamma_\kappa(\mathbf{r}_t)\rangle\langle \Gamma_d(\mathbf{r}'_t)\rangle\\
&\langle \Gamma_\kappa(\mathbf{r}'_t)\Gamma_d(\mathbf{r}_t)\rangle \qquad (2.14)\\
&\quad = V_c(\mathbf{r}_S, z_t)\mathrm{Covar}(\Gamma_\kappa(\mathbf{r}_t), \Gamma_d(\mathbf{r}_t))\delta(\mathbf{r}_t - \mathbf{r}'_t) + \langle \Gamma_\kappa(\mathbf{r}'_t)\rangle\langle \Gamma_d(\mathbf{r}_t)\rangle.
\end{aligned}$$

Then, Equation 2.10 becomes

$$\begin{aligned}
&\langle |\Phi_S(\mathbf{r}_S|\mathbf{r}, \mathbf{r}_0, t)|^2\rangle \qquad (2.15)\\
&= (4\pi)^2 \int_{f_c-B/2}^{f_c+B/2}\int_{f_c-B/2}^{f_c+B/2}\iiint_{V_S}\iiint_{V_S} V_c(\mathbf{r}_S, z_t)\\
&\quad \times [k^2k'^2\mathrm{Var}(\Gamma_\kappa)\delta(\mathbf{r}_t - \mathbf{r}'_t)\langle G(\mathbf{r}_t|\mathbf{r}_0, f)G(\mathbf{r}|\mathbf{r}_t, f)G^*(\mathbf{r}'_t|\mathbf{r}_0, f')G^*(\mathbf{r}|\mathbf{r}'_t, f')\rangle\\
&\quad + \mathrm{Var}(\Gamma_d)\delta(\mathbf{r}_t - \mathbf{r}'_t)\langle \nabla G(\mathbf{r}_t|\mathbf{r}_0, f)\cdot\nabla G(\mathbf{r}|\mathbf{r}_t, f)\times\nabla G^*(\mathbf{r}'_t|\mathbf{r}_0, f')\cdot\nabla G^*(\mathbf{r}|\mathbf{r}'_t, f')\rangle\\
&\quad + k^2\mathrm{Covar}(\Gamma_\kappa, \Gamma_d)\delta(\mathbf{r}_t - \mathbf{r}'_t)\langle G(\mathbf{r}_t|\mathbf{r}_0, f)G(\mathbf{r}|\mathbf{r}_t, f)\nabla G^*(\mathbf{r}'_t|\mathbf{r}_0, f')\cdot\nabla G^*(\mathbf{r}|\mathbf{r}'_t, f')\rangle\\
&\quad + k'^2\mathrm{Covar}(\Gamma_\kappa, \Gamma_d)\delta(\mathbf{r}_t - \mathbf{r}'_t)\langle G^*(\mathbf{r}'_t|\mathbf{r}_0, f')G^*(\mathbf{r}|\mathbf{r}'_t, f')\nabla G(\mathbf{r}_t|\mathbf{r}_0, f)\cdot\nabla G(\mathbf{r}|\mathbf{r}_t, f)\rangle]\\
&\quad \times \frac{1}{E_0}|Q(f)|^2|Q(f')|^2 e^{-i2\pi(f-f')(t-t_M)}\, dV_t\, dV'_t\, df\, df' +
\end{aligned}$$

$$
\begin{aligned}
&+ (4\pi)^2 \int_{f_c-B/2}^{f_c+B/2} \int_{f_c-B/2}^{f_c+B/2} \iiint_{V_S} \iiint_{V_S} \\
&\quad \times [k^2 k'^2 \langle \Gamma_\kappa(\mathbf{r}_t)\rangle \langle \Gamma_\kappa(\mathbf{r}'_t)\rangle \langle G(\mathbf{r}_t|\mathbf{r}_0, f) G(\mathbf{r}|\mathbf{r}_t, f) G^*(\mathbf{r}'_t|\mathbf{r}_0, f') G^*(\mathbf{r}|\mathbf{r}'_t, f')\rangle \\
&\quad + \langle \Gamma_d(\mathbf{r}_t)\rangle \langle \Gamma_d(\mathbf{r}'_t)\rangle \langle \nabla G(\mathbf{r}_t|\mathbf{r}_0, f) \cdot \nabla G(\mathbf{r}|\mathbf{r}_t, f) \times \nabla G^*(\mathbf{r}'_t|\mathbf{r}_0, f') \cdot \nabla G^*(\mathbf{r}|\mathbf{r}'_t, f')\rangle \\
&\quad + k^2 \langle \Gamma_\kappa(\mathbf{r}_t)\rangle \langle \Gamma_d(\mathbf{r}'_t)\rangle \langle G(\mathbf{r}_t|\mathbf{r}_0, f) G(\mathbf{r}|\mathbf{r}_t, f) \nabla G^*(\mathbf{r}'_t|\mathbf{r}_0, f') \cdot \nabla G^*(\mathbf{r}|\mathbf{r}'_t, f')\rangle \\
&\quad + k'^2 \langle \Gamma_\kappa(\mathbf{r}'_t)\rangle \langle \Gamma_d(\mathbf{r}_t)\rangle \langle G^*(\mathbf{r}'_t|\mathbf{r}_0, f') G^*(\mathbf{r}|\mathbf{r}'_t, f') \nabla G(\mathbf{r}_t|\mathbf{r}_0, f) \cdot \nabla G(\mathbf{r}|\mathbf{r}_t, f)\rangle] \\
&\quad \times \frac{1}{E_0} |Q(f)|^2 |Q(f')|^2 e^{-i2\pi(f-f')(t-t_M)} \, dV_t \, dV'_t \, df \, df'.
\end{aligned}
$$

After canceling the delta function with one of the volume integrals in the first term of the above equation, we have the full expression for the matched filtered total second moment

$$
\begin{aligned}
&\langle |\Phi_S(\mathbf{r}_S|\mathbf{r}, \mathbf{r}_0, t)|^2 \rangle \qquad (2.16) \\
&= (4\pi)^2 \int_{f_c-B/2}^{f_c+B/2} \int_{f_c-B/2}^{f_c+B/2} \iiint_{V_S} V_c(\mathbf{r}_S, z_t) \\
&\quad \times [k^2 k'^2 \mathrm{Var}(\Gamma_\kappa) \langle G(\mathbf{r}_t|\mathbf{r}_0, f) G(\mathbf{r}|\mathbf{r}_t, f) G^*(\mathbf{r}_t|\mathbf{r}_0, f') G^*(\mathbf{r}|\mathbf{r}_t, f')\rangle \\
&\quad + \mathrm{Var}(\Gamma_d) \langle \nabla G(\mathbf{r}_t|\mathbf{r}_0, f) \cdot \nabla G(\mathbf{r}|\mathbf{r}_t, f) \times \nabla G^*(\mathbf{r}_t|\mathbf{r}_0, f') \cdot \nabla G^*(\mathbf{r}|\mathbf{r}_t, f')\rangle \\
&\quad + k^2 \mathrm{Covar}(\Gamma_\kappa, \Gamma_d) \langle G(\mathbf{r}_t|\mathbf{r}_0, f) G(\mathbf{r}|\mathbf{r}_t, f) \nabla G^*(\mathbf{r}_t|\mathbf{r}_0, f') \cdot \nabla G^*(\mathbf{r}|\mathbf{r}_t, f')\rangle \\
&\quad + k'^2 \mathrm{Covar}(\Gamma_\kappa, \Gamma_d) \langle G^*(\mathbf{r}_t|\mathbf{r}_0, f') G^*(\mathbf{r}|\mathbf{r}_t, f') \nabla G(\mathbf{r}_t|\mathbf{r}_0, f) \cdot \nabla G(\mathbf{r}|\mathbf{r}_t, f)\rangle] \\
&\quad \times \frac{1}{E_0} |Q(f)|^2 |Q(f')|^2 e^{-i2\pi(f-f')(t-t_M)} \, dV_t \, df \, df' + \\
&+ (4\pi)^2 \int_{f_c-B/2}^{f_c+B/2} \int_{f_c-B/2}^{f_c+B/2} \iiint_{V_S} \iiint_{V_S} \\
&\quad \times [k^2 k'^2 \langle \Gamma_\kappa(\mathbf{r}_t)\rangle \langle \Gamma_\kappa(\mathbf{r}'_t)\rangle \langle G(\mathbf{r}_t|\mathbf{r}_0, f) G(\mathbf{r}|\mathbf{r}_t, f) G^*(\mathbf{r}'_t|\mathbf{r}_0, f') G^*(\mathbf{r}|\mathbf{r}'_t, f')\rangle \\
&\quad + \langle \Gamma_d(\mathbf{r}_t)\rangle \langle \Gamma_d(\mathbf{r}'_t)\rangle \langle \nabla G(\mathbf{r}_t|\mathbf{r}_0, f) \cdot \nabla G(\mathbf{r}|\mathbf{r}_t, f) \times \nabla G^*(\mathbf{r}'_t|\mathbf{r}_0, f') \cdot \nabla G^*(\mathbf{r}|\mathbf{r}'_t, f')\rangle \\
&\quad + k^2 \langle \Gamma_\kappa(\mathbf{r}_t)\rangle \langle \Gamma_d(\mathbf{r}'_t)\rangle \langle G(\mathbf{r}_t|\mathbf{r}_0, f) G(\mathbf{r}|\mathbf{r}_t, f) \nabla G^*(\mathbf{r}'_t|\mathbf{r}_0, f') \cdot \nabla G^*(\mathbf{r}|\mathbf{r}'_t, f')\rangle \\
&\quad + k'^2 \langle \Gamma_\kappa(\mathbf{r}'_t)\rangle \langle \Gamma_d(\mathbf{r}_t)\rangle \langle G^*(\mathbf{r}'_t|\mathbf{r}_0, f') G^*(\mathbf{r}|\mathbf{r}'_t, f') \nabla G(\mathbf{r}_t|\mathbf{r}_0, f) \cdot \nabla G(\mathbf{r}|\mathbf{r}_t, f)\rangle] \\
&\quad \times \frac{1}{E_0} |Q(f)|^2 |Q(f')|^2 e^{-i2\pi(f-f')(t-t_M)} \, dV_t \, dV'_t \, df \, df'.
\end{aligned}
$$

The total variance can be expressed in terms of the total second moment and the squared of the mean field as

$$\mathrm{Var}(\Phi_S(\mathbf{r}_S|\mathbf{r},\mathbf{r}_0,t)) = \langle|\Phi_S(\mathbf{r}_S|\mathbf{r},\mathbf{r}_0,t)|^2\rangle - |\langle\Phi_S(\mathbf{r}_S|\mathbf{r},\mathbf{r}_0,t)\rangle|^2, \tag{2.17}$$

which can be further expanded as

$$\begin{aligned}
&\mathrm{Var}(\Phi_S(\mathbf{r}_S|\mathbf{r},\mathbf{r}_0,t)) \qquad (2.18)\\
&= (4\pi)^2 \int_{f_c-B/2}^{f_c+B/2}\int_{f_c-B/2}^{f_c+B/2}\iiint_{V_S} V_c(\mathbf{r}_S,z_t)\\
&\quad\times[k^2k'^2\mathrm{Var}(\Gamma_\kappa)\langle G(\mathbf{r}_t|\mathbf{r}_0,f)G(\mathbf{r}|\mathbf{r}_t,f)G^*(\mathbf{r}_t|\mathbf{r}_0,f')G^*(\mathbf{r}|\mathbf{r}_t,f')\rangle\\
&\quad+\mathrm{Var}(\Gamma_d)\langle\nabla G(\mathbf{r}_t|\mathbf{r}_0,f)\cdot\nabla G(\mathbf{r}|\mathbf{r}_t,f)\times\nabla G^*(\mathbf{r}_t|\mathbf{r}_0,f')\cdot\nabla G^*(\mathbf{r}|\mathbf{r}_t,f')\rangle\\
&\quad+k^2\mathrm{Covar}(\Gamma_\kappa,\Gamma_d)\langle G(\mathbf{r}_t|\mathbf{r}_0,f)G(\mathbf{r}|\mathbf{r}_t,f)\nabla G^*(\mathbf{r}_t|\mathbf{r}_0,f')\cdot\nabla G^*(\mathbf{r}|\mathbf{r}_t,f')\rangle\\
&\quad+k'^2\mathrm{Covar}(\Gamma_\kappa,\Gamma_d)\langle G^*(\mathbf{r}_t|\mathbf{r}_0,f')G^*(\mathbf{r}|\mathbf{r}_t,f')\nabla G(\mathbf{r}_t|\mathbf{r}_0,f)\cdot\nabla G(\mathbf{r}|\mathbf{r}_t,f)\rangle]\\
&\quad\times\frac{1}{E_0}|Q(f)|^2|Q(f')|^2e^{-i2\pi(f-f')(t-t_M)}\,dV_t\,df\,df'+\\
&+(4\pi)^2\int_{f_c-B/2}^{f_c+B/2}\int_{f_c-B/2}^{f_c+B/2}\iiint_{V_S}\iiint_{V_S}\\
&\quad\times[k^2k'^2\langle\Gamma_\kappa(\mathbf{r}_t)\rangle\langle\Gamma_\kappa(\mathbf{r}'_t)\rangle\langle G(\mathbf{r}_t|\mathbf{r}_0,f)G(\mathbf{r}|\mathbf{r}_t,f)G^*(\mathbf{r}'_t|\mathbf{r}_0,f')G^*(\mathbf{r}|\mathbf{r}'_t,f')\rangle\\
&\quad+\langle\Gamma_d(\mathbf{r}_t)\rangle\langle\Gamma_d(\mathbf{r}'_t)\rangle\langle\nabla G(\mathbf{r}_t|\mathbf{r}_0,f)\cdot\nabla G(\mathbf{r}|\mathbf{r}_t,f)\times\nabla G^*(\mathbf{r}'_t|\mathbf{r}_0,f')\cdot\nabla G^*(\mathbf{r}|\mathbf{r}'_t,f')\rangle\\
&\quad+k^2\langle\Gamma_\kappa(\mathbf{r}_t)\rangle\langle\Gamma_d(\mathbf{r}'_t)\rangle\langle G(\mathbf{r}_t|\mathbf{r}_0,f)G(\mathbf{r}|\mathbf{r}_t,f)\nabla G^*(\mathbf{r}'_t|\mathbf{r}_0,f')\cdot\nabla G^*(\mathbf{r}|\mathbf{r}'_t,f')\rangle\\
&\quad+k'^2\langle\Gamma_\kappa(\mathbf{r}'_t)\rangle\langle\Gamma_d(\mathbf{r}_t)\rangle\langle G^*(\mathbf{r}'_t|\mathbf{r}_0,f')G^*(\mathbf{r}|\mathbf{r}'_t,f')\nabla G(\mathbf{r}_t|\mathbf{r}_0,f)\cdot\nabla G(\mathbf{r}|\mathbf{r}_t,f)\rangle]\\
&\quad\times\frac{1}{E_0}|Q(f)|^2|Q(f')|^2e^{-i2\pi(f-f')(t-t_M)}\,dV_t\,dV'_t\,df\,df'-
\end{aligned}$$

$$
\begin{aligned}
&- (4\pi)^2 \int_{f_c-B/2}^{f_c+B/2} \int_{f_c-B/2}^{f_c+B/2} \iiint_{V_S} \iiint_{V_S} \\
&\quad \times [k^2 k'^2 \langle \Gamma_\kappa(\mathbf{r}_t)\rangle \langle \Gamma_\kappa(\mathbf{r}'_t)\rangle \langle G(\mathbf{r}_t|\mathbf{r}_0, f) G(\mathbf{r}|\mathbf{r}_t, f)\rangle \langle G^*(\mathbf{r}'_t|\mathbf{r}_0, f') G^*(\mathbf{r}|\mathbf{r}'_t, f')\rangle \\
&\quad + \langle \Gamma_d(\mathbf{r}_t)\rangle \langle \Gamma_d(\mathbf{r}'_t)\rangle \langle \nabla G(\mathbf{r}_t|\mathbf{r}_0, f) \cdot \nabla G(\mathbf{r}|\mathbf{r}_t, f)\rangle \langle \nabla G^*(\mathbf{r}'_t|\mathbf{r}_0, f') \cdot \nabla G^*(\mathbf{r}|\mathbf{r}'_t, f')\rangle \\
&\quad + k^2 \langle \Gamma_\kappa(\mathbf{r}_t)\rangle \langle \Gamma_d(\mathbf{r}'_t)\rangle \langle G(\mathbf{r}_t|\mathbf{r}_0, f) G(\mathbf{r}|\mathbf{r}_t, f)\rangle \langle \nabla G^*(\mathbf{r}'_t|\mathbf{r}_0, f') \cdot \nabla G^*(\mathbf{r}|\mathbf{r}'_t, f')\rangle \\
&\quad + k'^2 \langle \Gamma_\kappa(\mathbf{r}'_t)\rangle \langle \Gamma_d(\mathbf{r}_t)\rangle \langle G^*(\mathbf{r}'_t|\mathbf{r}_0, f') G^*(\mathbf{r}|\mathbf{r}'_t, f')\rangle \langle \nabla G(\mathbf{r}_t|\mathbf{r}_0, f) \cdot \nabla G(\mathbf{r}|\mathbf{r}_t, f)\rangle] \\
&\quad \times \frac{1}{E_0} |Q(f)|^2 |Q(f')|^2 e^{-i2\pi(f-f')(t-t_M)} \, dV_t \, dV'_t \, df \, df'.
\end{aligned}
$$

While the above equation represents the full expression for the matched filtered total variance, we show in Section 3 that the last two terms of the variance Equation 2.18 are negligible, so that the variance can be approximated by the first term. Since the first two terms in the variance Equation 2.18 are the same as the terms of the second moment Equation 2.16, both the second moment, or matched filtered scattered intensity, and the variance, can then be approximated by

$$
\begin{aligned}
&\mathrm{Var}(\Phi_S(\mathbf{r}_S|\mathbf{r}, \mathbf{r}_0, t)) \qquad (2.19) \\
&\quad = (4\pi)^2 \int_{f_c-B/2}^{f_c+B/2} \int_{f_c-B/2}^{f_c+B/2} \iiint_{V_S} V_c(\mathbf{r}_S, z_t) \\
&\qquad \times [k^2 k'^2 \mathrm{Var}(\Gamma_\kappa) \langle G(\mathbf{r}_t|\mathbf{r}_0, f) G(\mathbf{r}|\mathbf{r}_t, f) G^*(\mathbf{r}_t|\mathbf{r}_0, f') G^*(\mathbf{r}|\mathbf{r}_t, f')\rangle \\
&\qquad + \mathrm{Var}(\Gamma_d) \langle \nabla G(\mathbf{r}_t|\mathbf{r}_0, f) \cdot \nabla G(\mathbf{r}|\mathbf{r}_t, f) \times \nabla G^*(\mathbf{r}_t|\mathbf{r}_0, f') \cdot \nabla G^*(\mathbf{r}|\mathbf{r}_t, f')\rangle \\
&\qquad + k^2 \mathrm{Covar}(\Gamma_\kappa, \Gamma_d) \langle G(\mathbf{r}_t|\mathbf{r}_0, f) G(\mathbf{r}|\mathbf{r}_t, f) \nabla G^*(\mathbf{r}_t|\mathbf{r}_0, f') \cdot \nabla G^*(\mathbf{r}|\mathbf{r}_t, f')\rangle \\
&\qquad + k'^2 \mathrm{Covar}(\Gamma_\kappa, \Gamma_d) \langle G^*(\mathbf{r}_t|\mathbf{r}_0, f') G^*(\mathbf{r}|\mathbf{r}_t, f') \nabla G(\mathbf{r}_t|\mathbf{r}_0, f) \cdot \nabla G(\mathbf{r}|\mathbf{r}_t, f)\rangle] \\
&\qquad \times \frac{1}{E_0} |Q(f)|^2 |Q(f')|^2 e^{-i2\pi(f-f')(t-t_M)} \, dV_t \, df \, df'.
\end{aligned}
$$

The equations presented above are expressed analytically in terms of the moments of the density and compressibility variations, as well as in terms of averages of Green function products over multiple realizations of the ocean environment. Implementation of the full second moment and variance formulations as expressed in Equations 2.16 and 2.18, respectively, requires, however, double integration over the volume V_S.

In Appendix A we develop a more efficient method for implementing the full formulations for the total variance and second moment, based on moments conditional on a set of deterministic Green functions.

2.3 Time harmonic approximation to the matched filtered scattered intensity

In this section, we present a computationally efficient approximation to the matched filtered scattered intensity derived in Section 2.2. Starting with Equation 2.5 for the time harmonic scattered field, where V_S now represents the resolution footprint of the imaging system, we following a procedure similar to the one used in the previous section, and find that the time harmonic total variance is

$$
\begin{aligned}
&\mathrm{Var}(\Phi_S(\mathbf{r}_S|\mathbf{r},\mathbf{r}_0,f)) \qquad (2.20)\\
&\quad = (4\pi)^2 \iiint_{V_S} V_c(\mathbf{r}_S,z_t)\\
&\qquad \times [k^4 \mathrm{Var}(\Gamma_\kappa)\langle |G(\mathbf{r}_t|\mathbf{r}_0,f)|^2 |G(\mathbf{r}|\mathbf{r}_t,f)|^2\rangle\\
&\qquad + \mathrm{Var}(\Gamma_d)\langle |\nabla G(\mathbf{r}_t|\mathbf{r}_0,f)\cdot\nabla G(\mathbf{r}|\mathbf{r}_t,f)|^2\rangle\\
&\qquad + k^2 \mathrm{Covar}(\Gamma_\kappa,\Gamma_d)\langle 2\Re\{G(\mathbf{r}_t|\mathbf{r}_0,f)G(\mathbf{r}|\mathbf{r}_t,f)\nabla G^*(\mathbf{r}_t|\mathbf{r}_0,f)\cdot\nabla G^*(\mathbf{r}|\mathbf{r}_t,f)\}\rangle] \, dV_t\\
&\quad + (4\pi)^2 \iiint_{V_S}\iiint_{V_S} [k^4\langle\Gamma_\kappa(\mathbf{r}_t)\rangle\langle\Gamma_\kappa(\mathbf{r}'_t)\rangle\langle G(\mathbf{r}_t|\mathbf{r}_0,f)G(\mathbf{r}|\mathbf{r}_t,f)G^*(\mathbf{r}'_t|\mathbf{r}_0,f)G^*(\mathbf{r}|\mathbf{r}'_t,f)\rangle\\
&\qquad + \langle\Gamma_d(\mathbf{r}_t)\rangle\langle\Gamma_d(\mathbf{r}'_t)\rangle\langle\nabla G(\mathbf{r}_t|\mathbf{r}_0,f)\cdot\nabla G(\mathbf{r}|\mathbf{r}_t,f)\times\nabla G^*(\mathbf{r}'_t|\mathbf{r}_0,f)\cdot\nabla G^*(\mathbf{r}|\mathbf{r}'_t,f)\rangle\\
&\qquad + k^2\langle\Gamma_\kappa(\mathbf{r}_t)\rangle\langle\Gamma_d(\mathbf{r}'_t)\rangle\langle G(\mathbf{r}_t|\mathbf{r}_0,f)G(\mathbf{r}|\mathbf{r}_t,f)\nabla G^*(\mathbf{r}'_t|\mathbf{r}_0,f)\cdot\nabla G^*(\mathbf{r}|\mathbf{r}'_t,f)\rangle\\
&\qquad + k^2\langle\Gamma_\kappa(\mathbf{r}'_t)\rangle\langle\Gamma_d(\mathbf{r}_t)\rangle\langle G^*(\mathbf{r}'_t|\mathbf{r}_0,f)G^*(\mathbf{r}|\mathbf{r}'_t,f)\nabla G(\mathbf{r}_t|\mathbf{r}_0,f)\cdot\nabla G(\mathbf{r}|\mathbf{r}_t,f)\rangle] \, dV_t \, dV'_t\\
&\quad - (4\pi)^2 \iiint_{V_S}\iiint_{V_S} [k^4\langle\Gamma_\kappa(\mathbf{r}_t)\rangle\langle\Gamma_\kappa(\mathbf{r}'_t)\rangle\langle G(\mathbf{r}_t|\mathbf{r}_0,f)G(\mathbf{r}|\mathbf{r}_t,f)\rangle\langle G^*(\mathbf{r}'_t|\mathbf{r}_0,f)G^*(\mathbf{r}|\mathbf{r}'_t,f)\rangle\\
&\qquad + \langle\Gamma_d(\mathbf{r}_t)\rangle\langle\Gamma_d(\mathbf{r}'_t)\rangle\langle\nabla G(\mathbf{r}_t|\mathbf{r}_0,f)\cdot\nabla G(\mathbf{r}|\mathbf{r}_t,f)\rangle\langle\nabla G^*(\mathbf{r}'_t|\mathbf{r}_0,f)\cdot\nabla G^*(\mathbf{r}|\mathbf{r}'_t,f)\rangle\\
&\qquad + k^2\langle\Gamma_\kappa(\mathbf{r}_t)\rangle\langle\Gamma_d(\mathbf{r}'_t)\rangle\langle G(\mathbf{r}_t|\mathbf{r}_0,f)G(\mathbf{r}|\mathbf{r}_t,f)\rangle\langle\nabla G^*(\mathbf{r}'_t|\mathbf{r}_0,f)\cdot\nabla G^*(\mathbf{r}|\mathbf{r}'_t,f)\rangle\\
&\qquad + k^2\langle\Gamma_\kappa(\mathbf{r}'_t)\rangle\langle\Gamma_d(\mathbf{r}_t)\rangle\langle G^*(\mathbf{r}'_t|\mathbf{r}_0,f)G^*(\mathbf{r}|\mathbf{r}'_t,f)\rangle\langle\nabla G(\mathbf{r}_t|\mathbf{r}_0,f)\cdot\nabla G(\mathbf{r}|\mathbf{r}_t,f)\rangle] \, dV_t \, dV'_t.
\end{aligned}
$$

In Section 3.1 we show, using Monte Carlo simulations in a standard Pekeris waveguide, that the matched filtered scattered intensity derived in Equation 2.19 can be approximated by the first term of the total time harmonic variance, also given by Galinde et al [6] as:

$$
\begin{aligned}
&\mathrm{Var}(\Phi_S(\mathbf{r}_S|\mathbf{r},\mathbf{r}_0,f)) \qquad (2.21)\\
&\quad = (4\pi)^2 \iiint_{V_S} V_c(\mathbf{r}_S,z_t)\\
&\qquad \times [k^4 \mathrm{Var}(\Gamma_\kappa)\langle |G(\mathbf{r}_t|\mathbf{r}_0,f)|^2 |G(\mathbf{r}|\mathbf{r}_t,f)|^2\rangle\\
&\qquad + \mathrm{Var}(\Gamma_d)\langle |\boldsymbol{\nabla} G(\mathbf{r}_t|\mathbf{r}_0,f)\cdot\boldsymbol{\nabla} G(\mathbf{r}|\mathbf{r}_t,f)|^2\rangle\\
&\qquad + k^2 \mathrm{Covar}(\Gamma_\kappa,\Gamma_d)\langle 2\Re\{G(\mathbf{r}_t|\mathbf{r}_0,f)G(\mathbf{r}|\mathbf{r}_t,f)\boldsymbol{\nabla} G^*(\mathbf{r}_t|\mathbf{r}_0,f)\cdot\boldsymbol{\nabla} G^*(\mathbf{r}|\mathbf{r}_t,f)\}\rangle]\, dV_t.
\end{aligned}
$$

Chapter 3

Model implementation for a Pekeris waveguide

In this section, we implement the theoretical formulations developed in Section 2 and Appendix A for the total moments of the scattered field to a standard sand Pekeris waveguide, using Monte Carlo simulations of the ocean environment. We show that the following three approximations can be made not only for multiple realizations, but also for a single realization of the ocean waveguide: (1) the total matched filtered second moment (Equation 2.16) is dominated by and can be approximated by the total matched filtered variance (Equation 2.18); (2) the total matched filtered variance (Equation 2.18) is dominated by and can be approximated by its first term (Equation 2.19), while the last two terms are negligible; (3) the first term of the total matched filtered variance (Equation 2.19) is dominated by and can be approximated by the first term of the total time harmonic variance (Equation 2.21). Lastly, we investigate the frequency dependence of the time harmonic model for the scattered intensity in an isovelocity sand Pekeris waveguide, while keeping the bottom parameters constant for all frequencies.

3.1 Approximations to the matched filtered scattered intensity

Here, we implement the formulations for the total moments of the scattered field to a Pekeris waveguide with sand bottom such as the one illustrated in Figure 3-1, and demonstrate that the three approximations stated above hold for any number of realizations of the ocean environment.

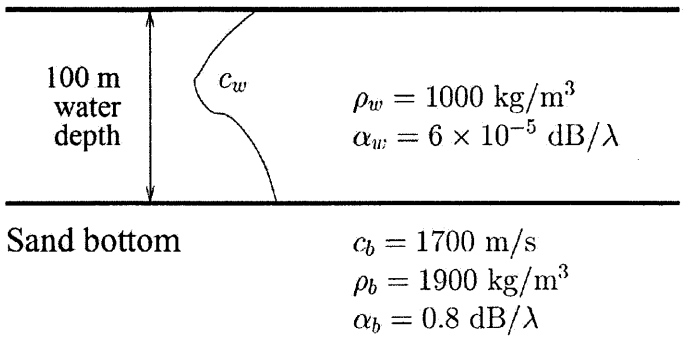

Figure 3-1: Pekeris waveguide with sand bottom, where c_w, ρ_w and α_w are the sound speed, density and attenuation of the water column, and c_b, ρ_b and α_b are those of the sea-bottom. The water column sound speed profiles used in simulations are actual sound speed profiles measured on the New Jersey continental shelf [16].

We allow the sound speed profiles to vary in range, in order to model the random fluctuations in the ocean environment caused by internal waves. From a set of sound speed profiles measured on the New Jersey continental shelf [16], we pick one sound speed profile every 500 m in range [2] and use the parabolic equation model RAM [5] to compute the Green functions for each randomly selected set of sound speed profiles. The set of measured sound speed profiles used for random selection is shown in Figure 3-2. The geometry of the problem is monostatic, with the source and receiver collocated at the depth of 50 m. The source and receiver comprise each of a single element. The source level is normalized to 0 dB re 1 μPa at 1 m and the waveform transmitted is a 1 second long linear frequency modulated (LFM) pulse centered at 415 Hz, with a 50 Hz bandwidth. The corresponding range resolution, Δr, is then 15 m, as $\Delta r = c/2B$, where c, the reference sound speed, is 1500 m/s, and B, the bandwidth, is 50 Hz. The statistics of the fractional changes in density

and compressibility used in the simulation are those estimated by Galinde et al [6] for the New Jersey continental shelf, summarized in Table 3.1. The region over which we integrate, V_S, corresponds to a seafloor patch that extends over 10m in depth (more than sufficient for convergence) and 3° in azimuth. In range, the patch extends from 100 m to 5500 m relative to the source/receiver location. The depth and range increments used for computing the Green functions and gradients are $dz = 0.4$ m and $dr = 3$ m, respectively. In azimuth, we assume the Green functions are constant over the integration angle.

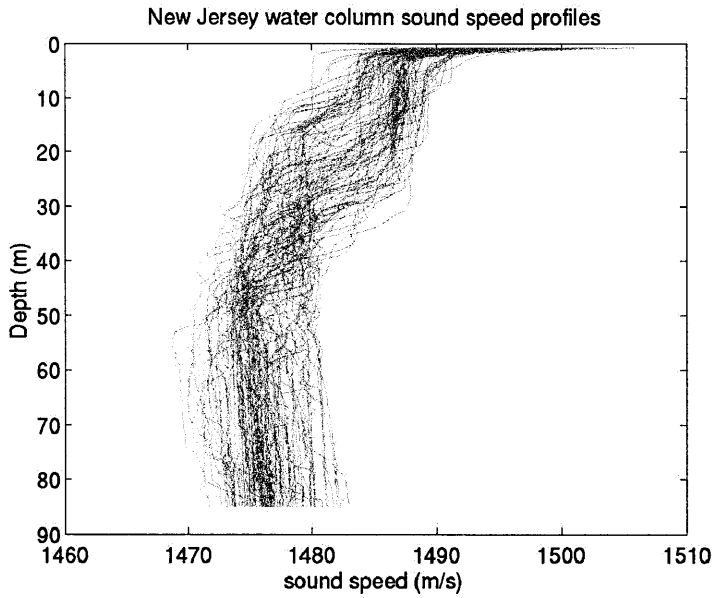

Figure 3-2: The sound speed profiles measured on the New Jersey continental shelf.

Table 3.1: Statistical geologic properties of the New Jersey Strataform, as estimated by Galinde et al [6].

Statistical parameters	Average values over the region
V_c	0.0030 (m^3)
$\langle \Gamma_k \rangle$	0.0000
$\langle \Gamma_d \rangle$	-0.0063
$\langle \Gamma_k^2 \rangle$	0.0083
$\langle \Gamma_d^2 \rangle$	0.0066
$\mathrm{Var}(\Gamma_k)$	0.0083
$\mathrm{Var}(\Gamma_d)$	0.0065
$\mathrm{Covar}(\Gamma_k, \Gamma_d)$	-0.0065

First, we show that the matched filtered scattered intensity is dominated by the incoherent intensity, or the variance. We implement the full expressions for the matched filtered total second moment, total variance and the magnitude squared of the total mean, as expressed in Equations A.12, A.14 and A.3, respectively, from Appendix A. These equations represent formulations for the scattered field moments alternative to those in Equations 2.16, 2.18 and 2.8 from Section 2: the former are formulations expressed in terms of moments conditional on a set of deterministic Green functions, while the latter are analytic formulations, expressed in terms of bottom parameter statistics and averages of Green function products over multiple realizations of the ocean environment. Equations A.12, A.14 and A.3, however, are more suitable for im-

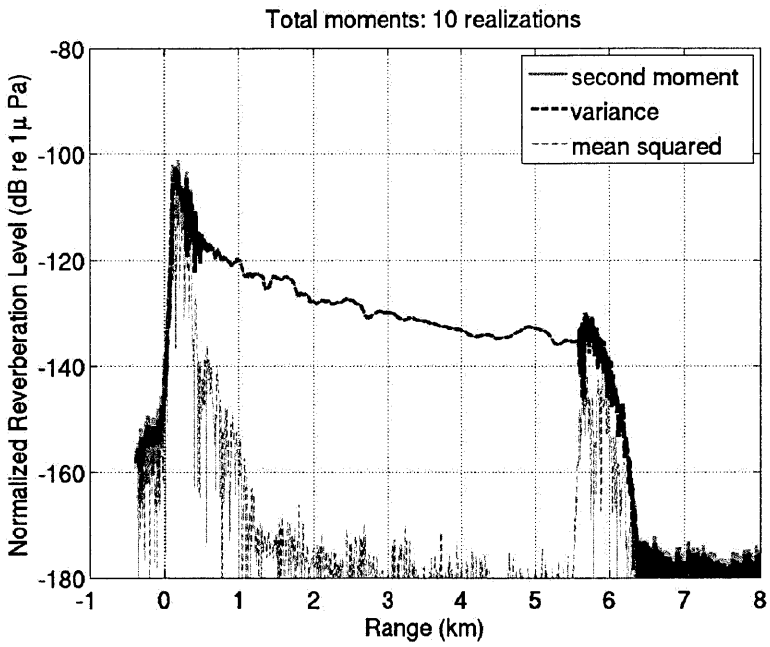

Figure 3-3: Total moments of the full 390-440 Hz matched filtered scattered field in a Pekeris sand waveguide with varying sound speed profiles, for 10 realizations of the ocean environment. The level of the mean squared term is dependent on the number of realizations and on the range increment dr, while the level of the variance term is stable.

plementation, since they don't require a double integration over the patch V_S. Figures 3-3 and 3-4 show the matched filtered moments for 10 and 1 realizations, respectively. Both figures show that, except at the edges of the patch, where the coherent intensity is non-negligible, the second moment, or scattered intensity is dominated by the

variance, or the incoherent intensity.

We note that the level of the coherent term, the mean squared, is dependent on the number of realizations and on the range increment dr, while the level of the incoherent term, the variance, is stable. For the latter, this implies that increasing the number of realizations renders a smoother curve, but one realization is sufficient to determine the correct level. For the case of one realization, in fact, the Green function is deterministic and the total moments are equal to the conditional moments described in Equations A.11, A.9 and A.2 for the second moment, variance and mean, respectively, which are functions of the statistics of the bottom parameters.

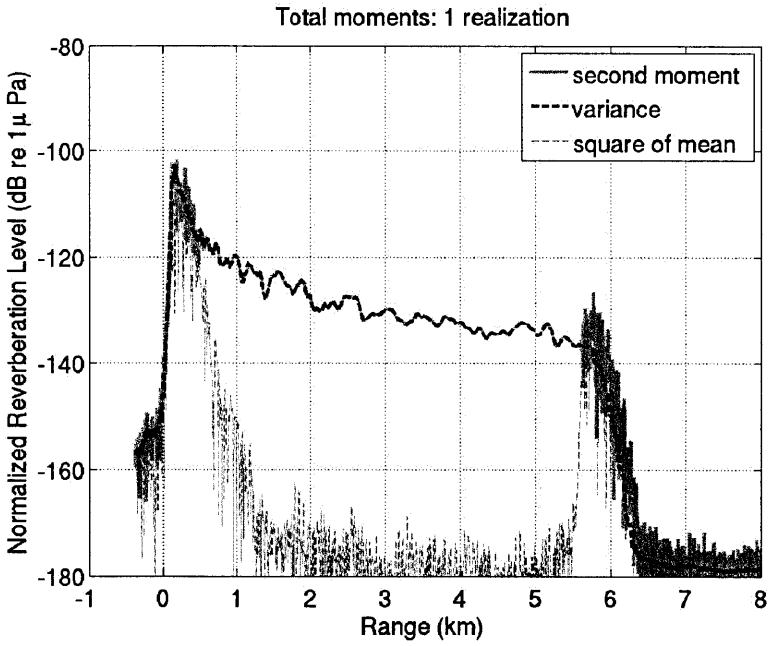

Figure 3-4: Total moments of the full 390-440 Hz matched filtered scattered field in a Pekeris sand waveguide with varying sound speed profiles, for a single realization of the ocean environment. For the case of a single realization, the total moments are equal to the moments conditional on a set of deterministic Green functions.

Next, we verify that the matched filtered variance, as given in Equation A.14, is dominated by the first term. In Figures 3-5 and 3-6 we plot the variance and its three terms, for the cases of 10 and 1 realizations, respectively. For both cases, we note that the first term dominates the total variance, while the last two terms are negligible. For the case of 10 realizations, the third term is the least significant, as it decreases both with an increase in the number of realizations, as well as with a

decrease in dr. The average level of the second term, however, is dependent only on the range increment dr. For the case of a single realization, the second and third terms cancel each other because of the common Green function product. Thus, for one realization, the total variance is equal to the conditional variance.

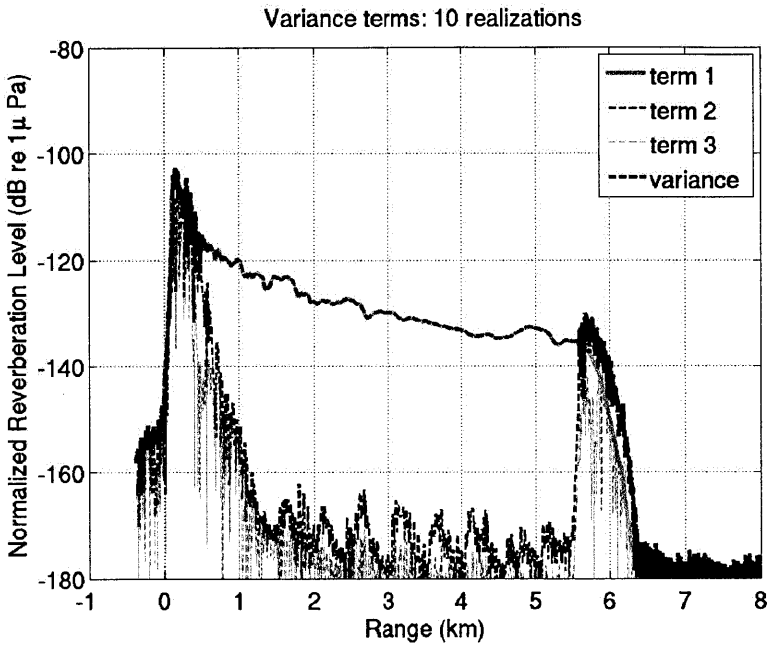

Figure 3-5: Total 390-440 Hz matched filtered variance and its terms in a Pekeris sand waveguide, for 10 realizations of the ocean environment.

Lastly, we demonstrate that we can further approximate the matched filtered scattered intensity by the time harmonic expression in Equation 2.21, where V_S is now the resolution footprint of the sonar. Thus, for the time harmonic expression in Equation 2.21, the integration region V_S corresponds to a seafloor patch that extends over 10m in depth, 3° in azimuth and 15m in range. We have shown that the matched filtered scattered intensity can be approximated by the incoherent term, which, at its turn, can be approximated by the first term of the total matched filtered variance, as expressed in Equation 2.19. By implementing Equations 2.19 and 2.21 to the same Pekeris sand waveguide, we show in Figures 3-7 and 3-8 that the full 390-440 Hz matched filtered expression can be approximated by the time harmonic expression at the 415 Hz center frequency, for both 10 and 1 realizations of the ocean environment, respectively. Figures 3-9 and 3-10, which compare the range-averaged values of the

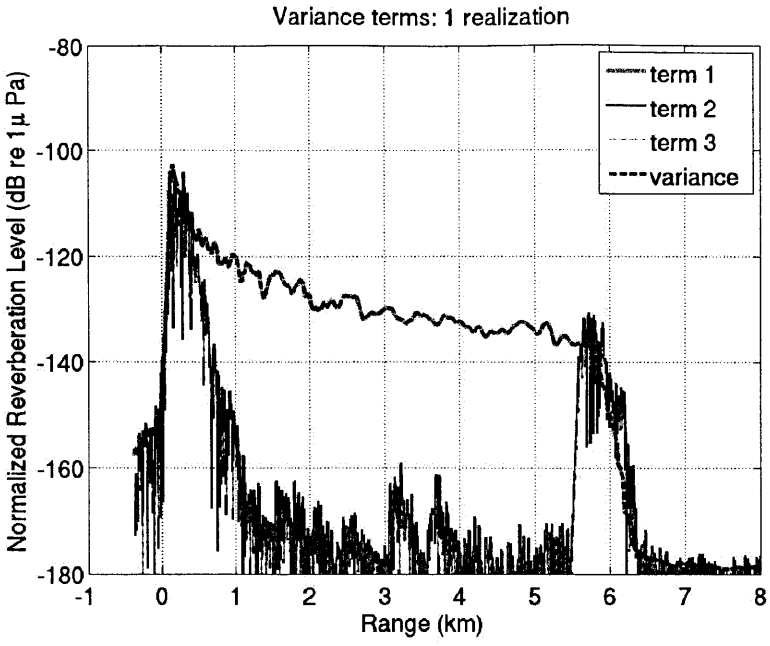

Figure 3-6: Total 390-440 Hz matched filtered variance and its terms in a Pekeris sand waveguide, for a single realization of the ocean environment. For a single realization, the last two terms cancel each other and the total variance is equal to the conditional variance .

two series, show the results are within a few dB. For the last two figures, we have found that if a patch at least 10 km long were considered, averaging over a 2000 m range reduces the difference between the two curves to as low as 1 to 2 dB. We restricted the analysis to a shorter patch in order to reduce computation time.

Equation 2.21 has just been shown to provide a good approximation to Equation 2.19 and to the total scattered intensity, and is the only term assumed in heuristic radiometry approaches. The total time harmonic variance expression of Equation 2.20, however, is not necessarily a good approximation. While the third term of Equation 2.20 is negligible, the second term of Equation 2.20 may not be negligible and is an artifact caused by misapplication of coherent single frequency theory, as shown in Appendix B.

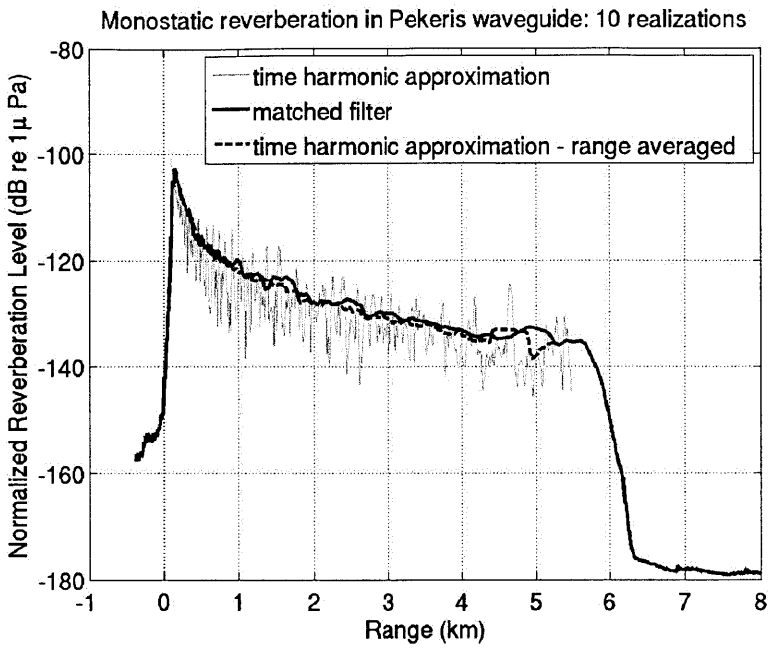

Figure 3-7: Full 390-440 Hz matched filtered depth-integrated monostatic bottom reverberation compared to time harmonic reverberation at center frequency 415 Hz, for 10 realizations of the ocean environment.

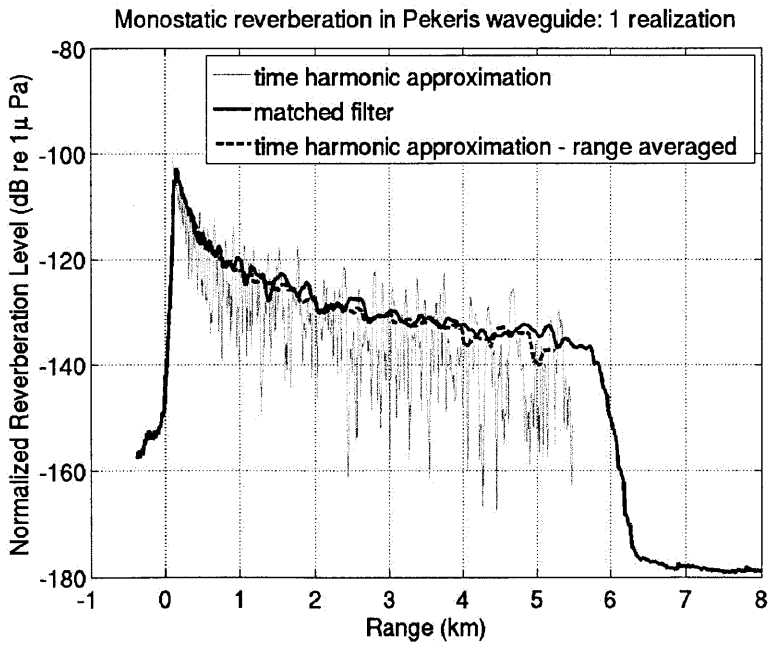

Figure 3-8: Full 390-440 Hz matched filtered depth-integrated monostatic bottom reverberation compared to time harmonic reverberation at center frequency 415 Hz, for a single realization of the ocean environment.

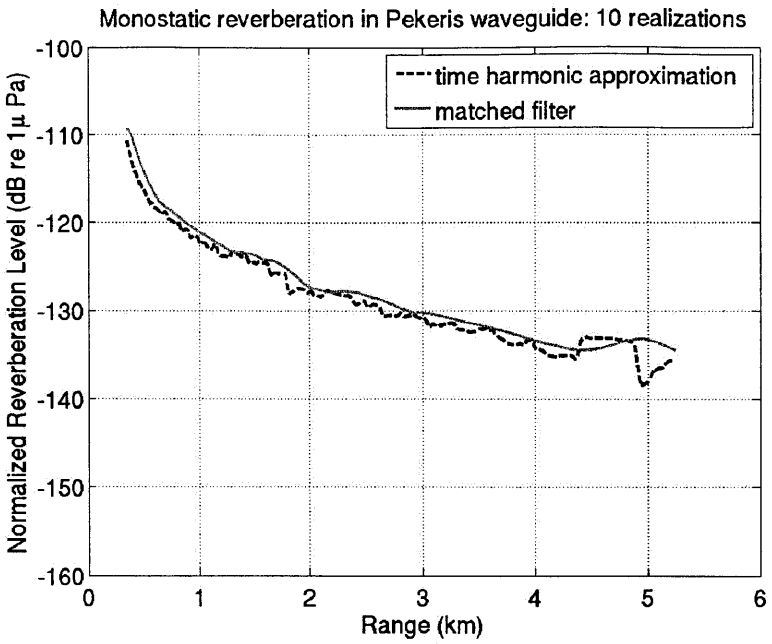

Figure 3-9: Range-averaged full 390-440 Hz matched filter depth-integrated monostatic bottom reverberation compared to range-averaged time harmonic reverberation at center frequency 415 Hz, for 10 realizations of the ocean environment (range averaging over 500 m).

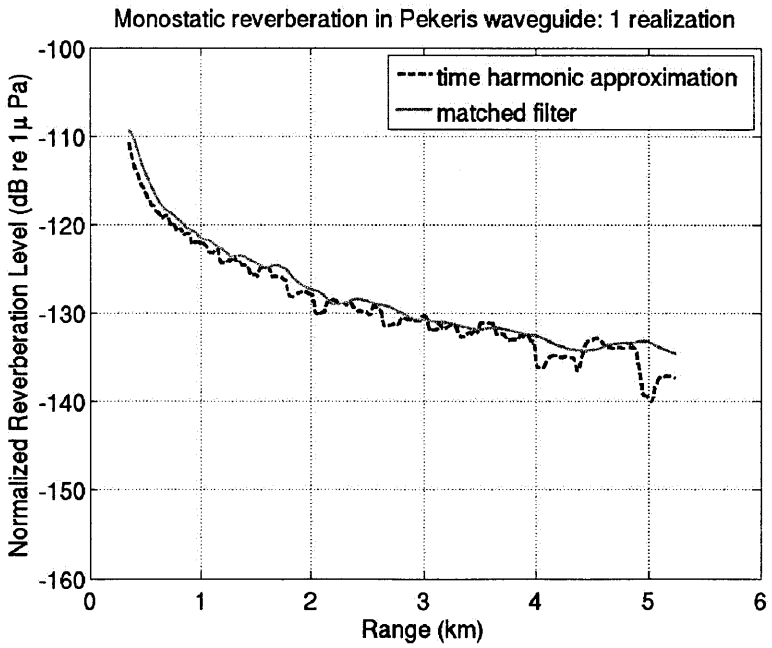

Figure 3-10: Range-averaged full 390-440 Hz matched filter depth-integrated monostatic bottom reverberation compared to range-averaged time harmonic reverberation at center frequency 415 Hz, for a single realization of the ocean environment (range averaging over 500 m).

3.2 Frequency dependence of simulated reverberation

In this subsection, we investigate the frequency dependence of the bottom reverberation using the time harmonic approximation given in Equation 2.21 and keeping the bottom parameters V_c, Var(Γ_κ), Var(Γ_d) and Covar(Γ_κ,Γ_d) constant for all frequencies. The analysis is performed using a Pekeris waveguide similar to the one in the previous subsection, where the actual sound speed profiles have been replaced with an isovelocity profile, with the sound speed constant at 1500 m. The depth and range increments are also modified from the previous section to $dz = 0.1$ m and $dr = 15$ m. Because of the constant sound speed, we only implement the expression in Equation 2.21 for one realization, where the sound speed is constant.

We begin by verifying the result in Galinde et al [6] that the monopole, dipole and cross terms in Equation 2.21 are proportional to the full bottom reverberation. Figures 3-11 and 3-12 show that this holds for both the matched filtered model and the time harmonic approximation, respectively. The results have been computed for an isovelocity Pekeris sand waveguide of Figure 3-1, and the levels have been averaged in range over 500 m.

We further demonstrate that the proportionality holds for all frequencies. We compute the simulated bottom reverberation for all frequencies by applying the time harmonic model to the isovelocity Pekeris waveguide and keeping the bottom parameters constant. After range averaging over 2000 m, we plot, in Figure 3-13, the levels of the full reverberation, monopole, dipole and crossterm at a single point in range. It is clear from the figure that, at 16 km in range from the receiver, the three terms are proportional to the full reverberation for all frequencies. The result was also found to hold for any point in range.

After having shown that the full simulated reverberation level is proportional to

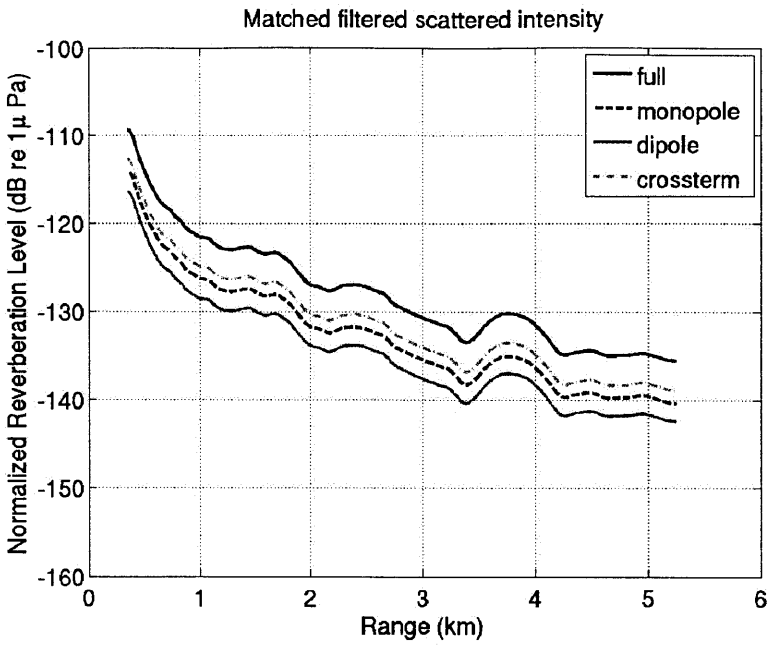

Figure 3-11: Range-averaged full 390-440 Hz matched filter bottom reverberation compared to its three terms: monopole, dipole and crossterm (range averaging over 500 m).

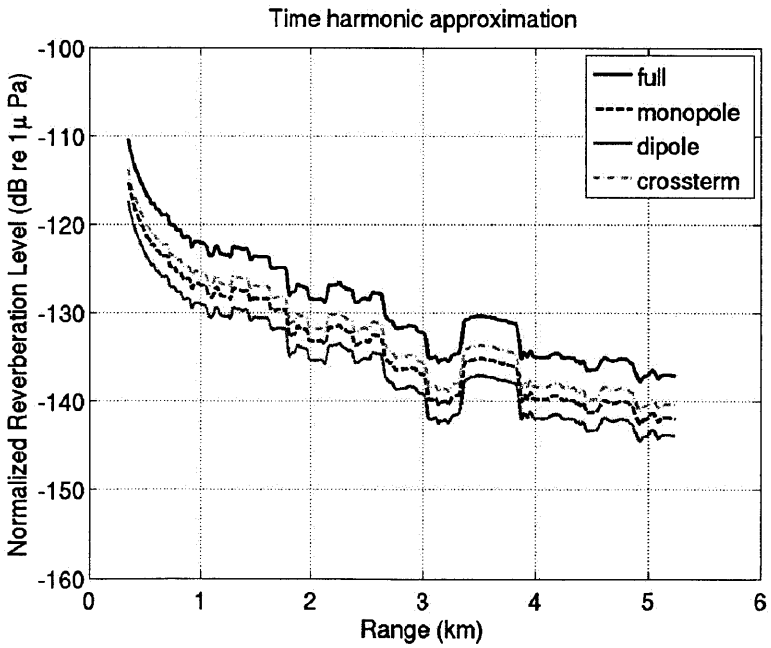

Figure 3-12: Range-averaged time harmonic bottom reverberation at center frequency 415 Hz compared to its three terms: monopole, dipole and crossterm (range averaging over 500 m).

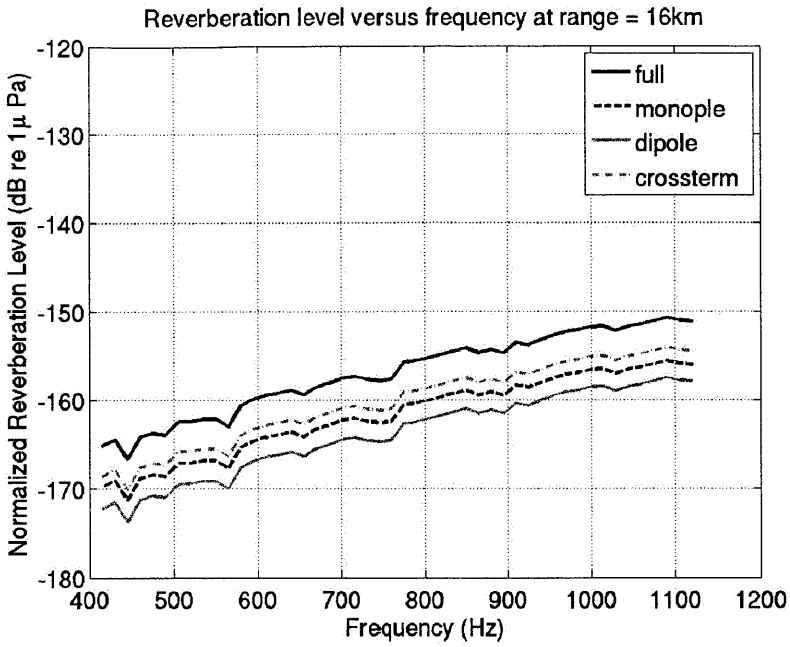

Figure 3-13: Range averaged time-harmonic simulated monostatic reverberation level in a sand Pekeris waveguide with isovelocity sound speed profile, at 16km from source/receiver (range averaging over 2000m).

the monopole term, given below as

$$(4\pi)^2 \iiint_{V_S} V_C(\mathbf{r}_S, z_t) k^4 \mathrm{Var}(\Gamma_k(\mathbf{r}_t)) \langle |G(\mathbf{r}_t|\mathbf{r}_0, f)|^2 |G(\mathbf{r}|\mathbf{r}_t, f)|^2 \rangle dV_t, \tag{3.1}$$

we can use this term to investigate the frequency dependence of the model. Since we keep the bottom parameters V_C and $\mathrm{Var}(\Gamma_k)$ constant for all frequencies, we can further restrict our analysis to the frequency dependence of the following term:

$$k^4 \iiint_{V_S} \langle |G(\mathbf{r}_t|\mathbf{r}_0, f)|^2 |G(\mathbf{r}|\mathbf{r}_t, f)|^2 \rangle dV_t. \tag{3.2}$$

For a monostatic scenario with the source and receiver collocated, this is equal to

$$k^4 \iiint_{V_S} \langle |G(\mathbf{r}_t|\mathbf{r}_0, f)|^4 \rangle dV_t. \tag{3.3}$$

Based on the equation above, for constant bottom parameters, we expect the reverberation level to have a f^4 frequency dependence due to the k^4 factor, and

a yet unknown frequency dependence due to the integral over the fourth power of the Green function. Since penetration depth is known to decrease with increasing frequency, however, we expect the volume integral in Equation 3.3 to be inversely proportional to frequency.

To determine the actual frequency dependence of the simulated reverberation numerically, we compute the time-harmonic simulated reverberation levels for a range of frequencies using the standard Pekeris sand waveguide with isovelocity sound speed profile. The bottom parameters are kept constant for all frequencies, and equal to those previously summarized in Table 3.1. In Figure 3-14 we plot the simulated reverberation levels versus range, for four different frequencies. The figure clearly shows an increase in reverberation level for higher frequencies.

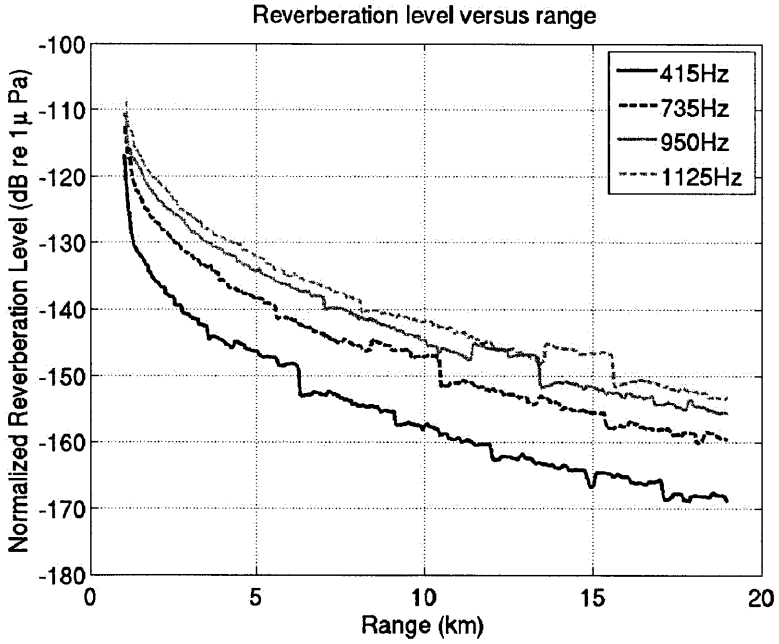

Figure 3-14: Range-averaged time-harmonic simulated monostatic reverberation level in a sand Pekeris waveguide with isovelocity sound speed profile, at 415, 735, 950 and 1125 Hz, respectively (range averaging over 2000 m).

To test whether the increase in reverberation level is consistent across all frequencies, we plot the simulated reverberation level versus frequency for several points in range, in Figure 3-15. We also plot the log-log of the simulated reverberation level versus frequency for only the first range (4000 m) in Figure 3-16, and note that the

frequency dependence is approximately f^4.

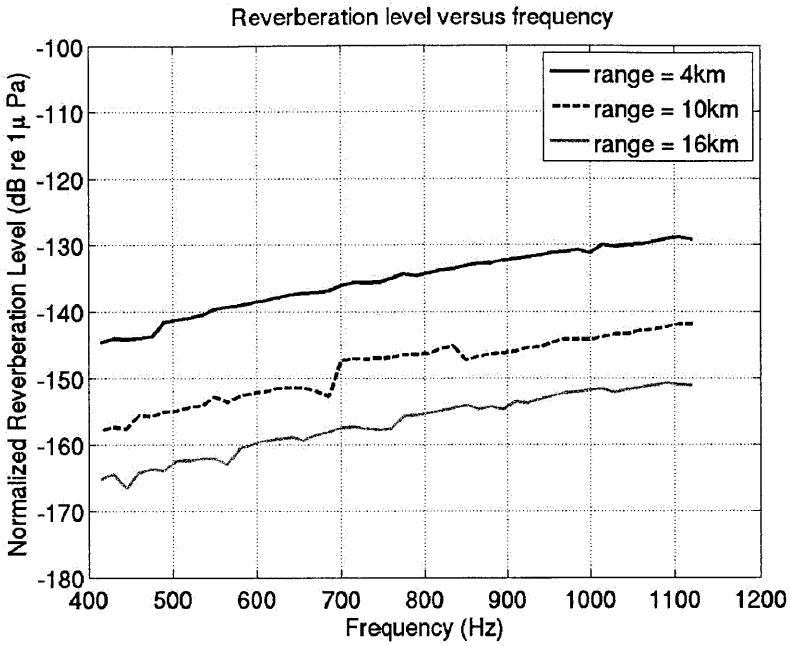

Figure 3-15: Range-averaged time-harmonic simulated monostatic reverberation level in a sand Pekeris waveguide with isovelocity sound speed profile, for all frequencies, at 4, 10 and 16 km in range, respectively (range averaging over 2000 m).

The fact that the reverberation level varies with approximately the fourth power of frequency, and the presence of the k^4 term in Equation 3.3 lead us to believe that the volume integral in Equation 3.3 is nearly frequency independent. To verify this, we plot the volume integral versus frequency in Figure 3-17 and versus the log of frequency in Figure 3-18. The two figures confirm that the integral is indeed nearly independent of frequency, as it varies approximately with $f^{-0.25}$.

As penetration depth is known to decrease with an increase in frequency, which makes the statement that the volume integral is nearly frequency independent counterintuitive, we provide further analysis to support this result. We plot the value of the integral in Equation 3.3 at several depths, as indicated in Figure 3-19. As the depth increment for this case is $dz = 0.1$ m, this represents an integral over a bottom layer that is 0.1 m thick. Next, we plot the value of the integral from the 100 m interface, down to several depths, as mentioned in Figure 3-20. Here, the integration is performed over all 0.1 m thick bottom layers located above the depths indicated in

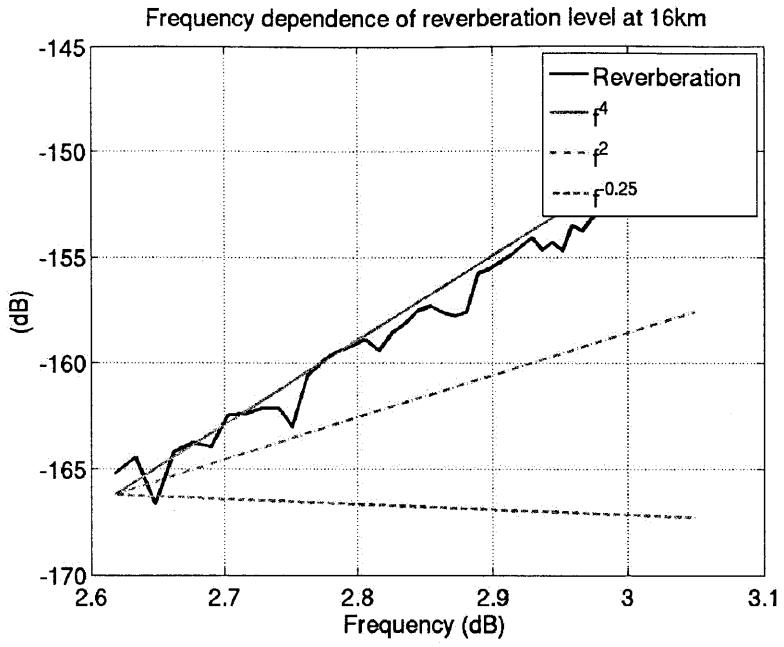

Figure 3-16: Frequency dependence of time-harmonic simulated monostatic reverberation level at 16 km in range for a sand Pekeris waveguide with isovelocity sound speed profile (range averaging over 2000 m), for bottom parameters V_c, $\mathrm{Var}(\Gamma_\kappa(\mathbf{r}_t))$, $\mathrm{Var}(\Gamma_d(\mathbf{r}_t))$ and $\mathrm{Covar}(\Gamma_\kappa(\mathbf{r}_t))$ constant for all frequencies.

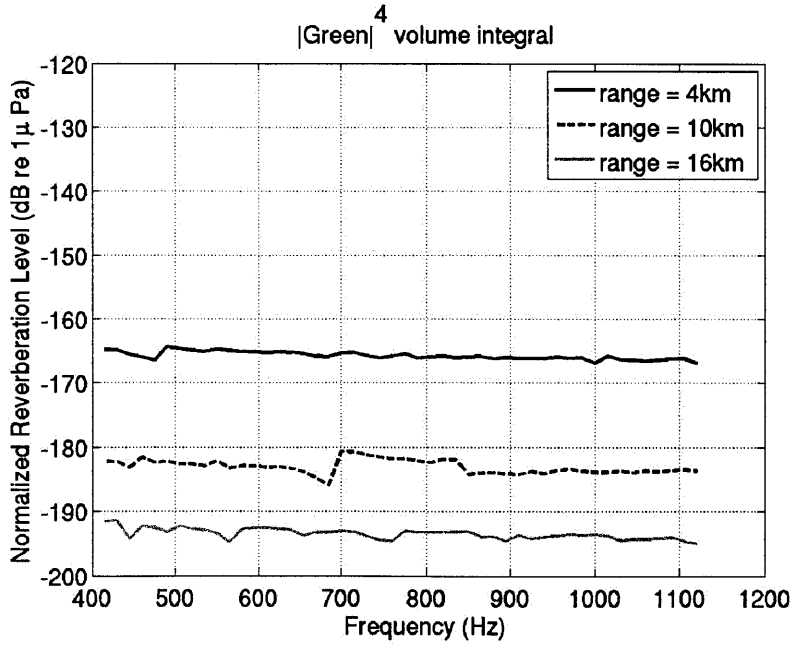

Figure 3-17: Volume integral from Equation 3.3 plotted versus frequency for several locations in range

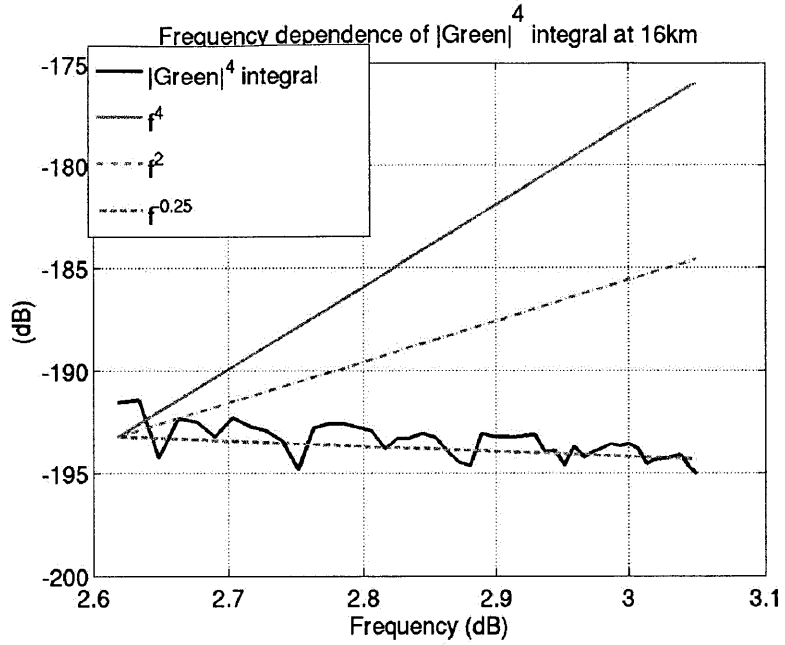

Figure 3-18: Frequency dependence of volume integral from Equation 3.3.

the legend. The figures show that, although the intensity within the layers changes for different frequencies and depths, causing the volume integral at low frequencies to converge in depth slower than at high frequencies, the total volume integral remains relatively constant across frequencies. The most plausible explanation for this phenomenon is that the top layers, with weak frequency dependence, are dominant.

The analysis presented in this section shows that the frequency dependence of the simulated reverberation, with constant bottom parameters V_c, $\mathrm{Var}(\Gamma_\kappa)$, $\mathrm{Var}(\Gamma_d)$ and $\mathrm{Covar}(\Gamma_\kappa,\Gamma_d)$, is approximately f^4. Literature detailing experimental results [8] reveals, however, that measured ocean bottom reverberation has a low frequency dependence. This is consistent with our model if we let the coherence volume V_C vary with frequency, as also suggested by Galinde et al [6], who state that the acoustically determined V_c may not equal the geological coherence volume for the bottom inhomogeneities, and it may vary with frequency. In the next section, we use the time-harmonic model for ocean bottom reverberation to invert for the bottom parameters for several frequencies at two distinct geographical locations.

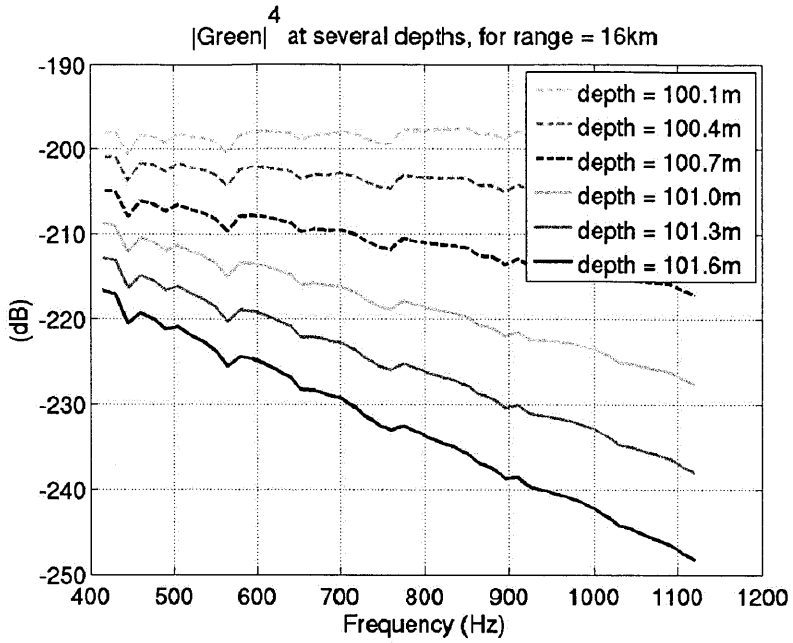

Figure 3-19: Value of the integral in Equation 3.3 evaluated at several depths: the integration is performed over a bottom layer that is 0.1 m thick, as $dz = 0.1$ m.

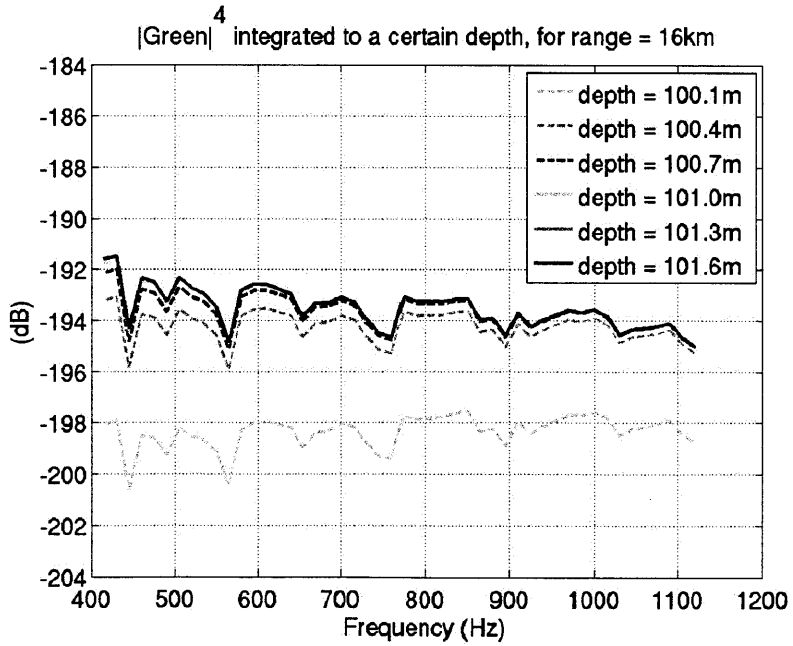

Figure 3-20: Value of the integral in Equation 3.3 evaluated from the 100 m water/air interface down to several depths: the integration is performed over all 0.1 m thick bottom layers located between 100 m and the depths indicated in the legend.

Chapter 4

Model calibration to bottom reverberation data

In this section we compare simulated bistatic, range-dependent reverberation to reverberation measured during the course of two experiments at sea. We use the efficient time harmonic approximation of Equation 2.21 to the matched filtered model and invert for the one parameter needed to scale the bottom parameters $V_c(\mathbf{r}_S, z_t)$, $\mathrm{Var}(\Gamma_\kappa(\mathbf{r}_t))$, $\mathrm{Var}(\Gamma_d(\mathbf{r}_t))$ and $\mathrm{Covar}(\Gamma_\kappa(\mathbf{r}_t))$ given known ratios for the monopole, dipole and cross terms. We use the least squares method to find the best fit parameter and provide statistics of the inverted parameter for each experiment, at three different frequencies.

4.1 OAWRS bottom reverberation data

For model calibration, we use data acquired by the ocean acoustic waveguide remote sensing (OAWRS) system during experiments conducted in 2003 on the New Jersey continental shelf and 2006 on the northern flank of Georges Bank in the Gulf of Maine.

The 2003 experiment was conducted from April 27 to May 15, 2003 on the New Jersey Strataform [2], [16], [13]. The bathymetry of the region is relatively flat, with depths ranging from 65 to 80 m. The bottom sediment in the region consists mostly of sand with a mean density, sound speed, and attenuation of approximately 1.9

g/cm^3, 1700 m/s, and 0.8 dB/λ, respectively [7], [6]. Over 100 sound speed profiles have been measured during the experiment to allow accurate characterization of the randomly fluctuating continental shelf waveguide. The bistatic OAWRS system consisted of a moored vertical array source centered at a depth of 47 m, and a horizontal receiving array towed at depths between 30 and 50 m. The source transmitted Tukey-shaded linear frequency modulated (LFM) broadband pulses in three distinct frequency ranges, 390 to 440 Hz, 875 to 975 Hz, and 1250 to 1400 Hz, each 1 second in duration at every 50 second interval.

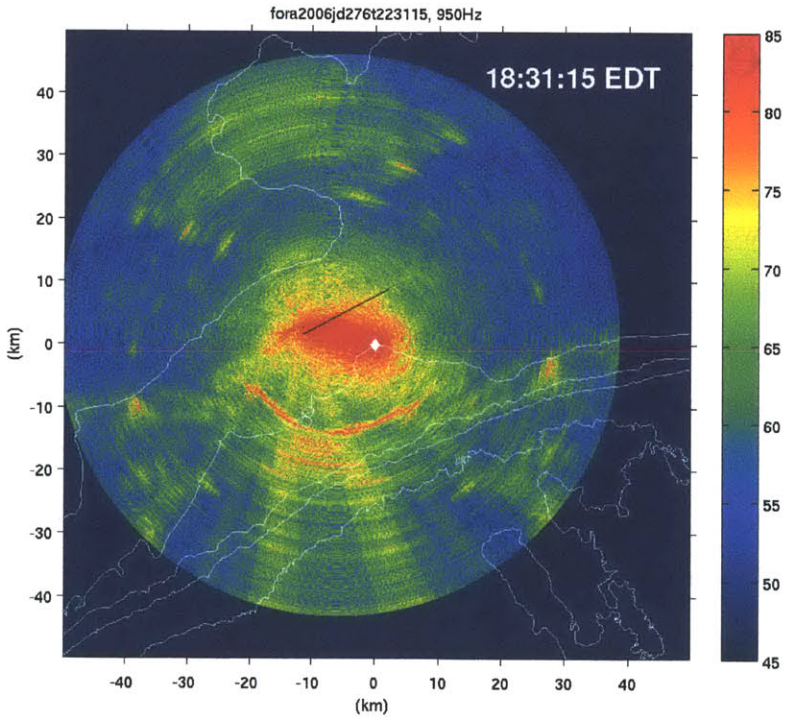

Figure 4-1: OAWRS image charting returns (dB re 1 μPa) received on the Northern Flank of Georges Bank at 18:31 EDT, on 3 October 2006. The white diamond indicates the source and the black line is the receiver track. The white curves are bathymetric contours for the region. Clutter is distinguished from seafloor returns by inspecting both the bathymetry of the region and the stationarity of the returns over multiple pings. Ship beams are also identified as radiating outward from the receiver, symmetrically about the endfire of the receiver array.

For the 2006 experiment, conducted from September 19 to October 6 [13], [8], [15] on the Northern Flank of Georges Bank in the Gulf of Maine, the water depth ranged from as shallow as 20 m to as deep as 400 m. The sediment at the experimental

site was found to consist of sand with sound speed of 1700 m/s, density of 1.9 g/cm^3 and attenuation of 0.8 dB/λ [8]. Roughly 200 sample sound speed profiles of the water column have been taken during the experiment. The OAWRS imaging system consisted of a moored vertical source array and a towed horizontal receiver array, centered at 65 and 105 m depth, respectively. One second Tukey-windowed LFM pulses were transmitted by the source in a 50 Hz frequency band around the center frequencies of 415, 735, 950 and 1125 Hz, 75 seconds apart.

The pressure data collected from both experiments was beamformed and matched filtered to determine the azimuth and range of arrivals and instantaneous OAWRS images such as the one shown in Figure 4-1 have been created for every broadband transmission [6], [8], [16], [15].

4.2 Parameter inversion methodology

We invert for only one parameter, as we have shown that the monopole, dipole and cross terms are proportional to the total intensity for the 415 Hz center frequency (Figure 3-12), as well as for all frequencies in the 415-1125 Hz frequency range considered (Figure 3-13). This proportionality allows us to express the total scattered intensity, or reverberation, as the product of one parameter and the monopole term. For this, we assume that $V_c(\mathbf{r}_S, z_t)$ and the moments of the fractional changes in bottom density and compressibility $\mathrm{Var}(\Gamma_\kappa(\mathbf{r}_t))$, $\mathrm{Var}(\Gamma_d(\mathbf{r}_t))$ and $\mathrm{Covar}(\Gamma_\kappa(\mathbf{r}_t))$ are constant across the seafloor as well as depth. Then, they can be taken outside the volume integral in Equation 2.21 and the time harmonic reverberation can be expressed as:

$$
\begin{aligned}
&\mathrm{Var}(\Phi_S(\mathbf{r}_S|\mathbf{r},\mathbf{r}_0,f)) \qquad (4.1)\\
&= (4\pi)^2 V_C \mathrm{Var}(\Gamma_k) \iiint_{V_S} k^4[\langle|G(\mathbf{r}_t|\mathbf{r}_0,f)|^2|G(\mathbf{r}|\mathbf{r}_t,f)|^2\rangle]dV_t\\
&+ (4\pi)^2 V_C \mathrm{Var}(\Gamma_d) \iiint_{V_S} [\langle|\nabla G(\mathbf{r}_t|\mathbf{r}_0)\cdot\nabla G(\mathbf{r}|\mathbf{r}_t)|^2\rangle]dV_t\\
&+ (4\pi)^2 V_C \mathrm{Cov}(\Gamma_k,\Gamma_d) \iiint_{V_S} k^2[2\Re\{G(\mathbf{r}_t|\mathbf{r}_0,f)G(\mathbf{r}|\mathbf{r}_t,f)\times\nabla G^*(\mathbf{r}_t|\mathbf{r}_0,f)\cdot\nabla G^*(\mathbf{r}|\mathbf{r}_t,f)\}\rangle]dV_t,
\end{aligned}
$$

where the first integral is a monopole term, the second integral is a dipole term, and the last integral is a crossterm. Using the fact that the three terms are proportional, we can define F_d and F_c so that F_d represents the ratio between the dipole integral and monopole integral, and F_c represents the ratio between the crossterm integral and monopole integral. Then, we can further simplify Equation 4.1 as:

$$\begin{aligned} &\mathrm{Var}(\Phi_S(\mathbf{r}_S|\mathbf{r},\mathbf{r}_0,f)) \\ &\quad = (4\pi)^2 V_C[\mathrm{Var}(\Gamma_k) + F_d\mathrm{Var}(\Gamma_d) + F_c\mathrm{Cov}(\Gamma_k,\Gamma_d)] \\ &\quad \times \iiint_{V_S} k^4[\langle|G(\mathbf{r}_t|\mathbf{r}_0,f)|^2|G(\mathbf{r}|\mathbf{r}_t,f)|^2\rangle]dV_t. \end{aligned} \tag{4.2}$$

Finally, the simplified one-parameter model we use for calibration is:

$$\mathrm{Var}(\Phi_S(\mathbf{r}_S|\mathbf{r},\mathbf{r}_0,f)) = \theta \times \iiint_{V_S} k^4[\langle|G(\mathbf{r}_t|\mathbf{r}_0,f)|^2|G(\mathbf{r}|\mathbf{r}_t,f)|^2\rangle]dV_t, \tag{4.3}$$

where the parameter we need to estimate is

$$\theta = (4\pi)^2 V_C[\mathrm{Var}(\Gamma_k) + F_d\mathrm{Var}(\Gamma_d) + F_c\mathrm{Cov}(\Gamma_k,\Gamma_d)]. \tag{4.4}$$

To find an estimate $\hat{\theta}$ for the parameter θ from the data, we use the method of least squares. The equation used to find the estimate $\hat{\theta}$ from the data using the model of Equation 4.3 is

$$\min_{\theta} \sum_{i=1}^{n} |10\log(\frac{|\Phi_{S_i Data}(\mathbf{r}_{S_i}|\mathbf{r},\mathbf{r}_0,f)|^2}{P_{ref}^2}) - 10\log(\frac{\mathrm{Var}(\Phi_{S_i}(\mathbf{r}_{S_i}|\mathbf{r},\mathbf{r}_0,f))}{P_{ref}^2})|^2, \tag{4.5}$$

where $|\Phi_{S_i Data}(\mathbf{r}_{S_i}|\mathbf{r},\mathbf{r}_0,f)|^2$ represents the measured reverberation level at $\mathbf{r}_{S_i}$. The summation is over all n resolution footprints V_{S_i} centered at $\mathbf{r}_{S_i}$ included in the seafloor region we use for calibration. Using Equation 4.3, we find that the parameter estimate $\hat{\theta}$ is given by

$$10\log(\hat{\theta}) = \frac{\sum_{i=1}^{n} 10\log|\Phi_{S_i Data}(\mathbf{r}_{S_i}|\mathbf{r},\mathbf{r}_0,f)|^2}{\sum_{i=1}^{n} 10\log(\iiint_{V_{S_i}} k^4[\langle|G(\mathbf{r}_t|\mathbf{r}_0,f)|^2|G(\mathbf{r}|\mathbf{r}_t,f)|^2\rangle]dV_t)}. \tag{4.6}$$

We note that using least squares for logarithmic variables may lead to biases in $\hat{\theta}$ [14].

Using beam time received pressure intensity data for one ping at a time, we find the best fit parameter for each beam in the respective ping. We do this by applying Equation 4.6 and estimating one value of θ for each beam within the particular ping. To obtain a statistically significant set of inverted parameters, we analyze multiple pings. We restrict our analysis to pings and beams that are not contaminated by clutter or ship noise, and to regions of relatively flat or downward sloping bathymetry. In the next section, we describe the beam time data used in the calibration and the methodology for implementing the model along a beam. We then compare the model simulation results with experimental data along beams. In the following section we compare the model simulation results with data for wide area polar plots.

4.3 Model/data comparison using beam time data

In this subsection, we begin our model/data comparison by considering the receiver reverberation intensity versus beam time and range. In the next subsection, we compare the model and data using wide area polar plots. All the analysis in the two sections is performed for pings received at the center frequency 415 Hz.

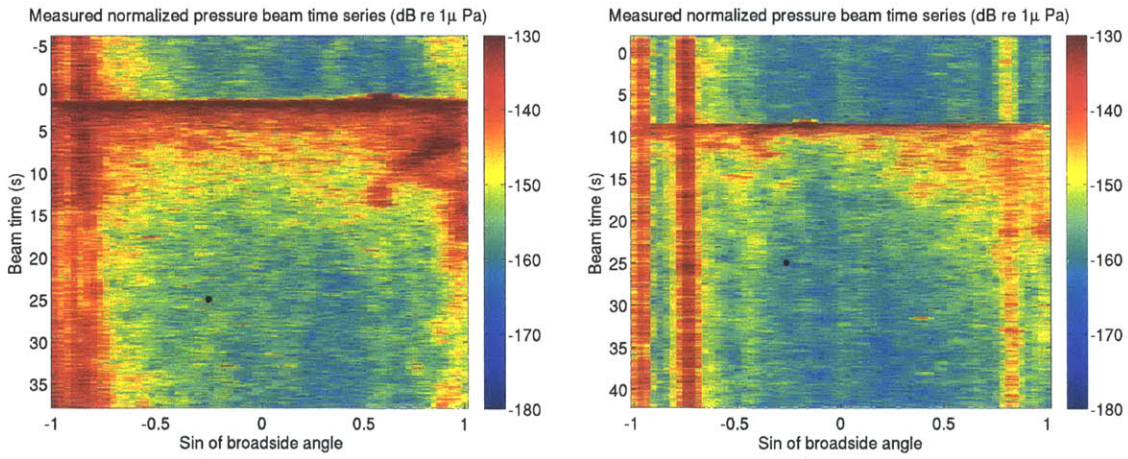

Figure 4-2: Measured normalized pressure level as beam time series for the New Jersey continental shelf (left) and Georges Bank in the Gulf of Maine (right). The black stars indicate the beams chosen for analysis. The source is broadband for 415 Hz center frequency and 50 Hz bandwidth and the source level is normalized to 0 dB re 1 μPa at 1m.

Each ping, for both the 2003 and 2006 ONR Geoclutter Experiments, consists of 65 or 66 beams of data covering an azimuthal sector of 180°, received continuously over a 50 or 75 second interval, depending on the experiment. The directions of the beams are uniformly spaced in $\sin(\phi)$, where ϕ is the angle of the beam relative to the broadside of the receiver. Figure 4-2 shows two examples of pings recorded during the New Jersey and Georges Bank experiments, respectively. The pings shown are partially contaminated by ship beams and clutter, which is often the case for the data collected, raising a need to restrict our analysis to clean beams that are stationary over multiple pings. Because of left-right ambiguity about the receiver heading, the reverberation data for each beam corresponds to the sum of the returns from a pair of two separate azimuthal directions, received along what we define as *original* and *mirror* beams. The beam time reverberation data is thus a function of

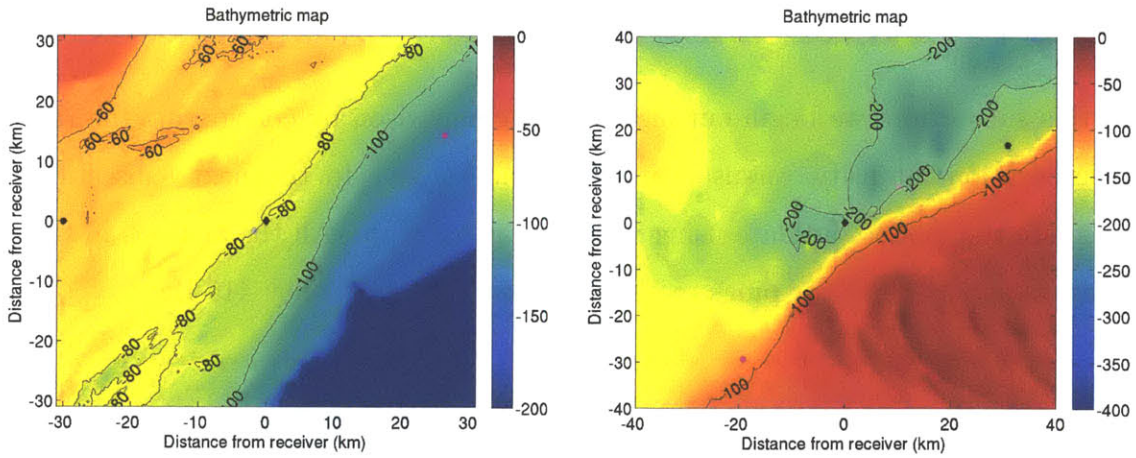

Figure 4-3: (Left) Bathymetric map of the New Jersey continental shelf indicating the source and receiver positions at 10:31 EDT, on 13 May 2003. The grey diamond indicates the source, located at 39.2312N, 72.8818W and operating at 390-440 Hz. The black diamond indicates the receiver, located at 39.2465N, 72.8626W, with heading 346°E. The black and magenta stars indicate the beams chosen for analysis, corresponding to the original and mirror beams, respectively. (Right) Bathymetric map of the northern flank of Georges Bank in the Gulf of Maine indicating source and receiver positions at 11:58 EDT, on 26 September 2006. The grey diamond indicates the source, located at 41.8901N, 68.2134W and operating at 390-440 Hz. The black diamond indicates the receiver, located at 41.8212N, 68.3368W, with heading 137°E. The black and magenta stars indicate the beams chosen for analysis, corresponding to the original and mirror beams, respectively.

$\sin(\phi)$ and beam time. This data can be charted to range and converted into polar

plots by multiplying the beam time with the sound propagation speed in the ocean and accounting for the bistatic geometry i.e. the distance traveled from source to each scatterer location in range along the beam and from the scatterer to the receiver.

To accurately model the reverberation received along each beam for a certain ping, we first account for all the variables of the problem, such as the actual bistatic geometry of the respective ping, bathymetry, sound speed profiles, seafloor and ocean properties and source and receiver array types. Each beam data time series corresponds to two patches in the seafloor, placed symmetrically about the receiver heading, along the *original* and *mirror* directions. The two patches extend over an azimuthal angle equal to the sonar angular resolution, over the top 10 m deep bottom layer and over 25 to 35 km in range from the receiver location, depending on the length of the data time series we use for comparison or the extent of the region for which we have bathymetric data. Since we use the time harmonic model for computational efficiency, we only integrate over volumes V_S that are 15 m long in range, corresponding to the sonar range resolution, at each point in range along the two patches. Examples of bistatic geometries from the New Jersey continental shelf and the northern flank of Georges Bank in the Gulf of Maine are depicted in Figure 4-3, showing the source and receiver (as the grey and black diamonds, respectively), along with black and magenta stars, corresponding to the *original* and *mirror* patches selected for analysis in this subsection. The background of the maps represents the relatively flat bathymetry in the region chosen for analysis, respectively.

Next, we compute the Green functions using the parabolic equation model RAM. For both experiments, we use sand as the bottom sediment type, with sound speed of 1700 m/s, density of 1.9 g/cm^3 and attenuation of 0.8 dB/λ, as mentioned in Section 4.1. We use a range increment $dr = 15$ m, a depth increment $dz = 0.4$ m, and we assume the Green function is uniform in azimuth over the angular resolution. Since both the *original* and *mirror* patches radiate outward from the receiver location, computing the Green function from the receiver to each range increment along the patch requires running RAM only once. However, for the bistatic case, computing the Green function from the source to each range increment along the patch requires

running RAM a great number of times. For computational efficiency, we run RAM from the source to only several points in range along each patch (sufficient for convergence) and interpolate the points to find the source Green function along the entire patch. The interpolation is performed in order to obtain a value for both the source and receiver Green functions at each range increment along the patch and thus increase the accuracy in fitting the model to the data. The Green functions are then used to compute the volume integral for the monopole term in Equation 4.3 over all resolution cells V_S along both the *original* and *mirror* patches. Since the time harmonic result is a function of range, due to the implementation at each resolution cell V_S, we convert range to time before adding the contributions from the *original* and *mirror* patches. Lastly, we use the least squares method to find the parameter that provides the best fit of the simulated reverberation to the beam time data along each beam considered.

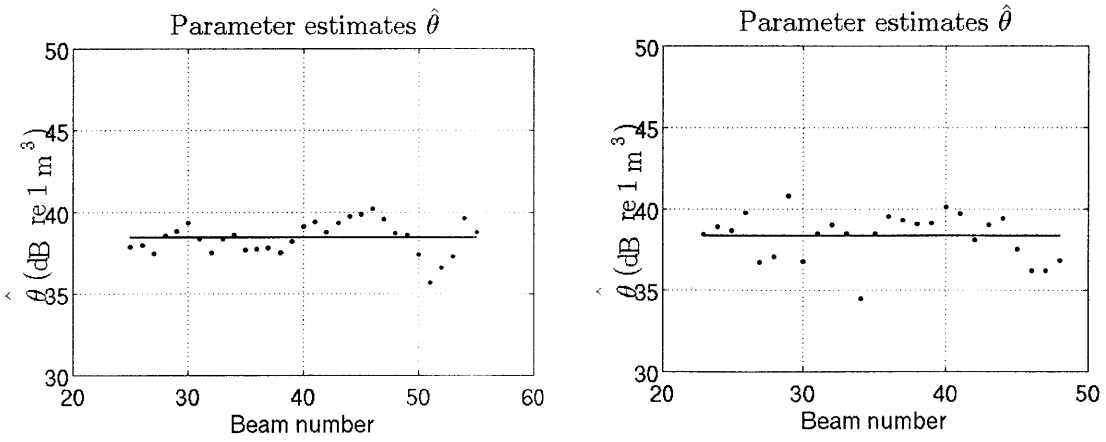

Figure 4-4: Parameter estimates $\hat{\theta}$ (log scale) estimated from the data pings shown in Figure 4-2 for the New Jersey (left) and Georges Bank (right) experiments, at 415 Hz. Each $\hat{\theta}$ corresponds to one beam and was estimated using Equation 4.6, where the summation is performed over all n resolution cells V_{S_i} along the beam. Typically, each beam extends for 25 to 35 km in range, which leads to values of n from 1667 to 2333, respectively, given the sonar range resolution of 15 m. The mean of the parameter estimates $\langle\hat{\theta}\rangle$ is indicated by the horizontal line and is obtained using Equation 4.7, with $p = 1$ and m representing the number of beams in each ping. For this figure, m equals 31 and 36 for the New Jersey and Georges Bank experiments, respectively.

The procedure described above can be repeated for all clutter-free beams within a certain ping, as well as for multiple pings. Typically, we average $\hat{\theta}$ over all calibrated

certain ping, as well as for multiple pings. Typically, we average $\hat{\theta}$ over all calibrated beams within a ping and over multiple pings, and then verify the fit of the model using the mean parameter estimate $\langle\hat{\theta}\rangle$. For the case of p pings each with m beams, $\langle\hat{\theta}\rangle$ is obtained by averaging over a total of mp ping-beam samples, and is given by

$$\langle\hat{\theta}\rangle = \frac{1}{m}\frac{1}{p}\sum_{j=1}^{m}\sum_{h=1}^{p}\hat{\theta}_{jh}. \tag{4.7}$$

In this subsection, however, we restrict our analysis to only one ping for each of the two experiments, corresponding to the beam time series data shown in Figure 4-2. Thus, for this special case, $p = 1$. The parameters $\hat{\theta}$ (in log) estimated for each of the m beams of the two pings are shown in Figure 4-4. A particular trend in $\hat{\theta}$ for consecutive beams within a ping could be an indication of a geographical feature or of gradual ship beam contamination. The red line indicates the mean parameter estimate $\langle\hat{\theta}\rangle$ as given by Equation 4.7 with $p = 1$ and m representing the number of beams in each ping. In Figure 4-5, we compare the measured reverberation level to the reverberation level simulated using Equation 4.3 and $\langle\hat{\theta}\rangle$ of Figure 4-4, along one of the beams for each experiment. For the range averaged levels presented in Figure 4-6 for the same beams, the errors are within 5 to 6 dB.

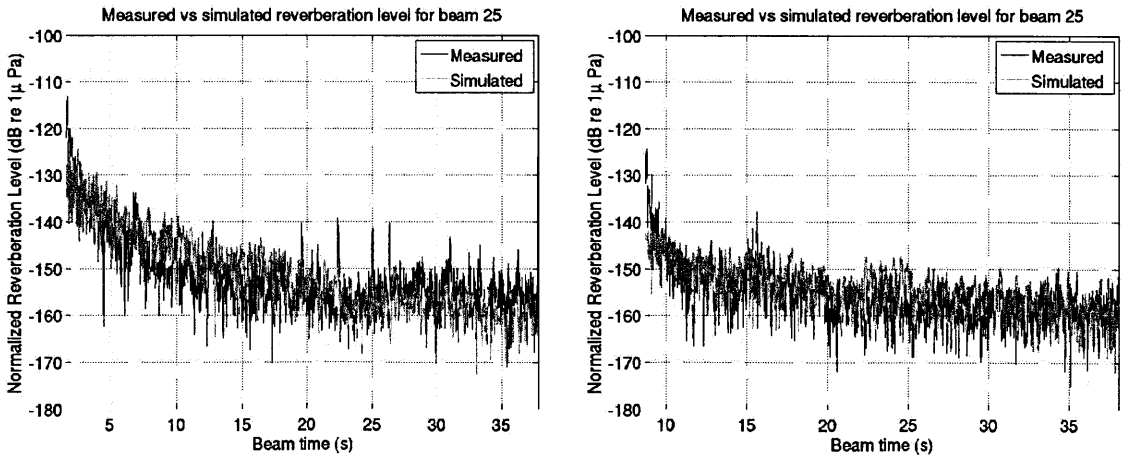

Figure 4-5: Model/data comparison along one beam for pings received at center frequency 415 Hz during the New Jersey (left) and Georges Bank (right) experiments, respectively. The source level is normalized to 0 dB re 1 μPa at 1 m .

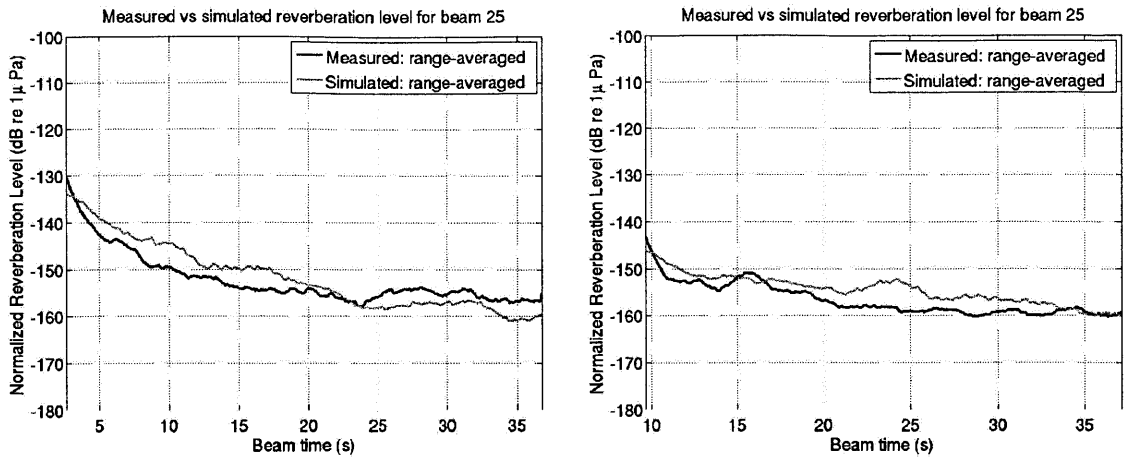

Figure 4-6: Model/data comparison along one beam for pings received at center frequency 415 Hz during the New Jersey (left) and Georges Bank (right) experiments, respectively (range averaging over 2000 m). The source level is normalized to 0 dB re 1 μPa at 1 m .

4.4 Model/data comparison using polar plots

Implementing the methodology described in the previous subsection and calibrating the model to data for consecutive beams within a ping enables us to create wide area polar plots of the simulated reverberation, and to compare them with polar plots of the data. Figure 4-7 shows the polar plots for the data (top), model (middle) and data-model differences (bottom) for the New Jersey (left) and Georges Bank (right) experiments. We can note from the figure that for the New Jersey ping, the beam time series was converted to an approximately symmetric range on both sides about the receiver heading, while for the Georges bank ping, a shorter range resulted on one side than on the other. This is because the separation between the source and receiver is larger for the Georges Bank ping, as we have seen in Figure 4-3. The patches of uniform intensity located at the sharp angle of the polar plots for Georges Bank are also due to the range stretching. Overall, the results are satisfactory, as the data-model differences plots show most of the errors fall within 5 dB. The data-model error at the i^{th} resolution footprint $V_{S_{ij}}$ along beam j is given by

$$10\log\left(\frac{|\Phi_{S_{ij}{}^{Data}}(\mathbf{r}_{S_{ij}}|\mathbf{r},\mathbf{r}_0,f)|^2}{P_{ref}^2} - \langle\hat{\theta}\rangle \frac{\iiint_{V_{S_{ij}}} k^4[\langle|G(\mathbf{r}_t|\mathbf{r}_0,f)|^2|G(\mathbf{r}|\mathbf{r}_t,f)|^2\rangle]dV_t}{P_{ref}^2}\right), \quad (4.8)$$

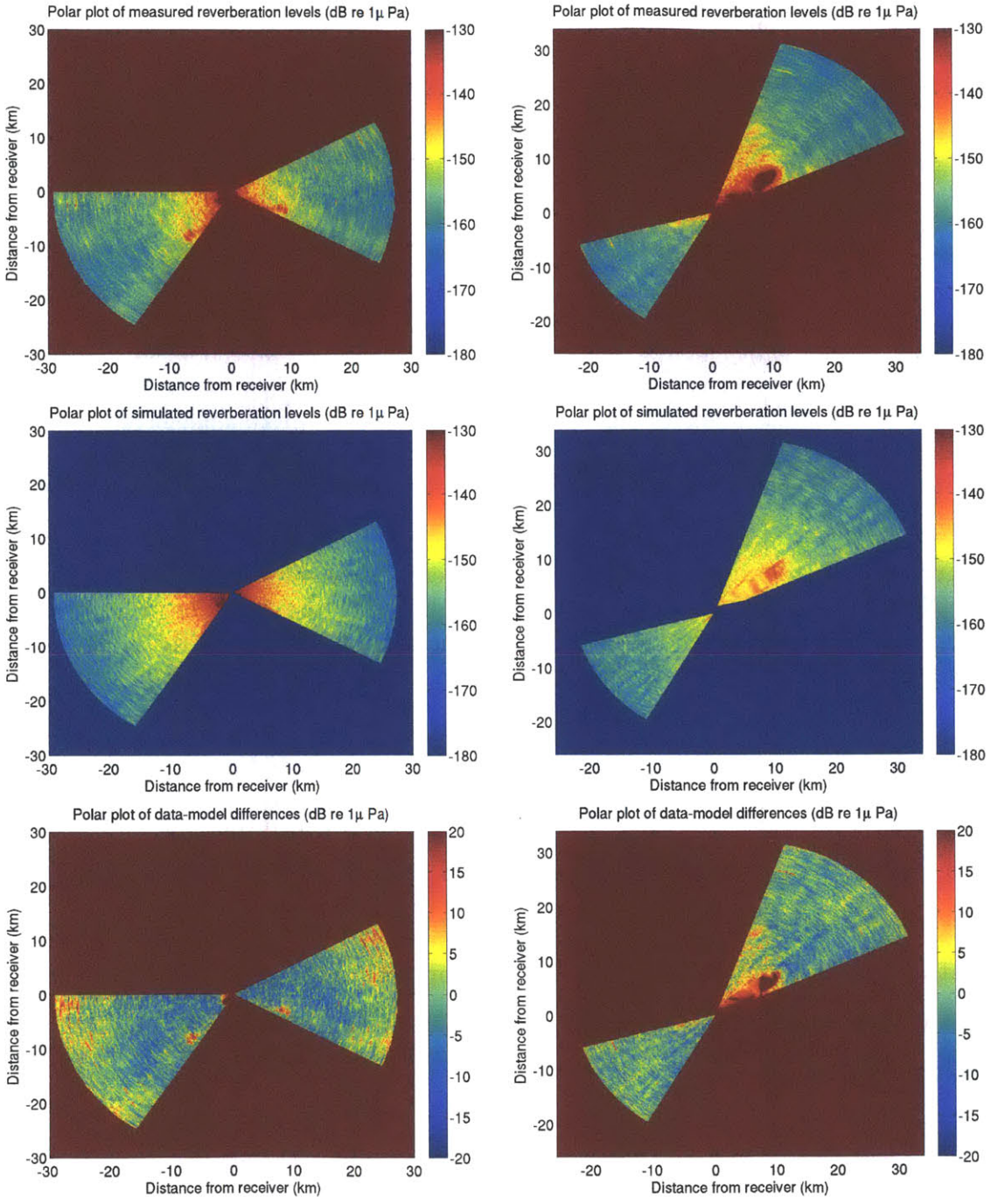

Figure 4-7: Polar plots of measured reverberation level (top), simulated reverberation level (middle) and their difference (bottom) for New Jersey (left) and Georges Bank (right). The source level is normalized to 0 dB re 1 μPa at 1m .

with $|\Phi_{S_{ij}{}^{Data}}(\mathbf{r}_{S_i}|\mathbf{r},\mathbf{r}_0,f)|^2$ being the measured reverberation level at $\mathbf{r}_{S_{ij}}$. Again, since the analysis in this section is restricted to one ping, the errors in Figure 4-3 are computed using $\langle\hat{\theta}\rangle$ for $p = 1$. Figure 4-8 shows the distribution of these errors for the entire polar area analyzed.

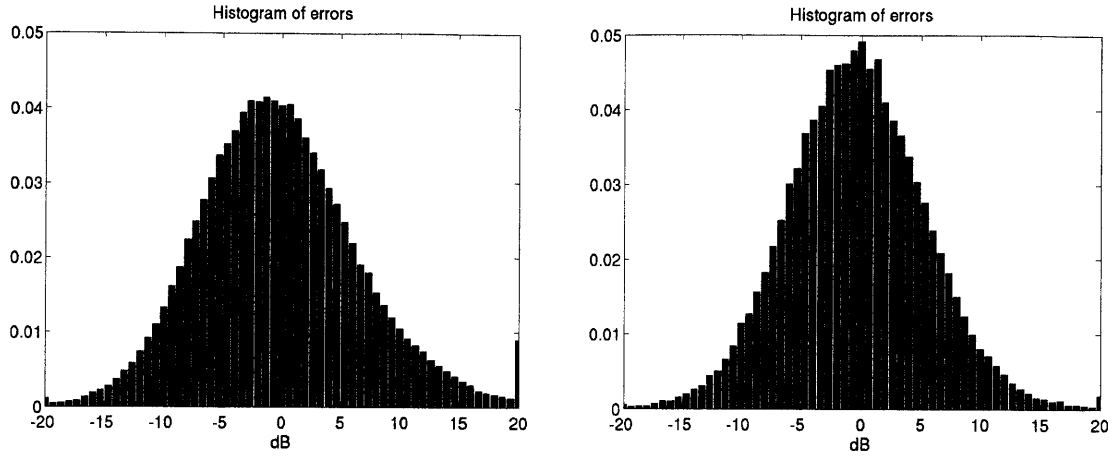

Figure 4-8: Histogram of the data-model differences as show in Figure 4-7 (bottom) for New Jersey (left) and Georges Bank (right). For the New Jersey errors (left), the mean is -1.1467 dB and the standard deviation 6.5095 dB. For the Georges Bank errors (right), the mean is -0.3526 dB and the standard deviation 5.8003 dB.

Appendix C presents calibration results for other pings at several frequencies. As the Appendix shows, for some of the pings recorded during the Georges Bank experiment at the center frequencies 950 and 1125 Hz, the model was found to underestimate the data for short ranges. Potential explanations may include returns that are not accounted for by the current approach, such as the use of too narrow of a vertical angle in the parabolic equation, fathometer returns, or returns due to multiple scattering.

4.5 Statistics and frequency dependence of inverted parameter

A systematic calibration of the model to data for multiple pings and frequencies for both the New Jersey and Georges Bank experiments allows us to determine the

second order statistics of the inverted parameter θ, which we tabulate in Table 4.1. The parameter θ, as given in Equation 4.4, is a function of the coherence volume V_C and the second order statistics of the bottom properties $\mathrm{Var}(\Gamma_\kappa(\mathbf{r}_t))$, $\mathrm{Var}(\Gamma_d(\mathbf{r}_t))$ and $\mathrm{Covar}(\Gamma_\kappa(\mathbf{r}_t))$, which we assume constant in depth and across the entire experimental site. Since 4.1 is an equation with four unknowns, the values for each of the bottom parameters cannot be estimated from θ. What we are most interested in, however, is the mean and variance of the parameter θ across the seafloor, for different frequencies and experimental locations.

		Data analyzed		Parameter statistics					
f (Hz)	Exper-iment*	p (# pings)	mp (# ping-beam samples)	$\langle\hat{\theta}\rangle$	$\langle\hat{\theta}\rangle$ (dB)	Std ($\hat{\theta}$)	Std($\hat{\theta}$) (dB)	% 1 std	% 2std
415	NJ	5	180	0.000117	-39.32	0.0000411	1.63	69.32	94.87
415	GB	4	85	0.000134	-38.73	0.0000461	1.47	74.70	95.18
925	NJ	4	144	0.0000032	-54.95	0.0000019	2.56	72.53	97.18
950	GB	4	99	0.0000059	-52.29	0.0000027	2.55	69.07	96.91
1325	NJ	4	144	0.0000019	-57.21	0.0000005	1.21	67.61	95.07
1125	GB	4	114	0.0000059	-52.29	0.0000022	1.73	66.36	96.36

Table 4.1: Table showing the results of the parameter estimation. The first two columns represent the corresponding center frequencies and experiment locations, respectively. The number of pings, p, and total ping-beam samples, mp, used in the analysis are given in the third and fourth columns, respectively. The next six columns give the mean (level and log scale), standard deviation (level and log scale), as well as the percentage of beam samples within one and two standard deviations, respectively. One $\hat{\theta}$ is estimated for each single beam in each single ping using Equation 4.6, where the summation is performed over all n resolution cells V_{S_i} along the particular beam. As mentioned in Figure 4-4, we typically sum over 1667 to 2333 resolution footprints along each beam. Then, the mean parameter estimate $\langle\hat{\theta}\rangle$ is obtained by averaging the parameter estimates $\hat{\theta}$ over all mp ping-beam samples, as given by Equation 4.7. (* the NJ and GB symbols stand for New Jersey and Georges Bank, respectively)

The inversion results summarized in Table 4.1 confirm that, for a certain frequency and for similar bottom sediments (in this case sand), the parameter estimates are consistent. For example, at 415 Hz, for both New Jersey and Georges Bank we found a parameter equal to about 0.0001, or negative 40 dB. This is also consistent with the parameter estimate $\hat{\theta}$ we would obtain if we used the bottom parameter statistics estimated by Galinde et al [6] for 415 Hz in New Jersey, summarized in Table 3.1.

Another observation is the fact that the value of the parameter decreases with

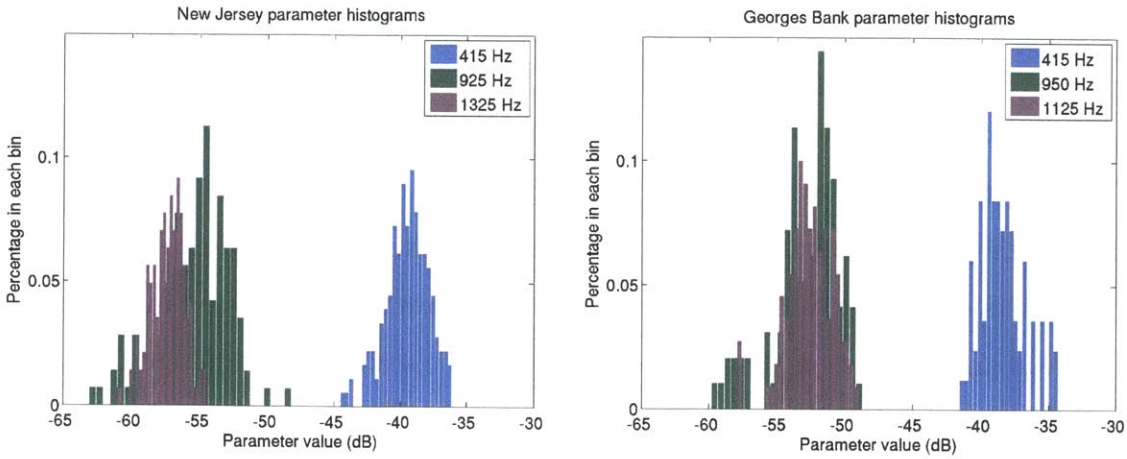

Figure 4-9: Histograms of parameter values (log scale), for the New Jersey (left) and Georges Bank (right) data.

frequency, except for Georges Bank, where the parameter θ remains stable from 950 to 1125 Hz. To clearly illustrate this result, we plot in Figure 4-9 the distributions of the inverted parameter estimates $\hat{\theta}$ using New Jersey and Georges Bank data at three frequencies for each case. In Figure 4-10 we also plot the mean and standard deviations of the estimated parameter $\hat{\theta}$ for both the New Jersey and Georges Bank data. Since the statistics of the bottom properties should be independent of frequency, the result supports our hypothesis from Section 3.2 that the acoustically determined coherence volume V_C varies inversely with frequency, to compensate for the frequency dependence of the k^4 factor in Equation 3.3. After fitting linear curves in log-log domain (Figure 4-11) through the data points for the mean estimates from figure 4-10, we find that the frequency dependence in the New Jersey case is $f^{-3.7}$, and in the Georges Bank case $f^{-3.3}$. This result is consistent with the wavelength dependence of scattered intensity found in speckle interferometry [9] and scintillation theory [2], [14]. For the case of volume scattering, when frequency dependence of scattered intensity is greatest [9], the inhomogeneities are selected over the wavelength scale in all three directions, leading to a dependence of approximately the wavelength cubed.

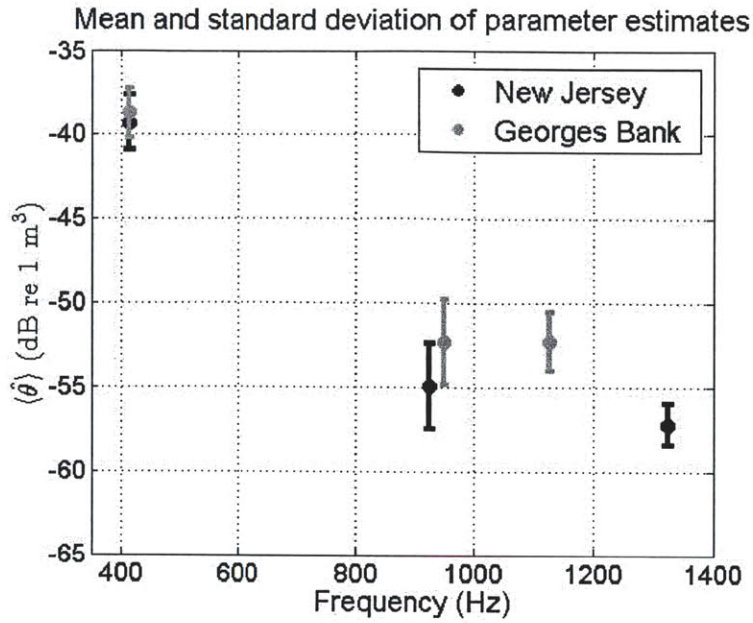

Figure 4-10: Mean (dots) and standard deviations (error bars) for the parameter estimate $\hat{\theta}$, as given in Table 4.1, for the New Jersey and Georges Bank data.

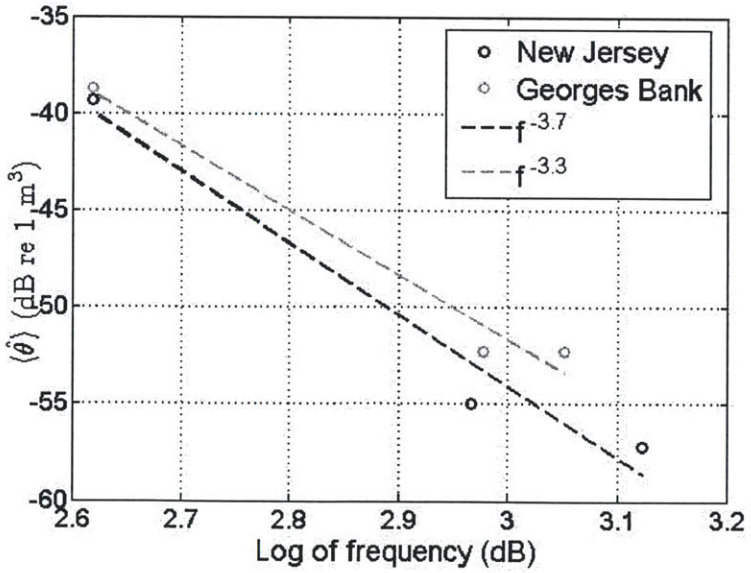

Figure 4-11: Mean parameter estimates $\hat{\theta}$ (circles), as given in Table 4.1, for the New Jersey and Georges Bank data, along with least squares fitted lines for each experiment.

Chapter 5

Conclusion

In this thesis, we derived full expressions for the total moments of the matched filtered scattered field, using the Green theorem application to the inhomogeneous wave equation and the Born single scatter approximation. We provided approximate expressions for the total scattered intensity, including a time harmonic approximation implemented in terms of the resolution footprint of the sonar. We showed, using Monte Carlo simulations of the Green function using actual sound speed profiles and a Pekeris waveguide, that the following are true: (1) the total matched filtered second moment can be approximated by the total matched filtered variance; (2) the total matched filtered variance can be approximated by its first term; (3) the first term of the total matched filtered variance can be approximated by the first term of the total time harmonic variance. Using the least squares method, we calibrated the computationally efficient time harmonic model to reverberation data collected during two experiments at sea, for several frequency ranges. We provided the statistics of the estimated parameter and discussed the frequency dependence of the model and parameters. We found that the acoustic signal selects seafloor scatterers of wavelength scale.

Appendix A

Matched filtered total moment expressions based on conditional moments

Instead of implementing the analytical expressions for the total moments of the matched filtered scattered field described in Section 2, we found it more efficient to implement the total moment expressions derived from conditional moment expressions as described in this section.

To derive the expressions for the total moments using conditional moments, we begin with Equation 2.7, for the matched filtered scattered field, which we repeat below as

$$\Phi_S(\mathbf{r}_S|\mathbf{r},\mathbf{r}_0,t_M) = (4\pi)\int_{f_c-B/2}^{f_c+B/2}\iiint_{V_S}[k^2\Gamma_\kappa(\mathbf{r}_t)G(\mathbf{r}_t|\mathbf{r}_0,f)G(\mathbf{r}|\mathbf{r}_t,f) + \Gamma_d(\mathbf{r}_t)\nabla G(\mathbf{r}_t|\mathbf{r}_0,f)\cdot\nabla G(\mathbf{r}|\mathbf{r}_t,f)] \times \frac{1}{\sqrt{E_0}}|Q(f)|^2 e^{-i2\pi f(t-t_M)}\,dV_t\,df. \tag{A.1}$$

Next, using the assumption that the bottom parameters are uncorrelated with the propagation Green functions, we condition on a deterministic set of Green functions $(G(\mathbf{r}_t|\mathbf{r}_0,f), G(\mathbf{r}|\mathbf{r}_t,f))$, and define the conditional mean for the matched filtered

scattered field as

$$\begin{aligned}
&\langle \Phi_S(\mathbf{r}_S|\mathbf{r},\mathbf{r}_0,t_M)|G(\mathbf{r}_t|\mathbf{r}_0,f),G(\mathbf{r}|\mathbf{r}_t,f)\rangle \qquad \text{(A.2)}\\
&= (4\pi)\int_{f_c-B/2}^{f_c+B/2}\iiint_{V_S}[k^2\langle\Gamma_\kappa(\mathbf{r}_t)\rangle G(\mathbf{r}_t|\mathbf{r}_0,f)G(\mathbf{r}|\mathbf{r}_t,f)\\
&+\langle\Gamma_d(\mathbf{r}_t)\rangle\nabla G(\mathbf{r}_t|\mathbf{r}_0,f)\cdot\nabla G(\mathbf{r}|\mathbf{r}_t,f)]\\
&\times\frac{1}{\sqrt{E_0}}|Q(f)|^2e^{-i2\pi f(t-t_M)}\,dV_t\,df.
\end{aligned}$$

The expression above is a function of the bottom parameters statistics $\langle\Gamma_\kappa\rangle$ and $\langle\Gamma_d\rangle$ and a deterministic set of Green functions $(G(\mathbf{r}_t|\mathbf{r}_0,f),G(\mathbf{r}|\mathbf{r}_t,f))$, which represent one realization of the ocean environment, where at every 500m in range we randomly selected a new sound speed profile from a large set of measured profiles.

The total matched filtered mean can then be expressed in terms of the conditional mean as

$$\langle\Phi_S(\mathbf{r}_S|\mathbf{r},\mathbf{r}_0,t_M)\rangle=\langle\langle\Phi_S(\mathbf{r}_S|\mathbf{r},\mathbf{r}_0,t_M)|G(\mathbf{r}_t|\mathbf{r}_0,f),G(\mathbf{r}|\mathbf{r}_t,f)\rangle\rangle. \qquad \text{(A.3)}$$

The expression above is equivalent to the analytic expression from Equation 2.8 and does not facilitate implementation. We are more interested in the formulations for the second moment and variance, which we derive in the remainder of this section.

The conditional second moment is now

$$\begin{aligned}
&\langle|\Phi_S(\mathbf{r}_S|\mathbf{r},\mathbf{r}_0,t_M)|^2|G(\mathbf{r}_t|\mathbf{r}_0,f),G(\mathbf{r}|\mathbf{r}_t,f)\rangle \qquad \text{(A.4)}\\
&=\langle(4\pi)\int_{f_c-B/2}^{f_c+B/2}\iiint_{V_S}[k^2\Gamma_\kappa(\mathbf{r}_t)G(\mathbf{r}_t|\mathbf{r}_0,f)G(\mathbf{r}|\mathbf{r}_t,f)\\
&\quad+\Gamma_d(\mathbf{r}_t)\nabla G(\mathbf{r}_t|\mathbf{r}_0,f)\cdot\nabla G(\mathbf{r}|\mathbf{r}_t,f)]\times\frac{1}{\sqrt{E_0}}|Q(f)|^2e^{-i2\pi f(t-t_M)}\,dV_t\,df\\
&\times(4\pi)\int_{f_c-B/2}^{f_c+B/2}\iiint_{V_S}[k'^2\Gamma_\kappa(\mathbf{r}'_t)G^*(\mathbf{r}'_t|\mathbf{r}_0,f')G^*(\mathbf{r}|\mathbf{r}'_t,f')\\
&\quad+\Gamma_d(\mathbf{r}'_t)\nabla G^*(\mathbf{r}'_t|\mathbf{r}_0,f')\cdot\nabla G^*(\mathbf{r}|\mathbf{r}'_t,f')]\times\frac{1}{\sqrt{E_0}}|Q(f')|^2e^{-i2\pi f'(t-t_M)}\,dV'_t\,df'\rangle,
\end{aligned}$$

and can be written as

$$\begin{aligned}
&\langle|\Phi_S(\mathbf{r}_S|\mathbf{r},\mathbf{r}_0,t_M)|^2|G(\mathbf{r}_t|\mathbf{r}_0,f),G(\mathbf{r}|\mathbf{r}_t,f)\rangle \qquad (A.5)\\
&= (4\pi)^2\int_{f_c-B/2}^{f_c+B/2}\int_{f_c-B/2}^{f_c+B/2}\iiint_{V_S}\iiint_{V_S}\\
&\quad [k^2k'^2\langle\Gamma_\kappa(\mathbf{r}_t)\Gamma_\kappa(\mathbf{r}'_t)\rangle G(\mathbf{r}_t|\mathbf{r}_0,f)G(\mathbf{r}|\mathbf{r}_t,f)G^*(\mathbf{r}'_t|\mathbf{r}_0,f')G^*(\mathbf{r}|\mathbf{r}'_t,f')\\
&\quad + \langle\Gamma_d(\mathbf{r}_t)\Gamma_d(\mathbf{r}'_t)\rangle\nabla G(\mathbf{r}_t|\mathbf{r}_0,f)\cdot\nabla G(\mathbf{r}|\mathbf{r}_t,f)\times\nabla G^*(\mathbf{r}'_t|\mathbf{r}_0,f')\cdot\nabla G^*(\mathbf{r}|\mathbf{r}'_t,f')\\
&\quad + k^2\langle\Gamma_\kappa(\mathbf{r}_t)\Gamma_d(\mathbf{r}'_t)\rangle G(\mathbf{r}_t|\mathbf{r}_0,f)G(\mathbf{r}|\mathbf{r}_t,f)\nabla G^*(\mathbf{r}'_t|\mathbf{r}_0,f')\cdot\nabla G^*(\mathbf{r}|\mathbf{r}'_t,f')\\
&\quad + k'^2\langle\Gamma_\kappa(\mathbf{r}'_t)\Gamma_d(\mathbf{r}_t)\rangle G^*(\mathbf{r}'_t|\mathbf{r}_0,f')G^*(\mathbf{r}|\mathbf{r}'_t,f')\nabla G(\mathbf{r}_t|\mathbf{r}_0,f)\cdot\nabla G(\mathbf{r}|\mathbf{r}_t,f)]\\
&\quad \times\frac{1}{E_0}|Q(f)|^2|Q(f')|^2e^{-i2\pi(f-f')(t-t_M)}\,dV_t\,dV'_t\,df\,df'.
\end{aligned}$$

Note that there are now no expectations around the Green function products, as the Green function and its gradients are assumed deterministic. We can further simplify this expression, using Equations 2.11 and 2.12, to obtain

$$\begin{aligned}
&\langle|\Phi_S(\mathbf{r}_S|\mathbf{r},\mathbf{r}_0,t_M)|^2|G(\mathbf{r}_t|\mathbf{r}_0,f),G(\mathbf{r}|\mathbf{r}_t,f)\rangle \qquad (A.6)\\
&= (4\pi)^2\int_{f_c-B/2}^{f_c+B/2}\int_{f_c-B/2}^{f_c+B/2}\iiint_{V_S}\iiint_{V_S}V_c(\mathbf{r}_S,z_t)\\
&\quad \times[k^2k'^2\mathrm{Var}(\Gamma_\kappa)\delta(\mathbf{r}_t-\mathbf{r}'_t)G(\mathbf{r}_t|\mathbf{r}_0,f)G(\mathbf{r}|\mathbf{r}_t,f)G^*(\mathbf{r}'_t|\mathbf{r}_0,f')G^*(\mathbf{r}|\mathbf{r}'_t,f')\\
&\quad + \mathrm{Var}(\Gamma_d)\delta(\mathbf{r}_t-\mathbf{r}'_t)\nabla G(\mathbf{r}_t|\mathbf{r}_0,f)\cdot\nabla G(\mathbf{r}|\mathbf{r}_t,f)\times\nabla G^*(\mathbf{r}'_t|\mathbf{r}_0,f')\cdot\nabla G^*(\mathbf{r}|\mathbf{r}'_t,f')\\
&\quad + k^2\mathrm{Covar}(\Gamma_\kappa,\Gamma_d)\delta(\mathbf{r}_t-\mathbf{r}'_t)G(\mathbf{r}_t|\mathbf{r}_0,f)G(\mathbf{r}|\mathbf{r}_t,f)\nabla G^*(\mathbf{r}'_t|\mathbf{r}_0,f')\cdot\nabla G^*(\mathbf{r}|\mathbf{r}'_t,f')\\
&\quad + k'^2\mathrm{Covar}(\Gamma_\kappa,\Gamma_d)\delta(\mathbf{r}_t-\mathbf{r}'_t)G^*(\mathbf{r}'_t|\mathbf{r}_0,f')G^*(\mathbf{r}|\mathbf{r}'_t,f')\nabla G(\mathbf{r}_t|\mathbf{r}_0,f)\cdot\nabla G(\mathbf{r}|\mathbf{r}_t,f)]\\
&\quad \times\frac{1}{E_0}|Q(f)|^2|Q(f')|^2e^{-i2\pi(f-f')(t-t_M)}\,dV_t\,dV'_t\,df\,df'+
\end{aligned}$$

$$
\begin{aligned}
&+ (4\pi)^2 \int_{f_c-B/2}^{f_c+B/2} \int_{f_c-B/2}^{f_c+B/2} \iiint_{V_S} \iiint_{V_S} \\
&\quad \times [k^2 k'^2 \langle \Gamma_\kappa(\mathbf{r}_t) \rangle \langle \Gamma_\kappa(\mathbf{r}'_t) \rangle G(\mathbf{r}_t|\mathbf{r}_0, f) G(\mathbf{r}|\mathbf{r}_t, f) G^*(\mathbf{r}'_t|\mathbf{r}_0, f') G^*(\mathbf{r}|\mathbf{r}'_t, f') \\
&\quad + \langle \Gamma_d(\mathbf{r}_t) \rangle \langle \Gamma_d(\mathbf{r}'_t) \rangle \nabla G(\mathbf{r}_t|\mathbf{r}_0, f) \cdot \nabla G(\mathbf{r}|\mathbf{r}_t, f) \times \nabla G^*(\mathbf{r}'_t|\mathbf{r}_0, f') \cdot \nabla G^*(\mathbf{r}|\mathbf{r}'_t, f') \\
&\quad + k^2 \langle \Gamma_\kappa(\mathbf{r}_t) \rangle \langle \Gamma_d(\mathbf{r}'_t) \rangle G(\mathbf{r}_t|\mathbf{r}_0, f) G(\mathbf{r}|\mathbf{r}_t, f) \nabla G^*(\mathbf{r}'_t|\mathbf{r}_0, f') \cdot \nabla G^*(\mathbf{r}|\mathbf{r}'_t, f') \\
&\quad + k'^2 \langle \Gamma_\kappa(\mathbf{r}'_t) \rangle \langle \Gamma_d(\mathbf{r}_t) \rangle G^*(\mathbf{r}'_t|\mathbf{r}_0, f') G^*(\mathbf{r}|\mathbf{r}'_t, f') \nabla G(\mathbf{r}_t|\mathbf{r}_0, f) \cdot \nabla G(\mathbf{r}|\mathbf{r}_t, f)] \\
&\quad \times \frac{1}{E_0} |Q(f)|^2 |Q(f')|^2 e^{-i2\pi(f-f')(t-t_M)} \, dV_t \, dV'_t \, df \, df'.
\end{aligned}
$$

By canceling the delta function with one of the volume integrals in the first term, we have

$$
\begin{aligned}
&\langle |\Phi_S(\mathbf{r}_S|\mathbf{r}, \mathbf{r}_0, t_M)|^2 | G(\mathbf{r}_t|\mathbf{r}_0, f), G(\mathbf{r}|\mathbf{r}_t, f) \rangle \qquad \text{(A.7)} \\
&= (4\pi)^2 \int_{f_c-B/2}^{f_c+B/2} \int_{f_c-B/2}^{f_c+B/2} \iiint_{V_S} V_c(\mathbf{r}_S, z_t) \\
&\quad \times [k^2 k'^2 \mathrm{Var}(\Gamma_\kappa) G(\mathbf{r}_t|\mathbf{r}_0, f) G(\mathbf{r}|\mathbf{r}_t, f) G^*(\mathbf{r}_t|\mathbf{r}_0, f') G^*(\mathbf{r}|\mathbf{r}_t, f') \\
&\quad + \mathrm{Var}(\Gamma_d) \nabla G(\mathbf{r}_t|\mathbf{r}_0, f) \cdot \nabla G(\mathbf{r}|\mathbf{r}_t, f) \times \nabla G^*(\mathbf{r}_t|\mathbf{r}_0, f') \cdot \nabla G^*(\mathbf{r}|\mathbf{r}_t, f') \\
&\quad + k^2 \mathrm{Covar}(\Gamma_\kappa, \Gamma_d) G(\mathbf{r}_t|\mathbf{r}_0, f) G(\mathbf{r}|\mathbf{r}_t, f) \nabla G^*(\mathbf{r}_t|\mathbf{r}_0, f') \cdot \nabla G^*(\mathbf{r}|\mathbf{r}_t, f') \\
&\quad + k'^2 \mathrm{Covar}(\Gamma_\kappa, \Gamma_d) G^*(\mathbf{r}_t|\mathbf{r}_0, f') G^*(\mathbf{r}|\mathbf{r}_t, f') \nabla G(\mathbf{r}_t|\mathbf{r}_0, f) \cdot \nabla G(\mathbf{r}|\mathbf{r}_t, f)] \\
&\quad \times \frac{1}{E_0} |Q(f)|^2 |Q(f')|^2 e^{-i2\pi(f-f')(t-t_M)} \, dV_t \, df \, df' + \\
&+ (4\pi)^2 \int_{f_c-B/2}^{f_c+B/2} \int_{f_c-B/2}^{f_c+B/2} \iiint_{V_S} \iiint_{V_S} \\
&\quad \times [k^2 k'^2 \langle \Gamma_\kappa(\mathbf{r}_t) \rangle \langle \Gamma_\kappa(\mathbf{r}'_t) \rangle G(\mathbf{r}_t|\mathbf{r}_0, f) G(\mathbf{r}|\mathbf{r}_t, f) G^*(\mathbf{r}'_t|\mathbf{r}_0, f') G^*(\mathbf{r}|\mathbf{r}'_t, f') \\
&\quad + \langle \Gamma_d(\mathbf{r}_t) \rangle \langle \Gamma_d(\mathbf{r}'_t) \rangle \nabla G(\mathbf{r}_t|\mathbf{r}_0, f) \cdot \nabla G(\mathbf{r}|\mathbf{r}_t, f) \times \nabla G^*(\mathbf{r}'_t|\mathbf{r}_0, f') \cdot \nabla G^*(\mathbf{r}|\mathbf{r}'_t, f') \\
&\quad + k^2 \langle \Gamma_\kappa(\mathbf{r}_t) \rangle \langle \Gamma_d(\mathbf{r}'_t) \rangle G(\mathbf{r}_t|\mathbf{r}_0, f) G(\mathbf{r}|\mathbf{r}_t, f) \nabla G^*(\mathbf{r}'_t|\mathbf{r}_0, f') \cdot \nabla G^*(\mathbf{r}|\mathbf{r}'_t, f') \\
&\quad + k'^2 \langle \Gamma_\kappa(\mathbf{r}'_t) \rangle \langle \Gamma_d(\mathbf{r}_t) \rangle G^*(\mathbf{r}'_t|\mathbf{r}_0, f') G^*(\mathbf{r}|\mathbf{r}'_t, f') \nabla G(\mathbf{r}_t|\mathbf{r}_0, f) \cdot \nabla G(\mathbf{r}|\mathbf{r}_t, f)] \\
&\quad \times \frac{1}{E_0} |Q(f)|^2 |Q(f')|^2 e^{-i2\pi(f-f')(t-t_M)} \, dV_t \, dV'_t \, df \, df'.
\end{aligned}
$$

By inspection, however, we notice that the last term in the above equation is the

magnitude squared of the conditional mean expression from Equation A.2:

$$
\begin{aligned}
&|\langle \Phi_S(\mathbf{r}_S|\mathbf{r},\mathbf{r}_0,t_M)|G(\mathbf{r}_t|\mathbf{r}_0,f),G(\mathbf{r}|\mathbf{r}_t,f)\rangle|^2 \qquad \text{(A.8)}\\
&\quad = (4\pi)^2 \int_{f_c-B/2}^{f_c+B/2}\int_{f_c-B/2}^{f_c+B/2}\iiint_{V_S}\iiint_{V_S}\\
&\qquad \times [k^2k'^2\langle\Gamma_\kappa(\mathbf{r}_t)\rangle\langle\Gamma_\kappa(\mathbf{r}'_t)\rangle G(\mathbf{r}_t|\mathbf{r}_0,f)G(\mathbf{r}|\mathbf{r}_t,f)G^*(\mathbf{r}'_t|\mathbf{r}_0,f')G^*(\mathbf{r}|\mathbf{r}'_t,f')\\
&\qquad + \langle\Gamma_d(\mathbf{r}_t)\rangle\langle\Gamma_d(\mathbf{r}'_t)\rangle\nabla G(\mathbf{r}_t|\mathbf{r}_0,f)\cdot\nabla G(\mathbf{r}|\mathbf{r}_t,f)\times\nabla G^*(\mathbf{r}'_t|\mathbf{r}_0,f')\cdot\nabla G^*(\mathbf{r}|\mathbf{r}'_t,f')\\
&\qquad + k^2\langle\Gamma_\kappa(\mathbf{r}_t)\rangle\langle\Gamma_d(\mathbf{r}'_t)\rangle G(\mathbf{r}_t|\mathbf{r}_0,f)G(\mathbf{r}|\mathbf{r}_t,f)\nabla G^*(\mathbf{r}'_t|\mathbf{r}_0,f')\cdot\nabla G^*(\mathbf{r}|\mathbf{r}'_t,f')\\
&\qquad + k'^2\langle\Gamma_\kappa(\mathbf{r}'_t)\rangle\langle\Gamma_d(\mathbf{r}_t)\rangle G^*(\mathbf{r}'_t|\mathbf{r}_0,f')G^*(\mathbf{r}|\mathbf{r}'_t,f')\nabla G(\mathbf{r}_t|\mathbf{r}_0,f)\cdot\nabla G(\mathbf{r}|\mathbf{r}_t,f)]\\
&\qquad \times \frac{1}{E_0}|Q(f)|^2|Q(f')|^2e^{-i2\pi(f-f')(t-t_M)}\,dV_t\,dV'_t\,df\,df'.
\end{aligned}
$$

We can also note that the first term of Equation A.7 is the conditional variance

$$
\begin{aligned}
&\mathrm{Var}(\Phi_S(\mathbf{r}_S|\mathbf{r},\mathbf{r}_0,t_M)|G(\mathbf{r}_t|\mathbf{r}_0,f),G(\mathbf{r}|\mathbf{r}_t,f)) \qquad \text{(A.9)}\\
&\quad = \langle|\Phi_S(\mathbf{r}_S|\mathbf{r},\mathbf{r}_0,t_M)|^2|G(\mathbf{r}_t|\mathbf{r}_0,f),G(\mathbf{r}|\mathbf{r}_t,f)\rangle\\
&\qquad - |\langle\Phi_S(\mathbf{r}_S|\mathbf{r},\mathbf{r}_0,t_M)|G(\mathbf{r}_t|\mathbf{r}_0,f),G(\mathbf{r}|\mathbf{r}_t,f)\rangle|^2\\
&\quad = (4\pi)^2 \int_{f_c-B/2}^{f_c+B/2}\int_{f_c-B/2}^{f_c+B/2}\iiint_{V_S} V_c(\mathbf{r}_S,z_t)\\
&\qquad \times [k^2k'^2\mathrm{Var}(\Gamma_\kappa)G(\mathbf{r}_t|\mathbf{r}_0,f)G(\mathbf{r}|\mathbf{r}_t,f)G^*(\mathbf{r}_t|\mathbf{r}_0,f')G^*(\mathbf{r}|\mathbf{r}_t,f')\\
&\qquad + \mathrm{Var}(\Gamma_d)\nabla G(\mathbf{r}_t|\mathbf{r}_0,f)\cdot\nabla G(\mathbf{r}|\mathbf{r}_t,f)\times\nabla G^*(\mathbf{r}_t|\mathbf{r}_0,f')\cdot\nabla G^*(\mathbf{r}|\mathbf{r}_t,f')\\
&\qquad + k^2\mathrm{Covar}(\Gamma_\kappa,\Gamma_d)G(\mathbf{r}_t|\mathbf{r}_0,f)G(\mathbf{r}|\mathbf{r}_t,f)\nabla G^*(\mathbf{r}_t|\mathbf{r}_0,f')\cdot\nabla G^*(\mathbf{r}|\mathbf{r}_t,f')\\
&\qquad + k'^2\mathrm{Covar}(\Gamma_\kappa,\Gamma_d)G^*(\mathbf{r}_t|\mathbf{r}_0,f')G^*(\mathbf{r}|\mathbf{r}_t,f')\nabla G(\mathbf{r}_t|\mathbf{r}_0,f)\cdot\nabla G(\mathbf{r}|\mathbf{r}_t,f)]\\
&\qquad \times \frac{1}{E_0}|Q(f)|^2|Q(f')|^2e^{-i2\pi(f-f')(t-t_M)}\,dV_t\,df\,df'.
\end{aligned}
$$

(A.10)

Then, the conditional second moment can be expressed as

$$\begin{aligned}
&\langle|\Phi_S(\mathbf{r}_S|\mathbf{r},\mathbf{r}_0,t_M)|^2|G(\mathbf{r}_t|\mathbf{r}_0,f),G(\mathbf{r}|\mathbf{r}_t,f)\rangle \\
&\quad=\mathrm{Var}(\Phi_S(\mathbf{r}_S|\mathbf{r},\mathbf{r}_0,t_M)|G(\mathbf{r}_t|\mathbf{r}_0,f),G(\mathbf{r}|\mathbf{r}_t,f)) \\
&\quad+|\langle\Phi_S(\mathbf{r}_S|\mathbf{r},\mathbf{r}_0,t_M)|G(\mathbf{r}_t|\mathbf{r}_0,f),G(\mathbf{r}|\mathbf{r}_t,f)\rangle|^2,
\end{aligned} \tag{A.11}$$

and the total second moment as

$$\begin{aligned}
\langle|\Phi_S(\mathbf{r}_S|\mathbf{r},\mathbf{r}_0,t_M)|^2\rangle &= \langle\langle|\Phi_S(\mathbf{r}_S|\mathbf{r},\mathbf{r}_0,t_M)|^2|G(\mathbf{r}_t|\mathbf{r}_0,f),G(\mathbf{r}|\mathbf{r}_t,f)\rangle\rangle \\
&=\langle\mathrm{Var}(\Phi_S(\mathbf{r}_S|\mathbf{r},\mathbf{r}_0,t_M)|G(\mathbf{r}_t|\mathbf{r}_0,f),G(\mathbf{r}|\mathbf{r}_t,f))\rangle \\
&+\langle|\langle\Phi_S(\mathbf{r}_S|\mathbf{r},\mathbf{r}_0,t_M)|G(\mathbf{r}_t|\mathbf{r}_0,f),G(\mathbf{r}|\mathbf{r}_t,f)\rangle|^2\rangle,
\end{aligned} \tag{A.12}$$

where the conditional variance $\mathrm{Var}(\Phi_S(\mathbf{r}_S|\mathbf{r},\mathbf{r}_0,t_M)|G(\mathbf{r}_t|\mathbf{r}_0,f),G(\mathbf{r}|\mathbf{r}_t,f))$ and the conditional mean $\langle\Phi_S(\mathbf{r}_S|\mathbf{r},\mathbf{r}_0,t_M)|G(\mathbf{r}_t|\mathbf{r}_0,f),G(\mathbf{r}|\mathbf{r}_t,f)\rangle$ are as given in Equations A.9 and A.2 respectively. This expression is easier to implement than Equation 2.16 in Section 2.2, which has a double integral over volume.

To derive the total variance based on the conditional expressions derived above, we use the fact that the total variance is the difference between the total second moment and the magnitude squared of the total mean

$$\begin{aligned}
&\mathrm{Var}(\Phi_S(\mathbf{r}_S|\mathbf{r},\mathbf{r}_0,t_M)) \\
&\quad=\langle|\Phi_S(\mathbf{r}_S|\mathbf{r},\mathbf{r}_0,t_M)|^2\rangle-|\langle\Phi_S(\mathbf{r}_S|\mathbf{r},\mathbf{r}_0,t_M)\rangle|^2
\end{aligned} \tag{A.13}$$

By applying Equations A.12 and A.3, we find that the total matched filtered variance is

$$\begin{aligned}
&\mathrm{Var}(\Phi_S(\mathbf{r}_S|\mathbf{r},\mathbf{r}_0,t_M)) \\
&\quad=\langle\mathrm{Var}(\Phi_S(\mathbf{r}_S|\mathbf{r},\mathbf{r}_0,t_M)|G(\mathbf{r}_t|\mathbf{r}_0,f),G(\mathbf{r}|\mathbf{r}_t,f))\rangle \\
&\qquad+\langle|\langle\Phi_S(\mathbf{r}_S|\mathbf{r},\mathbf{r}_0,t_M)|G(\mathbf{r}_t|\mathbf{r}_0,f),G(\mathbf{r}|\mathbf{r}_t,f)\rangle|^2\rangle \\
&\qquad-|\langle\langle\Phi_S(\mathbf{r}_S|\mathbf{r},\mathbf{r}_0,t_M)|G(\mathbf{r}_t|\mathbf{r}_0,f),G(\mathbf{r}|\mathbf{r}_t,f)\rangle\rangle|^2.
\end{aligned} \tag{A.14}$$

Equation A.14 is also easier to implement than the full expression for the total matched filtered variance given in Equation 2.18, due to the fact none of its terms have a double integral over the volume V_S. To note is also that the first term in Equation A.14 is equivalent to the expression given in Equation 2.19:

$$
\begin{aligned}
&\langle \mathrm{Var}(\Phi_S(\mathbf{r}_S|\mathbf{r},\mathbf{r}_0,t_M)|G(\mathbf{r}_t|\mathbf{r}_0,f),G(\mathbf{r}|\mathbf{r}_t,f))\rangle \qquad \text{(A.15)}\\
&\quad = (4\pi)^2 \int_{f_c-B/2}^{f_c+B/2}\int_{f_c-B/2}^{f_c+B/2}\iiint_{V_S} V_c(\mathbf{r}_S,z_t)\\
&\qquad \times [k^2k'^2\mathrm{Var}(\Gamma_\kappa)\langle G(\mathbf{r}_t|\mathbf{r}_0,f)G(\mathbf{r}|\mathbf{r}_t,f)G^*(\mathbf{r}_t|\mathbf{r}_0,f')G^*(\mathbf{r}|\mathbf{r}_t,f')\rangle\\
&\qquad + \mathrm{Var}(\Gamma_d)\langle \boldsymbol{\nabla}G(\mathbf{r}_t|\mathbf{r}_0,f)\cdot\boldsymbol{\nabla}G(\mathbf{r}|\mathbf{r}_t,f)\times\boldsymbol{\nabla}G^*(\mathbf{r}_t|\mathbf{r}_0,f')\cdot\boldsymbol{\nabla}G^*(\mathbf{r}|\mathbf{r}_t,f')\rangle\\
&\qquad + k^2\mathrm{Covar}(\Gamma_\kappa,\Gamma_d)\langle G(\mathbf{r}_t|\mathbf{r}_0,f)G(\mathbf{r}|\mathbf{r}_t,f)\boldsymbol{\nabla}G^*(\mathbf{r}_t|\mathbf{r}_0,f')\cdot\boldsymbol{\nabla}G^*(\mathbf{r}|\mathbf{r}_t,f')\rangle\\
&\qquad + k'^2\mathrm{Covar}(\Gamma_\kappa,\Gamma_d)\langle G^*(\mathbf{r}_t|\mathbf{r}_0,f')G^*(\mathbf{r}|\mathbf{r}_t,f')\boldsymbol{\nabla}G(\mathbf{r}_t|\mathbf{r}_0,f)\cdot\boldsymbol{\nabla}G(\mathbf{r}|\mathbf{r}_t,f)\rangle]\\
&\qquad \times \frac{1}{E_0}|Q(f)|^2|Q(f')|^2 e^{-i2\pi(f-f')(t-t_M)}\,dV_t\,df\,df',
\end{aligned}
$$

and can be used to approximate the total matched filtered scattered intensity.

Appendix B

Second term of the time harmonic total variance

In section 3.1 we showed that the time harmonic expression in Equation 2.21 provides a good approximation to the matched filtered scattered intensity. Equation 2.21, however, corresponds to only the first term of the total time harmonic variance, given by Equation 2.20. Numerically, we haven't been able to show that the first term of Equation 2.20 dominates the total time harmonic variance. While the third term of Equation 2.20 becomes negligible for a fine range increment and for several realizations of the ocean environment, the second term is independent of the number of realizations, and even for a fine range increment, dominates or is comparable to the first term. This was not the case for the second term of the total matched filtered variance given in Equation 2.18, where both the second and the third terms have been shown to be negligible (Figures 3-5 and 3-6). We believe that the dominance of the second term in Equation 2.20 is an artifact of the time harmonic approximation, which cannot approximate a finite duration pulse and so cannot resolve a scattering patch. Implementing the time harmonic approximation is effectively equivalent to using a continuous wave CW waveform of infinite duration. We show in this Appendix that while a 1 second long CW waveform renders results similar to the linear frequency modulated (LFM), increasing the duration of the CW signal reduces the range resolution and consequently overestimates the second term in Equation 2.18 for

the matched filtered variance.

The simulation in this appendix was performed for an actual New Jersey continental shelf environment approximately 80 m deep. Monte Carlo simulations using actual sound speed profiles have been run to randomize the waveguide and to allow computation of the total moments. The depth and range increments used were $dz = 0.4$ m and $dr = 3$ m, respectively. The single element source and receiver were collocated and situated at 50 m in depth. The integration patch V_S extended over the top 10 m layers in depth, from 100 m to 5,500 m in range and over a 3° angle in azimuth. The center frequency and bandwidth were 415 Hz and 50 Hz, respectively, for all waveforms considered.

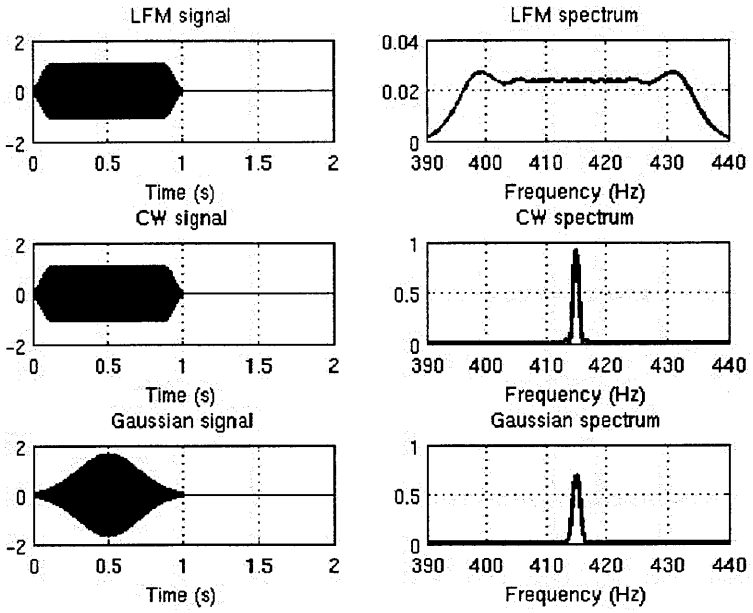

Figure B-1: Real part (left) and source spectrum $Q(f)^2$ for 1 second long LFM (top), CW (middle) and Gaussian (bottom) waveforms.

We first wish to study the effect that the choice of waveform has on the simulated reverberation and in particular to determine whether the first term of the total matched filtered variance dominates for all three waveforms. We consider the LFM waveform typically used in experiments, along with the CW and Gaussian waveforms. We keep the signal duration τ constant to 1 second for all three waveforms. The real

part of the time domain signal and the corresponding normalized spectra $Q(f)^2$ for each waveform are depicted in Figure B-1. As expected, the CW and Gaussian waveforms have a much narrower bandwidth than the LFM. To obtain consistent results for the simulated reverberation using all three waveforms, we normalize by the time-bandwidth product τB. Figure B-2 shows that, indeed, the simulated reverberation level using the first term of the matched filtered variance given in Equation 2.19, is consistent for the three waveforms.

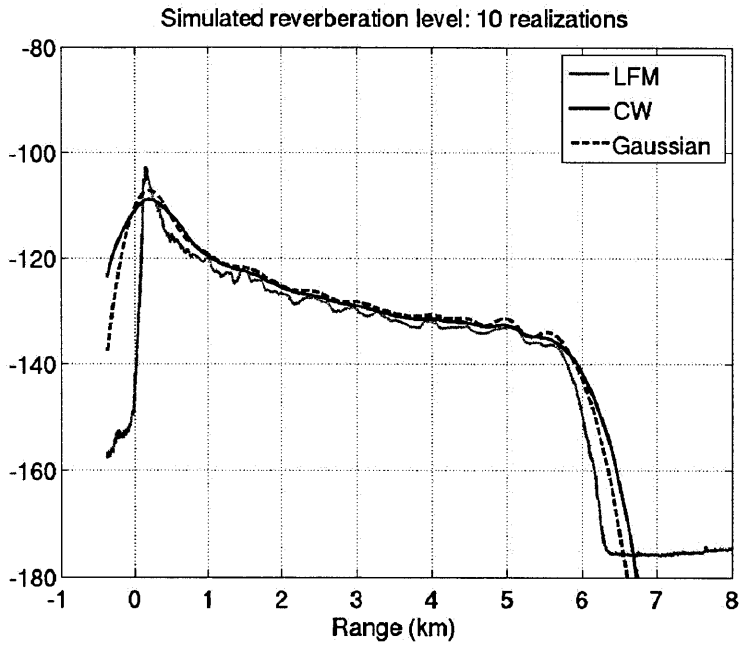

Figure B-2: Simulated reverberation level using the first term of the matched filtered total variance for 10 Monte Carlo simulations, after normalization by τB, for LFM, CW and Gaussian 1 second long broadband pulses centered at 415 Hz and with 50 Hz bandwidth.

While we confirmed that the three waveforms give consistent results, we also wish to verify whether the second and third terms of the full matched filtered variance given in Equation 2.18 are negligible compared to the first term. Figure B-3 shows the total matched filtered variance and its three terms, for 10 Monte Carlo realizations, for the LFM, CW and Gaussian waveforms. For all three waveforms, the first term dominates, while the second and third terms are negligible. As the range resolution $\Delta r = \frac{c}{2B}$, where c is the sound speed and B is the bandwidth, the CW and Gaussian

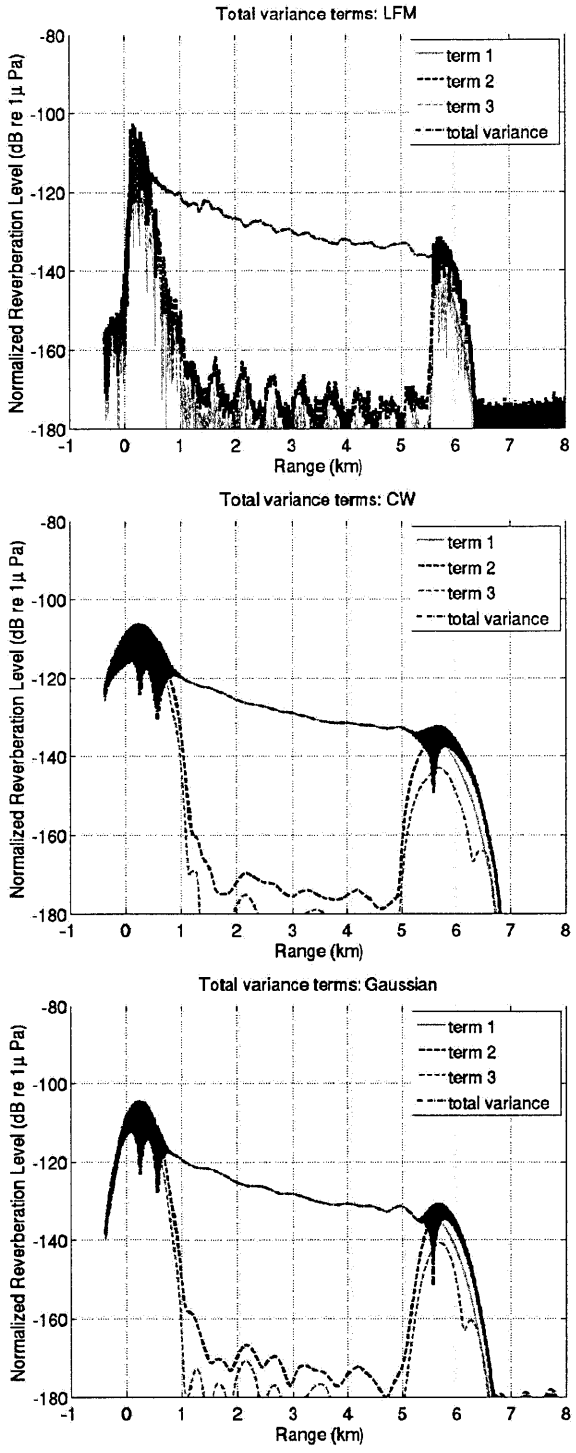

Figure B-3: Total matched filtered variance and its three terms, for 1 second LFM, CW and Gaussian broadband pulses centered at 415 Hz with 50 Hz bandwidth.

pulses, with much narrower bandwidth than the LFM, offer a worse range resolution. This explains why the plots of the CW and Gaussian variance terms in Figure B-3 are smoother than the corresponding LFM plots. As the signal duration τ increases, the range resolution of the CW waveform decreases even further. The two peaks in the second term found at the end points of the patch due to discontinuity of the medium could, then, overlap for a certain value of τ, causing the second term to be at the level of the two peaks. The next part of the Appendix studies the behavior of the second term as the duration τ of the CW signal increases.

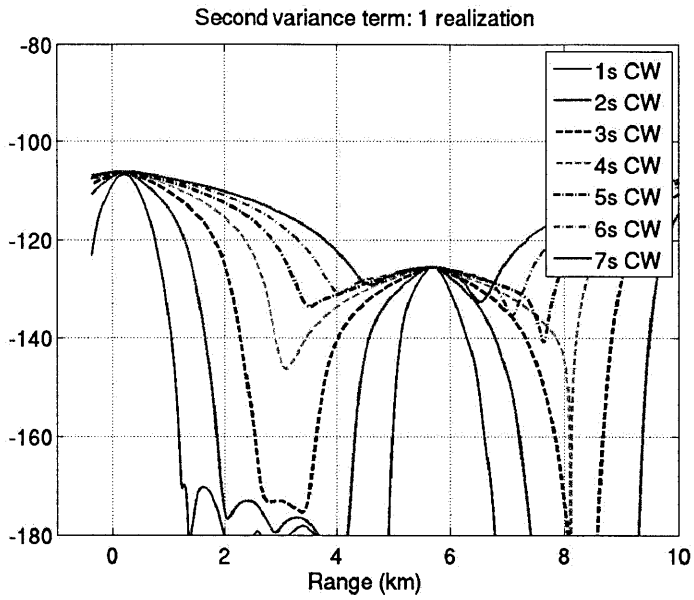

Figure B-4: Second term of total variance (Equation 2.18) for 1 Monte Carlo simulation, for CW pulses of 1 to 7 second duration, centered at 415 Hz and with 50 Hz bandwidth.

To study the behavior of the second term as the duration τ of the CW signal increases, we only need to consider one realization of the ocean waveguide, as the average level of the second term has been found to remain constant across realizations. We consider CW pulses of durations $\tau = 1$ to 7 s, and plot in Figure B-4 the second term of the matched filtered variance (Equation 2.18) for each τ, for one realization of the ocean waveguide. The figure shows that, as the signal time duration increases, the peaks at the edges of the patch become wider, and begin to overlap. For a

hypothetical CW pulse of infinite time duration, even if wrap-around would not be problem and the time window for the fourier transform was large, the two peaks would still overlap and form a monotonous curve, causing an apparent dominance of the second term.

Appendix C

Examples of calibration results for each experiment and frequency

C.1 New Jersey, 415 Hz

Implementation to New Jersey data, 415Hz, ping fora2003jd133t143135.

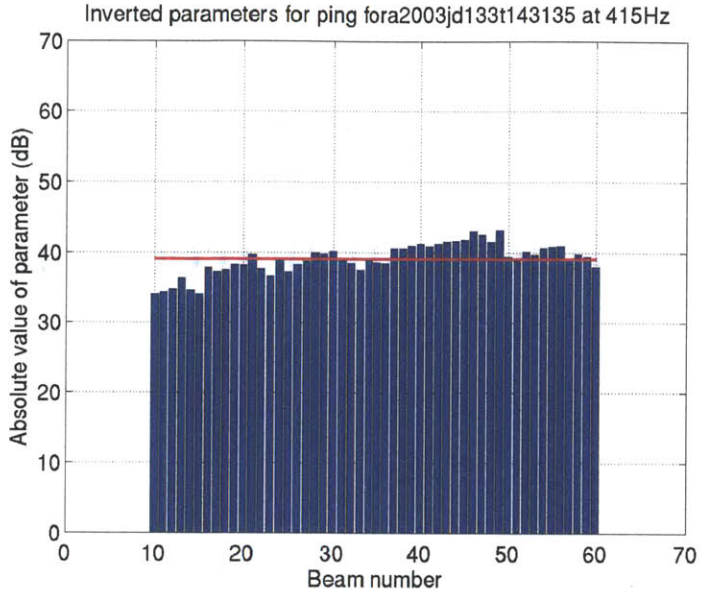

Figure C-1: Parameters obtained after fitting the model to the data for each beam, in log scale. The red horizontal line indicates the mean of the parameter values (log scale). Only beams corresponding to relatively flat or downward sloping bathymetry were included in the analysis. Endfire beams as well as beams contaminated by clutter were also excluded. The second half of the data and model time series were chosen for calibration, as the model fails to predict well the data for small ranges.

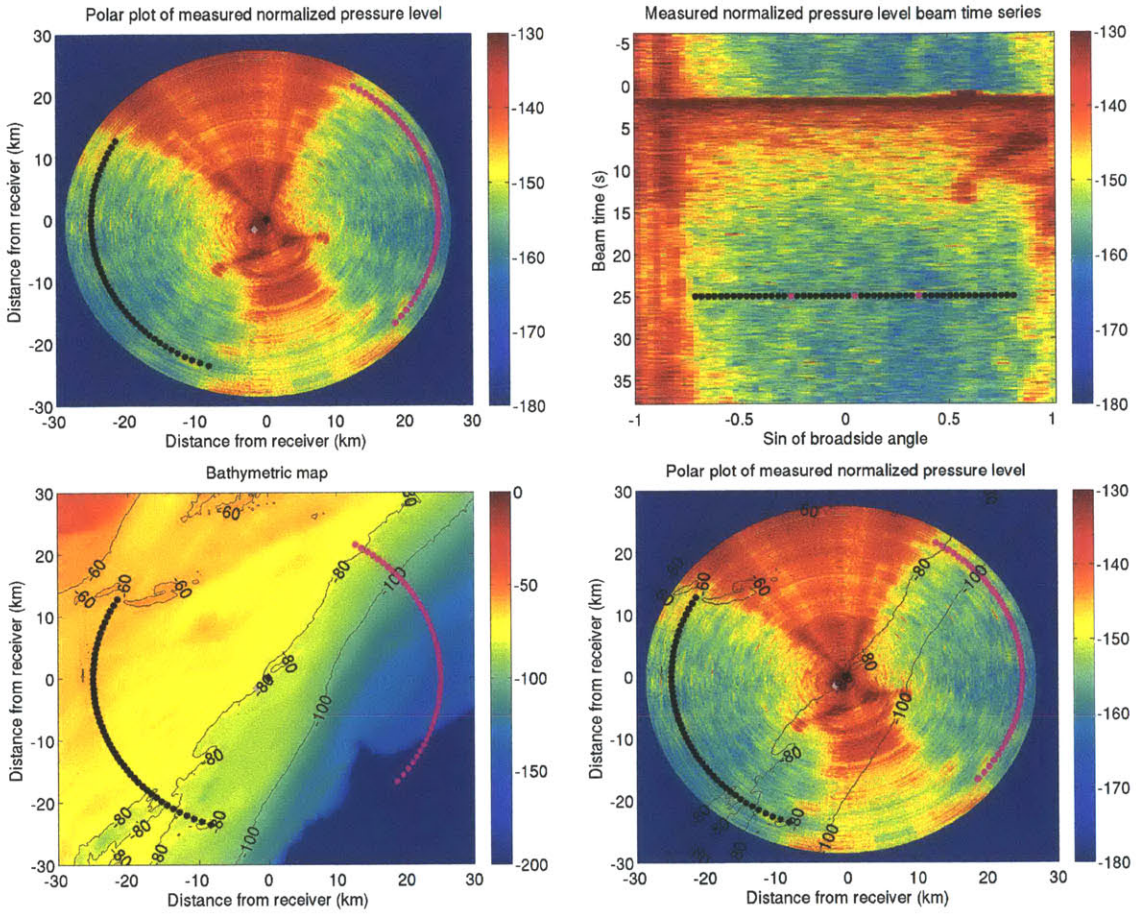

Figure C-2: New Jersey continental shelf: (top left) Polar plot of received normalized pressure level by OAWRS at 14:31 EDT, on 13 May 2003. The grey diamond indicates the source, located at 39.2312N, 72.8818W and operating at 390-440 Hz. The black diamond indicates the receiver, the coordinate origin, located at 39.2465N, 72.8626W, with heading 346°E. The black and magenta stars indicate the beams chosen for analysis, corresponding to the original and mirror beams, respectively. (top right) Received normalized pressure level as beam time series. The black stars indicate the beams chosen for analysis. The three magenta stars correspond to the beams analyzed in Figures C-3 and C-4. (bottom left) Bathymetric map of the region with depth contours at 60, 80 and 100m. The grey and white diamonds correspond to the source and receiver, respectively. The black and magenta stars indicate the beams chosen for analysis. (bottom right) Polar plot of received normalized pressure with overlain bathymetric contours.

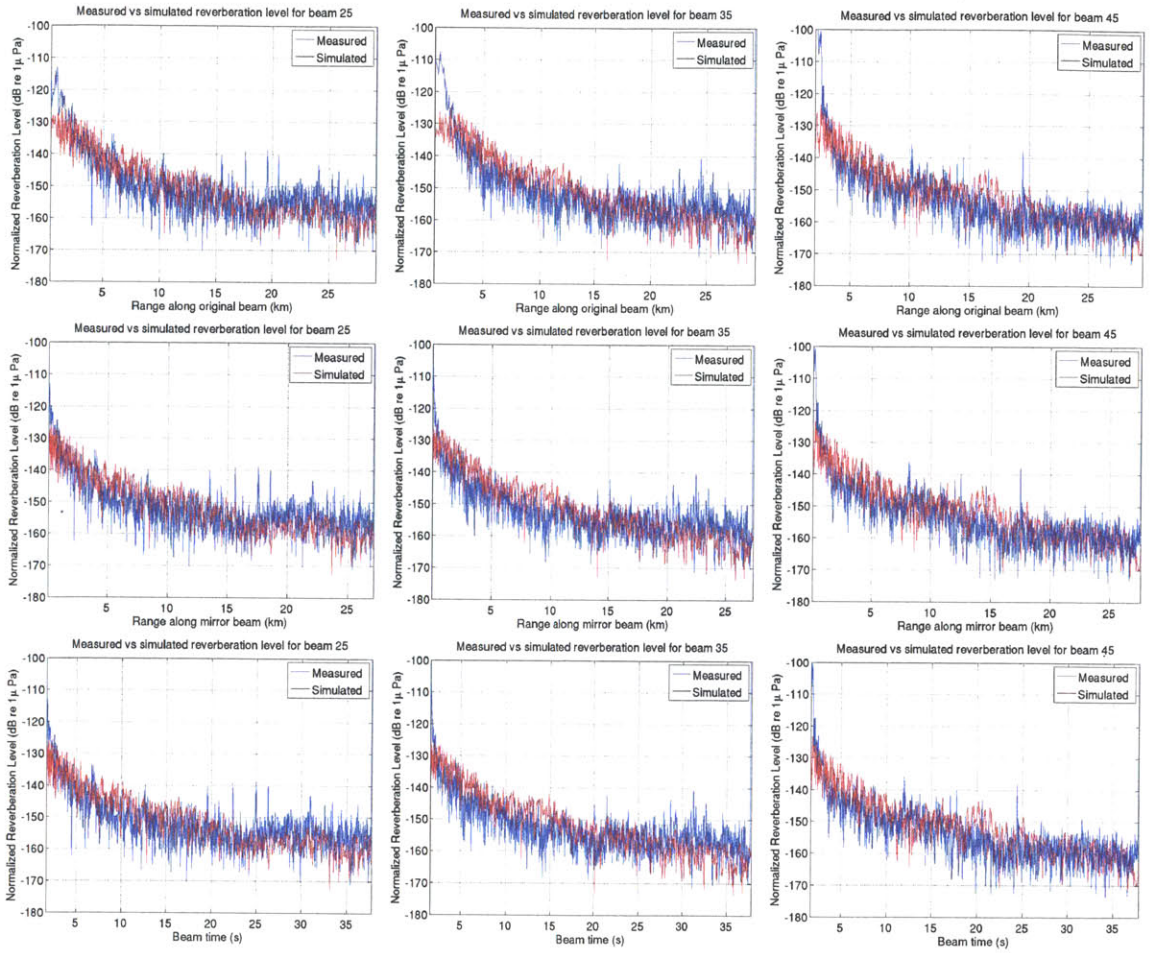

Figure C-3: Comparison of measured and simulated reverberation levels plotted against: beam time (top), range from the receiver along the original beam (middle), range from receiver along the mirror beam (bottom), for beams 30, 40 and 50, indicated by magenta stars in Figure C-2 (top right).

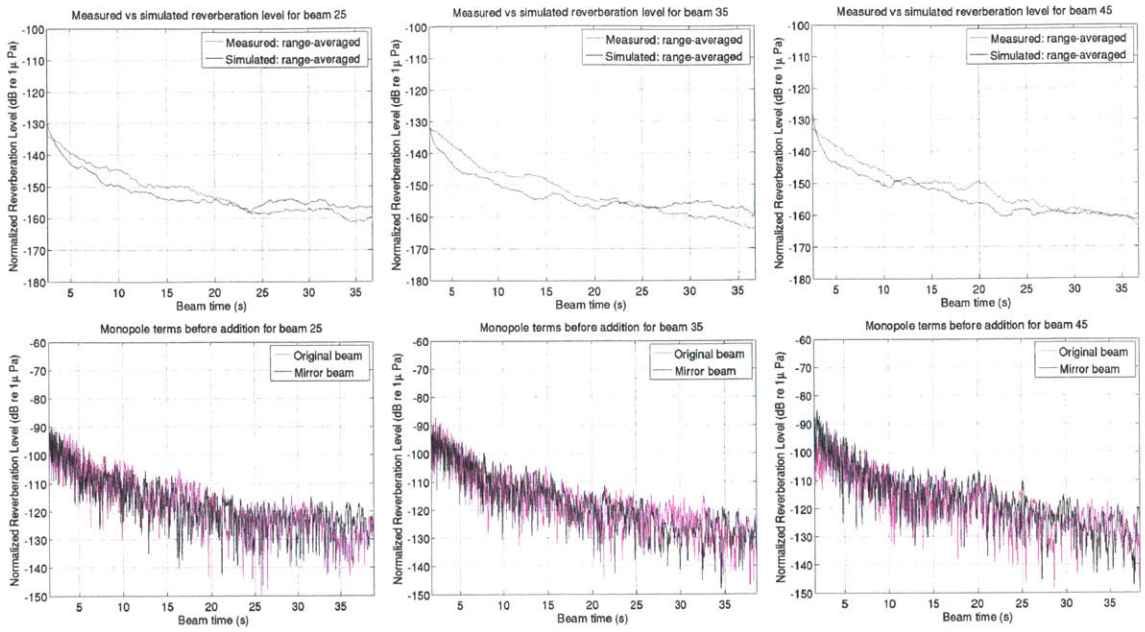

Figure C-4: For the same beams as in the previous figure C-3: comparison of measured and simulated reverberation time series after range/time averaging (top); comparison of the monopole term before adding the reverberation intensities for the original and mirror beams (bottom).

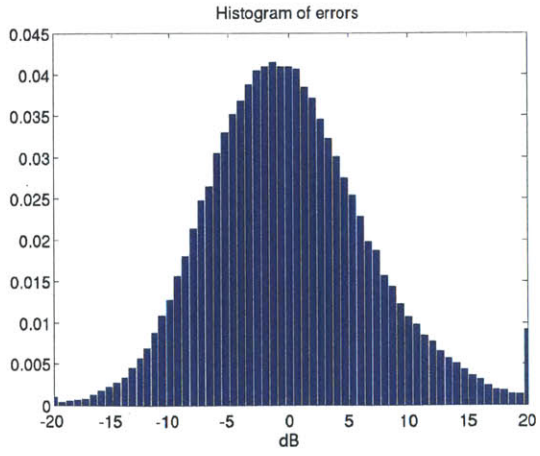

Figure C-5: Histogram of data-model differences for Figure C-6.

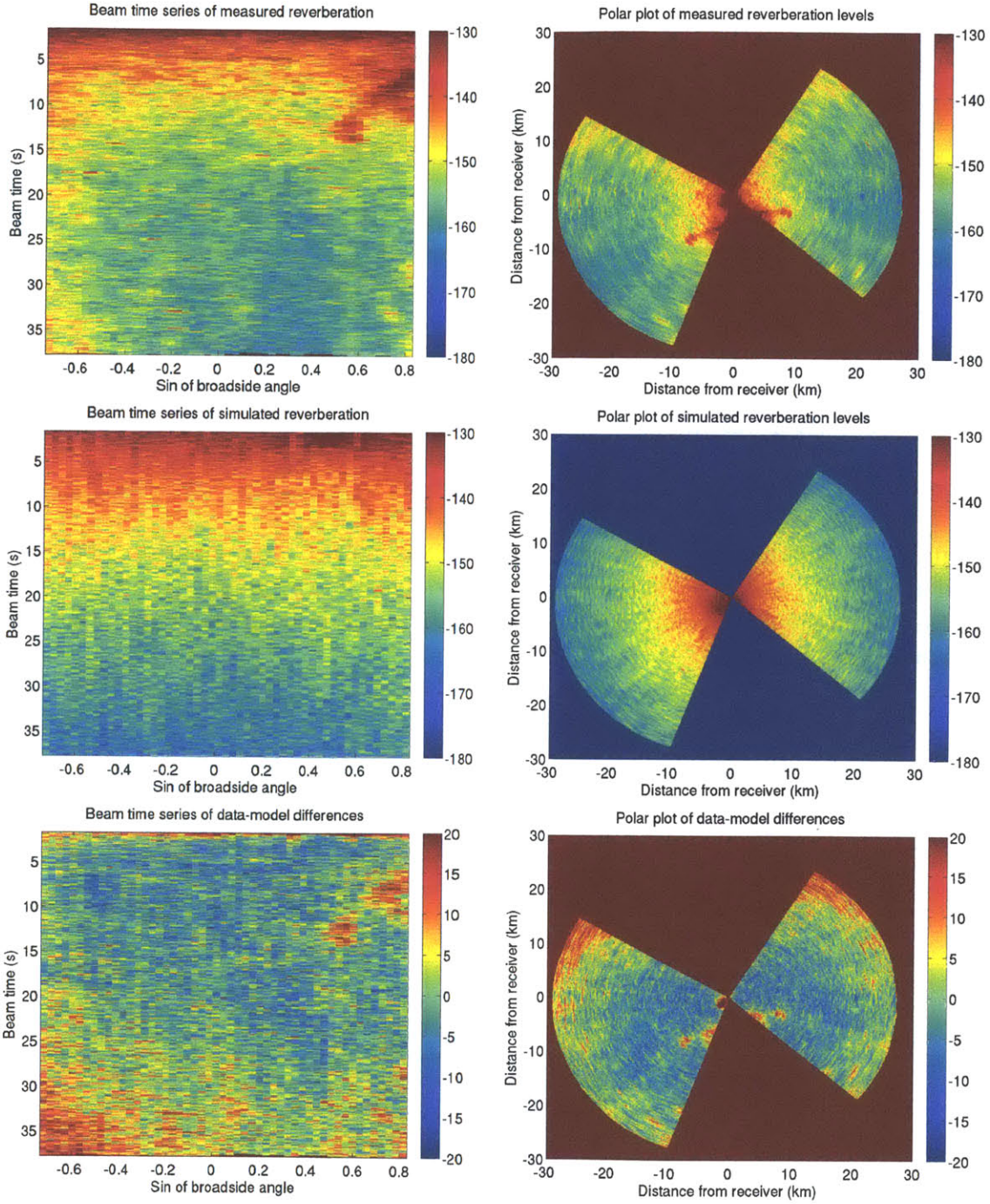

Figure C-6: Beam time (left) and polar (right) plots of measured reverberation level (top), simulated reverberation level (middle) and their difference (bottom).

C.2 New Jersey, 925 Hz

Implementation to New Jersey data, 925Hz, ping fora2003jd124t155725.

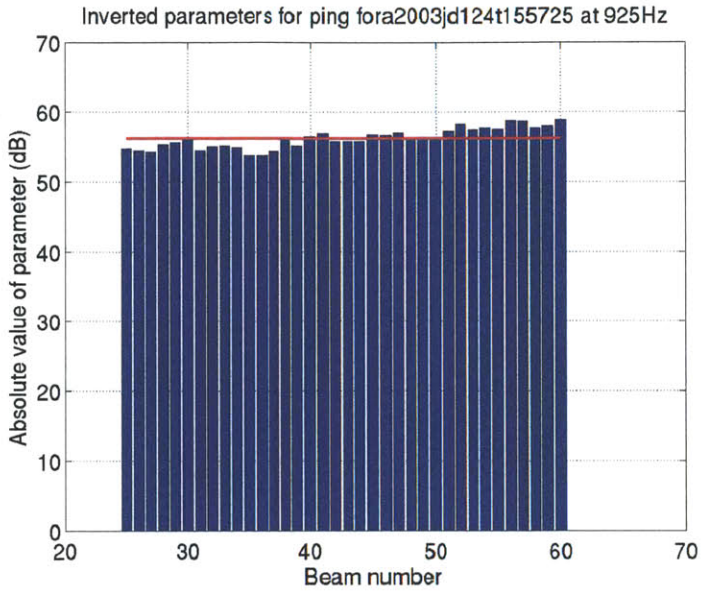

Figure C-7: Parameters obtained after fitting the model to the data for each beam, in log scale. The red horizontal line indicates the mean of the parameter values (log scale). Only beams corresponding to relatively flat or downward sloping bathymetry were included in the analysis. Endfire beams as well as beams contaminated by clutter were also excluded. The second half of the data and model time series were chosen for calibration, as the model fails to predict well the data for small ranges.

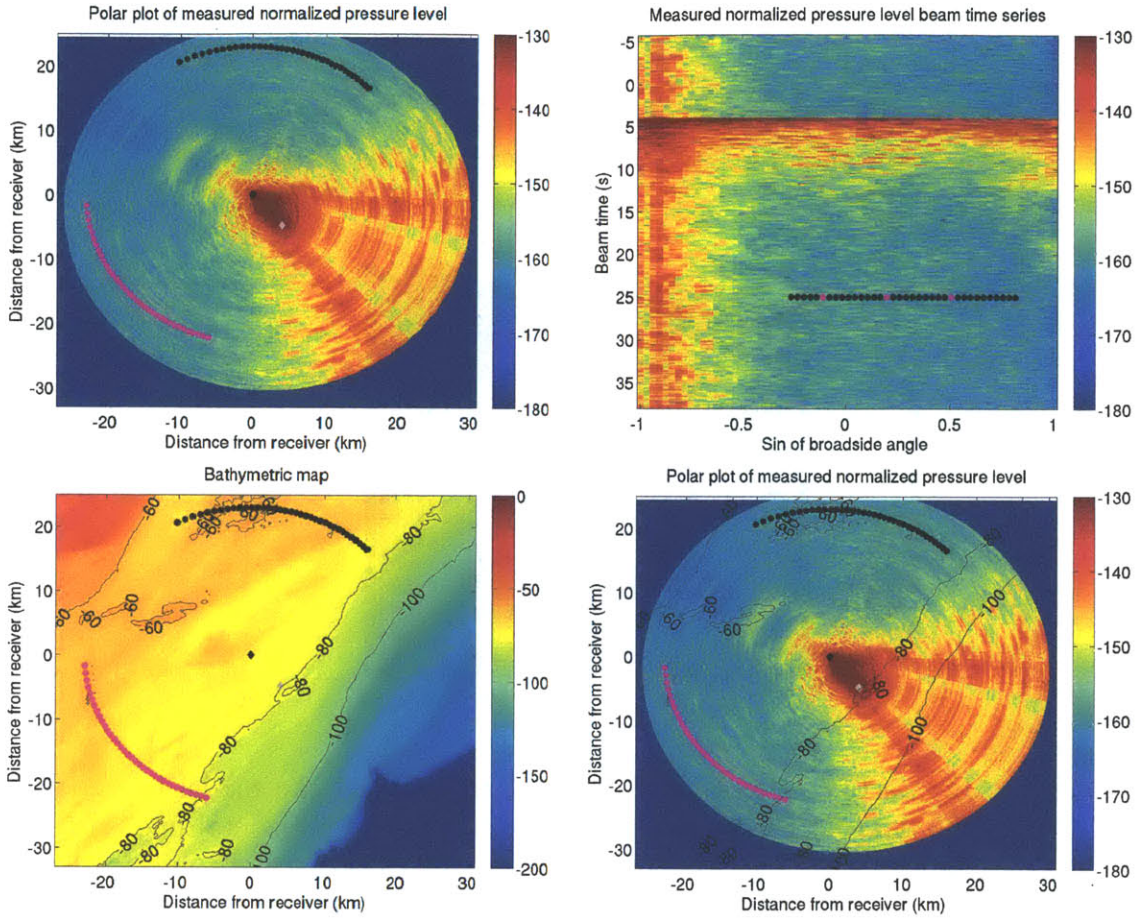

Figure C-8: New Jersey continental shelf: (top left) Polar plot of received normalized pressure level by OAWRS at 15:57 EDT, on 4 May 2003. The grey diamond indicates the source, located at 39.2694N, 72.8630W and operating at 875-975 Hz. The black diamond indicates the receiver, the coordinate origin, located at 39.3108N, 72.9116W, with heading 120°E. The black and magenta stars indicate the beams chosen for analysis, corresponding to the original and mirror beams, respectively. (top right) Received normalized pressure level as beam time series. The black stars indicate the beams chosen for analysis. The three magenta stars correspond to the beams analyzed in Figures C-9 and C-10. (bottom left) Bathymetric map of the region with depth contours at 60, 80 and 100m. The grey and white diamonds correspond to the source and receiver, respectively. The black and magenta stars indicate the beams chosen for analysis. (bottom right) Polar plot of received normalized pressure with overlain bathymetric contours.

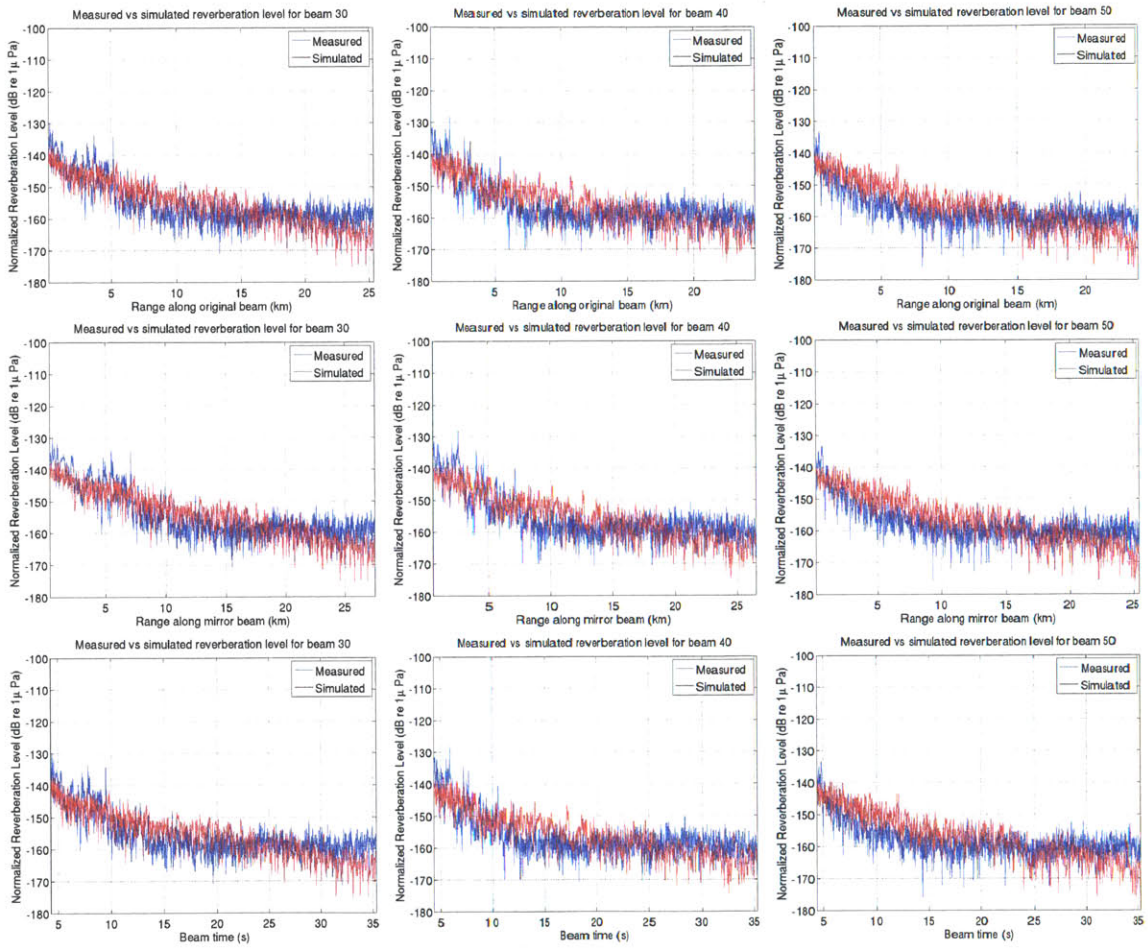

Figure C-9: Comparison of measured and simulated reverberation levels plotted against: beam time (top), range from the receiver along the original beam (middle), range from receiver along the mirror beam (bottom), for beams 30, 40 and 50, indicated by magenta stars in Figure C-8 (top right).

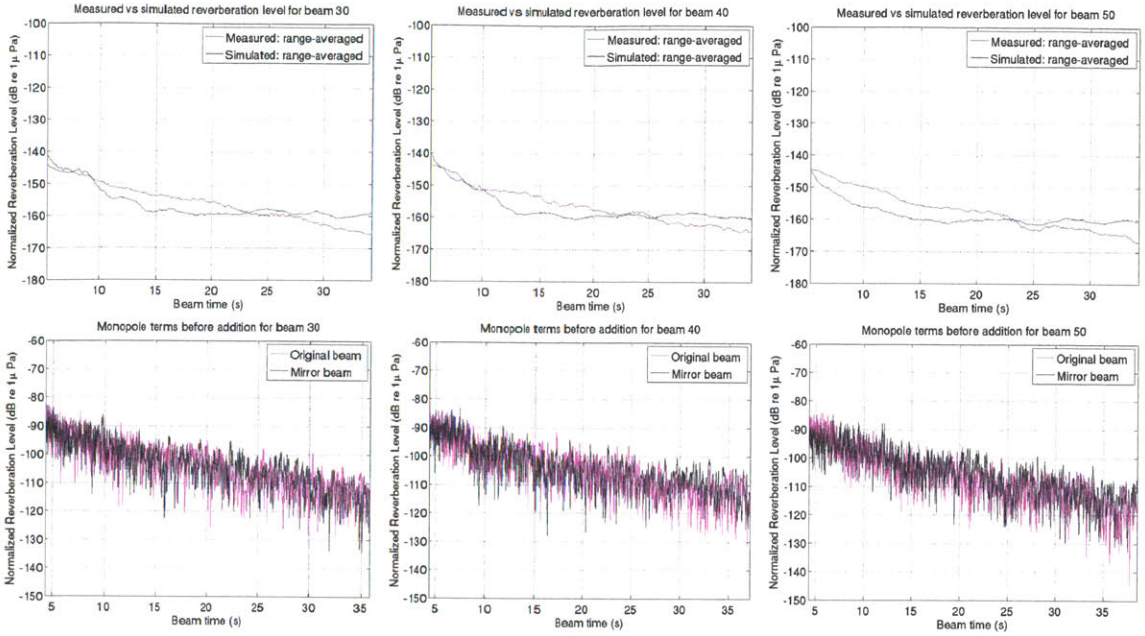

Figure C-10: For the same beams as in the previous figure C-9: comparison of measured and simulated reverberation time series after range/time averaging (top); comparison of the monopole term before adding the reverberation intensities for the original and mirror beams (bottom).

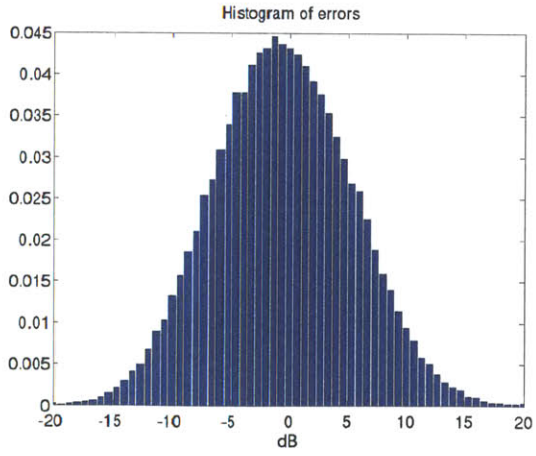

Figure C-11: Histogram of data-model differences for Figure C-12.

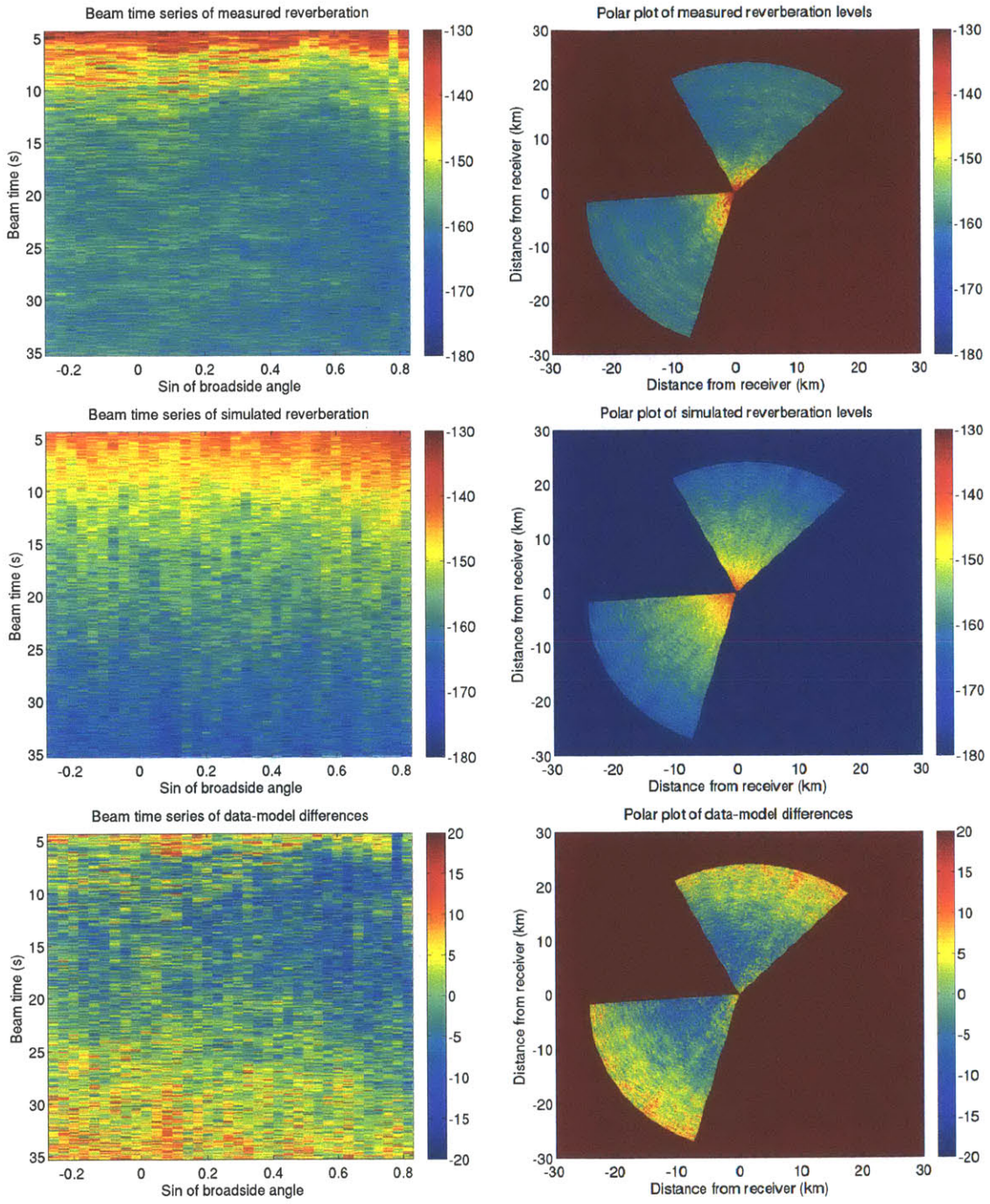

Figure C-12: Beam time (left) and polar (right) plots of measured reverberation level (top), simulated reverberation level (middle) and their difference (bottom).

C.3 New Jersey, 1325 Hz

Implementation to New Jersey data, 1325Hz, ping fora2003jd124t155135.

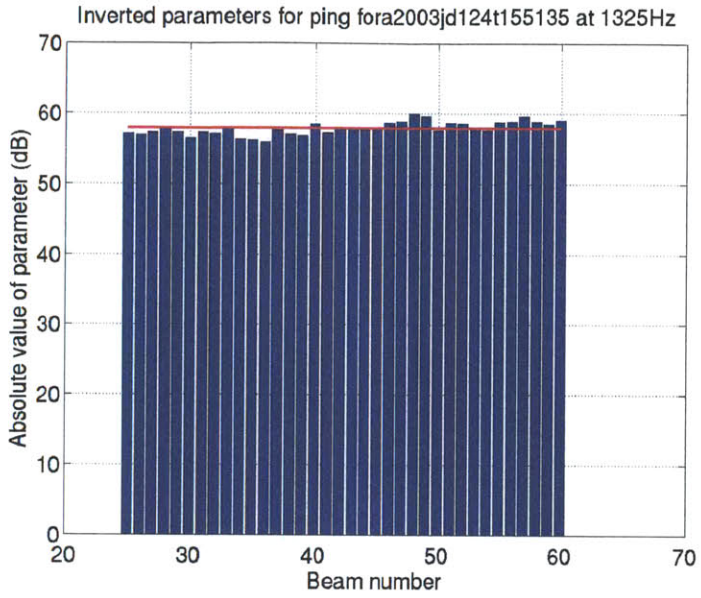

Figure C-13: Parameters obtained after fitting the model to the data for each beam, in log scale. The red horizontal line indicates the mean of the parameter values (log scale). Only beams corresponding to relatively flat or downward sloping bathymetry were included in the analysis. Endfire beams as well as beams contaminated by clutter were also excluded. The second half of the data and model time series were chosen for calibration, as the model fails to predict well the data for small ranges.

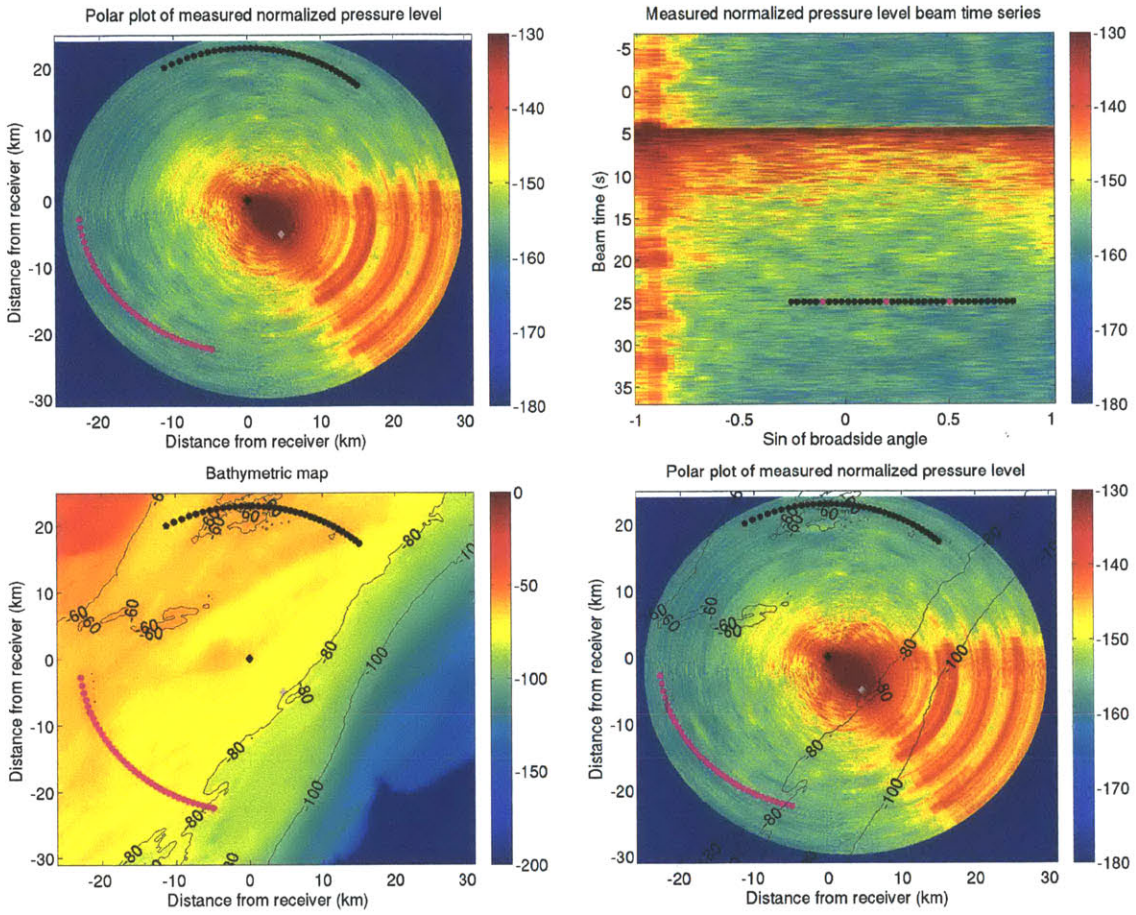

Figure C-14: New Jersey continental shelf: (top left) Polar plot of received normalized pressure level by OAWRS at 15:51 EDT, on 4 May 2003. The grey diamond indicates the source, located at 39.2694N, 72.8630W and operating at 1250-1400 Hz. The black diamond indicates the receiver, the coordinate origin, located at 39.3140N, 72.9185W, with heading 117°E. The black and magenta stars indicate the beams chosen for analysis, corresponding to the original and mirror beams, respectively. (top right) Received normalized pressure level as beam time series. The black stars indicate the beams chosen for analysis. The three magenta stars correspond to the beams analyzed in Figures C-15 and C-16. (bottom left) Bathymetric map of the region with depth contours at 60, 80 and 100m. The grey and white diamonds correspond to the source and receiver, respectively. The black and magenta stars indicate the beams chosen for analysis. (bottom right) Polar plot of received normalized pressure with overlain bathymetric contours.

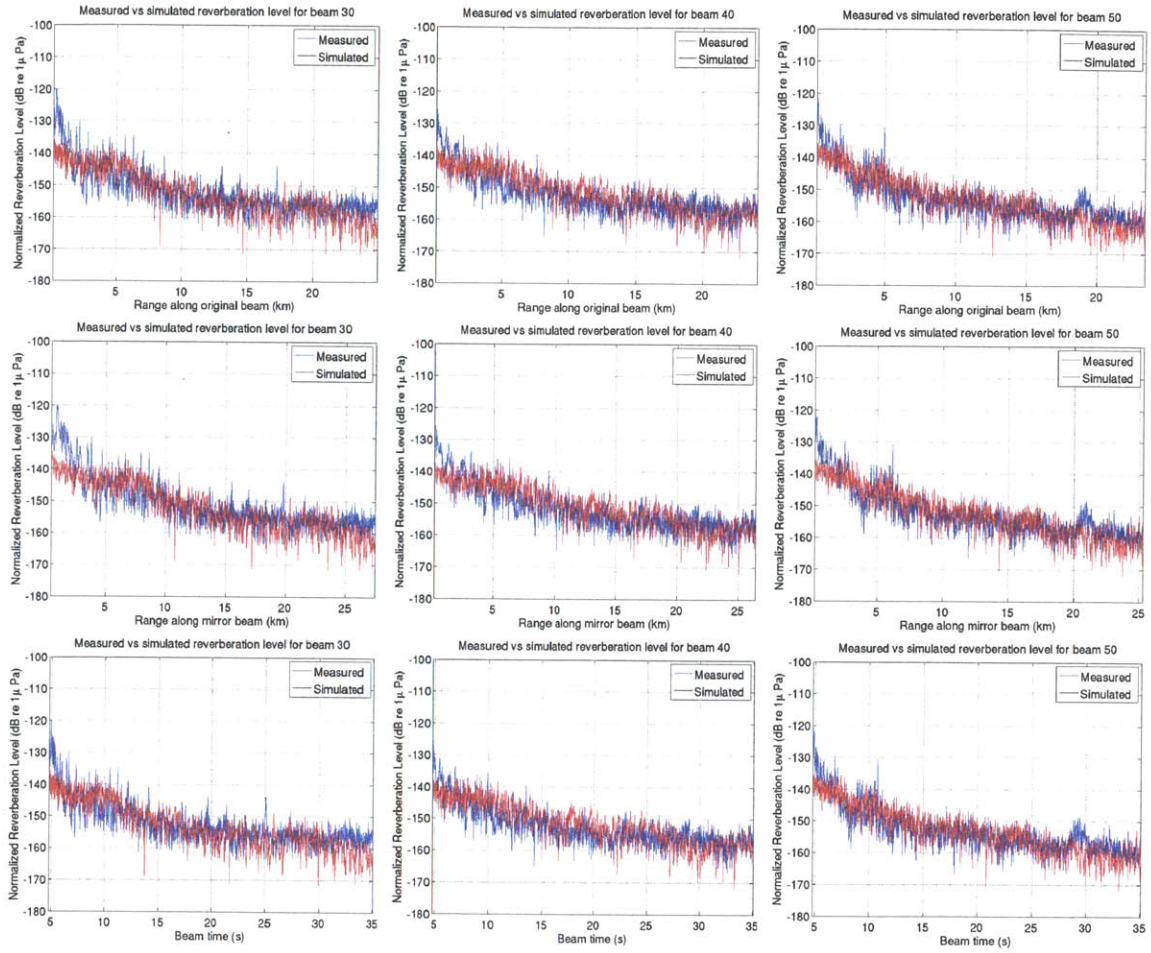

Figure C-15: Comparison of measured and simulated reverberation levels plotted against: beam time (top), range from the receiver along the original beam (middle), range from receiver along the mirror beam (bottom), for beams 30, 40 and 50, indicated by magenta stars in Figure C-14 (top right).

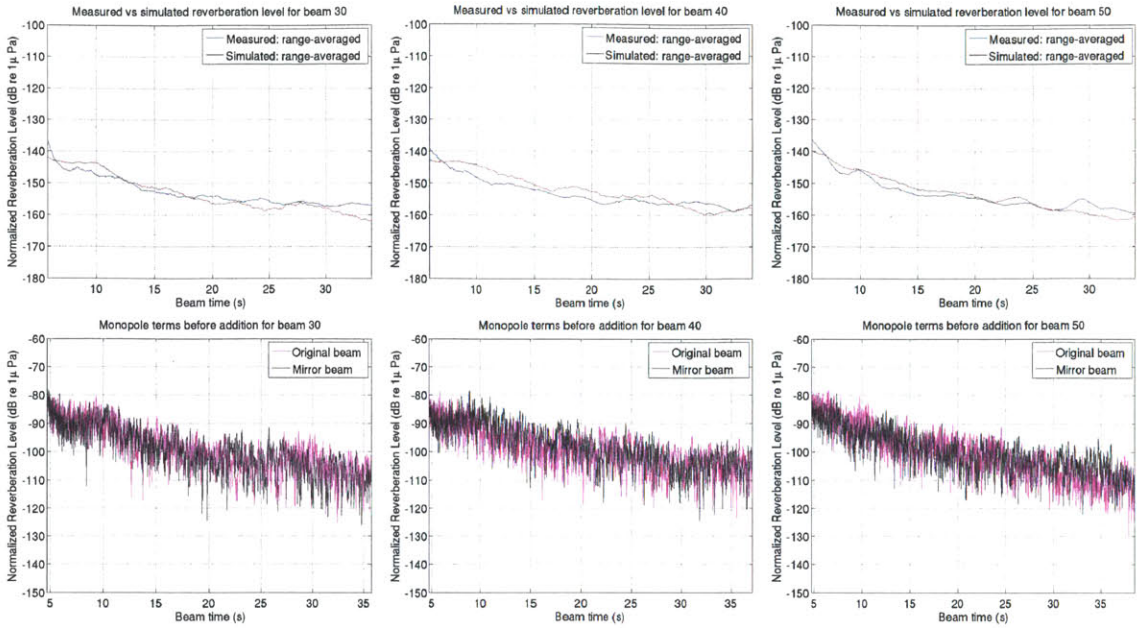

Figure C-16: For the same beams as in the previous figure C-15: comparison of measured and simulated reverberation time series after range/time averaging (top); comparison of the monopole term before adding the reverberation intensities for the original and mirror beams (bottom).

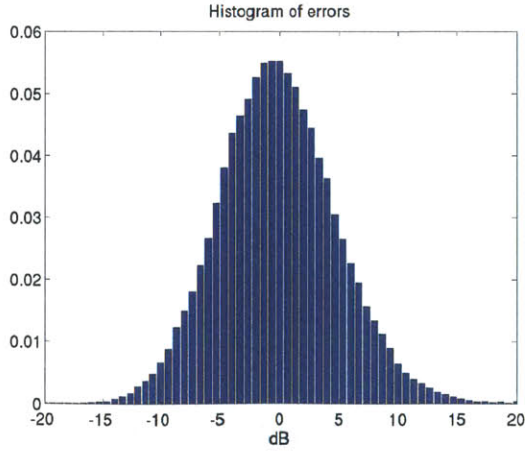

Figure C-17: Histogram of data-model differences for Figure C-18.

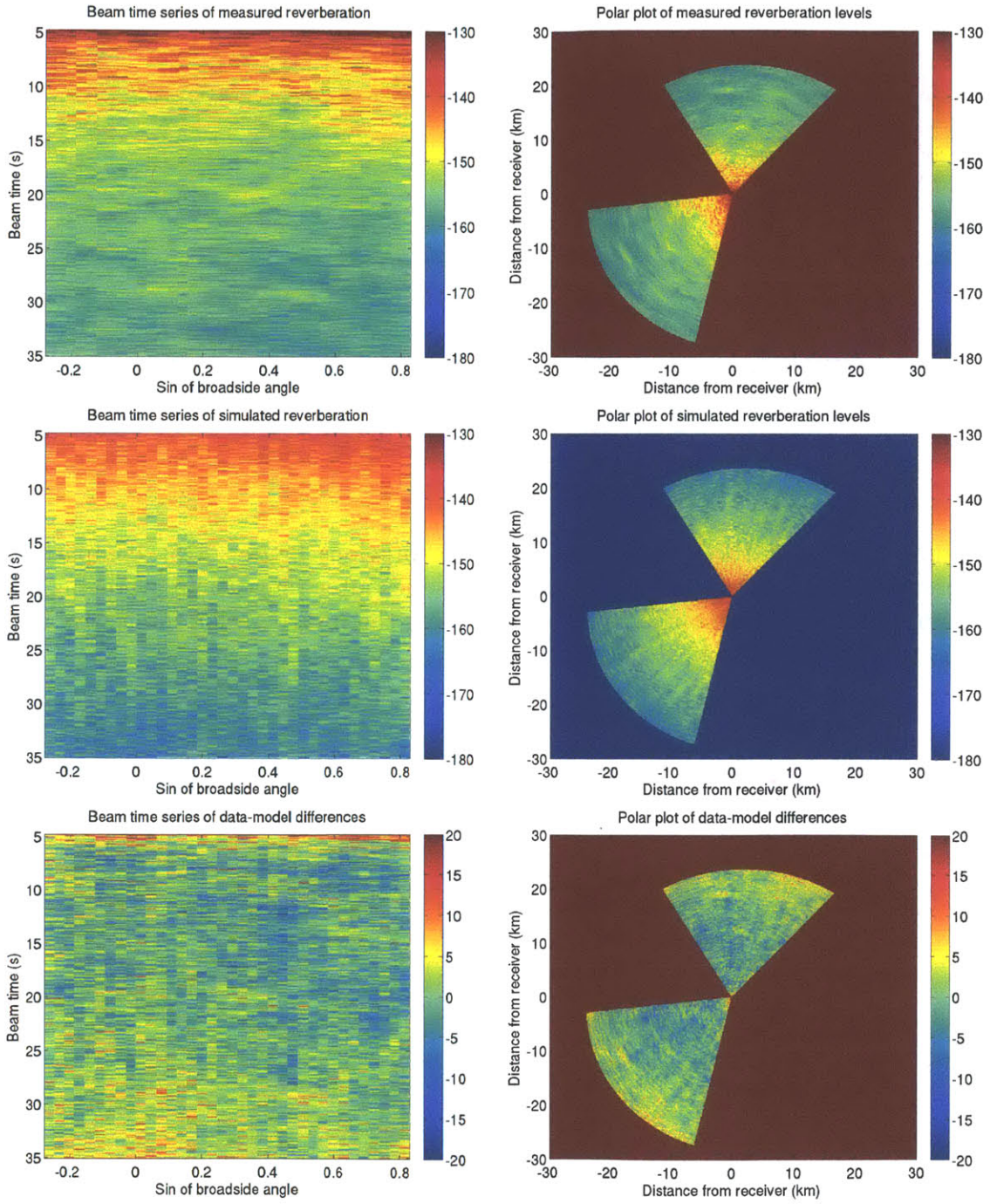

Figure C-18: Beam time (left) and polar (right) plots of measured reverberation level (top), simulated reverberation level (middle) and their difference (bottom).

C.4 Georges Bank, 415 Hz

Implementation to Georges Bank data, 415Hz, ping fora2006jd269t165140.

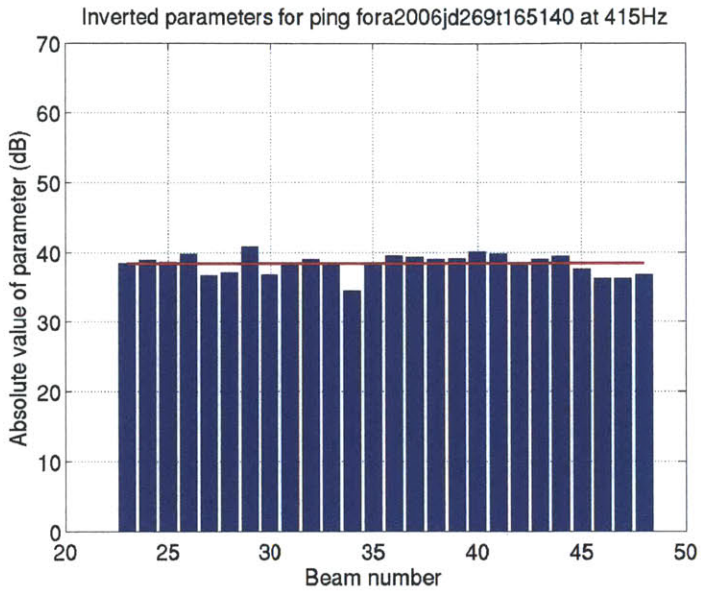

Figure C-19: Parameters obtained after fitting the model to the data for each beam, in log scale. The red horizontal line indicates the mean of the parameter values (log scale). Only beams corresponding to relatively flat or downward sloping bathymetry were included in the analysis. Endfire beams as well as beams contaminated by clutter were also excluded. The second half of the data and model time series were chosen for calibration, as the model fails to predict well the data for small ranges.

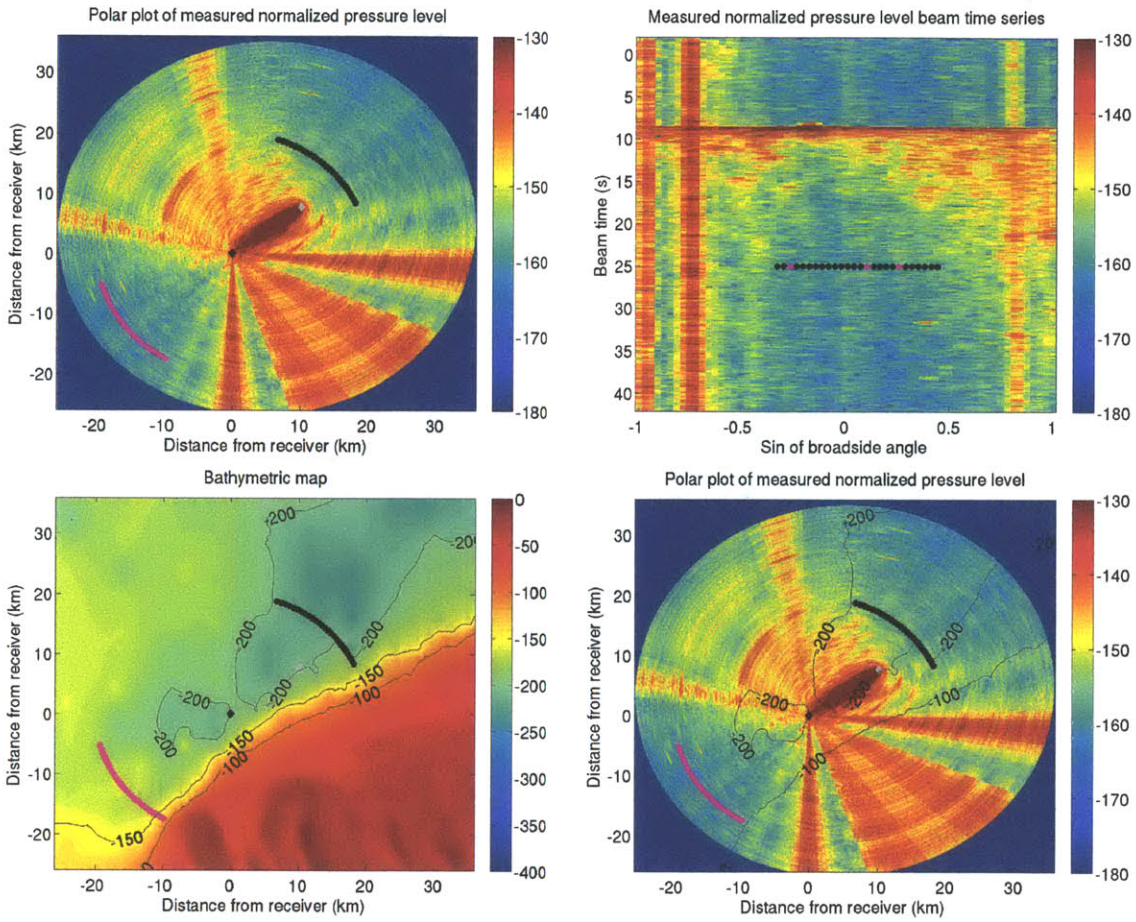

Figure C-20: Northern flank of Georges Bank in the Gulf of Maine: (top left) Polar plot of received normalized pressure level by OAWRS at 11:58 EDT, on 26 September 2006. The grey diamond indicates the source, located at 41.8901N, 68.2134W and operating at 390-440 Hz. The black diamond indicates the receiver, the coordinate origin, located at 41.8212N, 68.3368W, with heading 137°E. The black and magenta stars indicate the beams chosen for analysis, corresponding to the original and mirror beams, respectively. (top right) Received normalized pressure level as beam time series. The black stars indicate the beams chosen for analysis. The three magenta stars correspond to the beams analyzed in Figures C-21 and C-22. (bottom left) Bathymetric map of the region with depth contours at 100, 150 and 200m. The grey and white diamonds correspond to the source and receiver, respectively. The black and magenta stars indicate the beams chosen for analysis. (bottom right) Polar plot of received normalized pressure with overlain bathymetric contours.

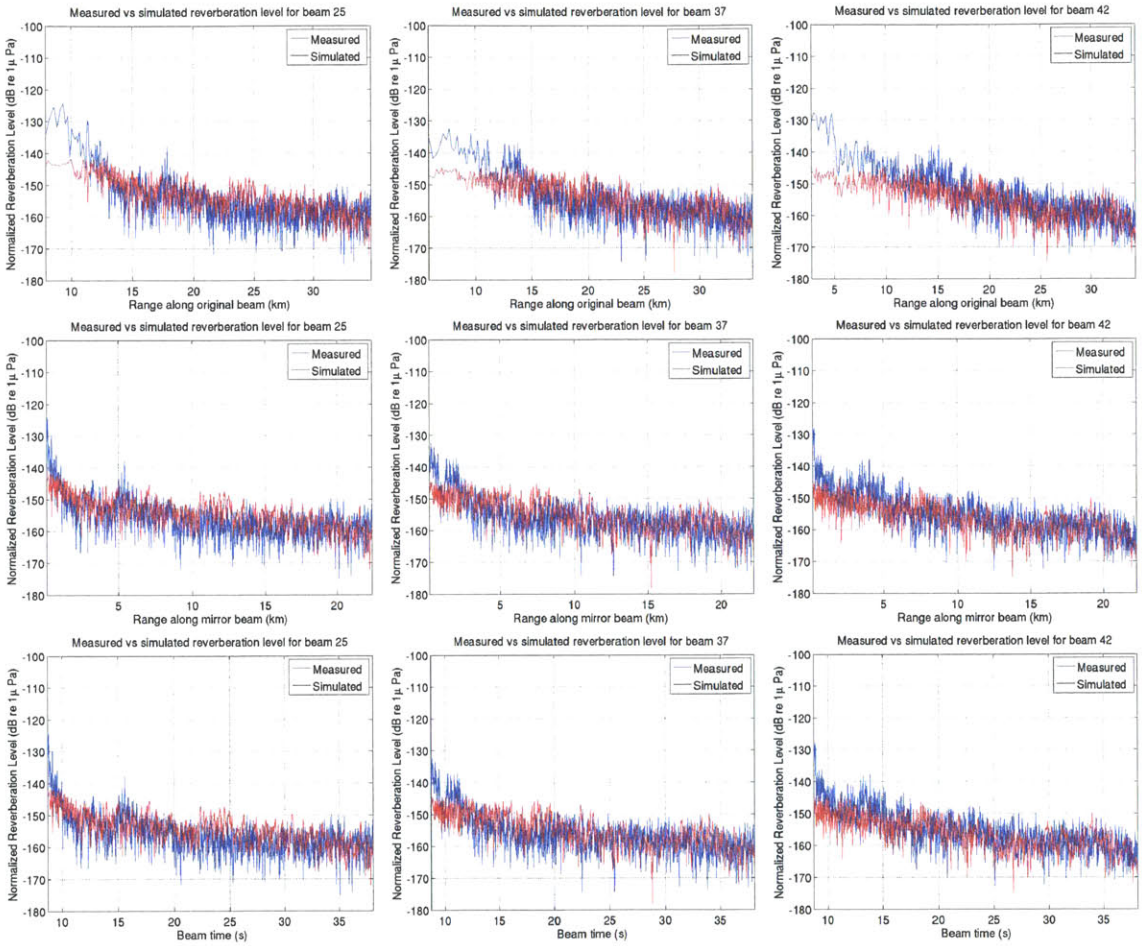

Figure C-21: Comparison of measured and simulated reverberation levels plotted against: beam time (top), range from the receiver along the original beam (middle), range from receiver along the mirror beam (bottom), for beams 25, 37 and 42 indicated by magenta stars in Figure C-20 (top right).

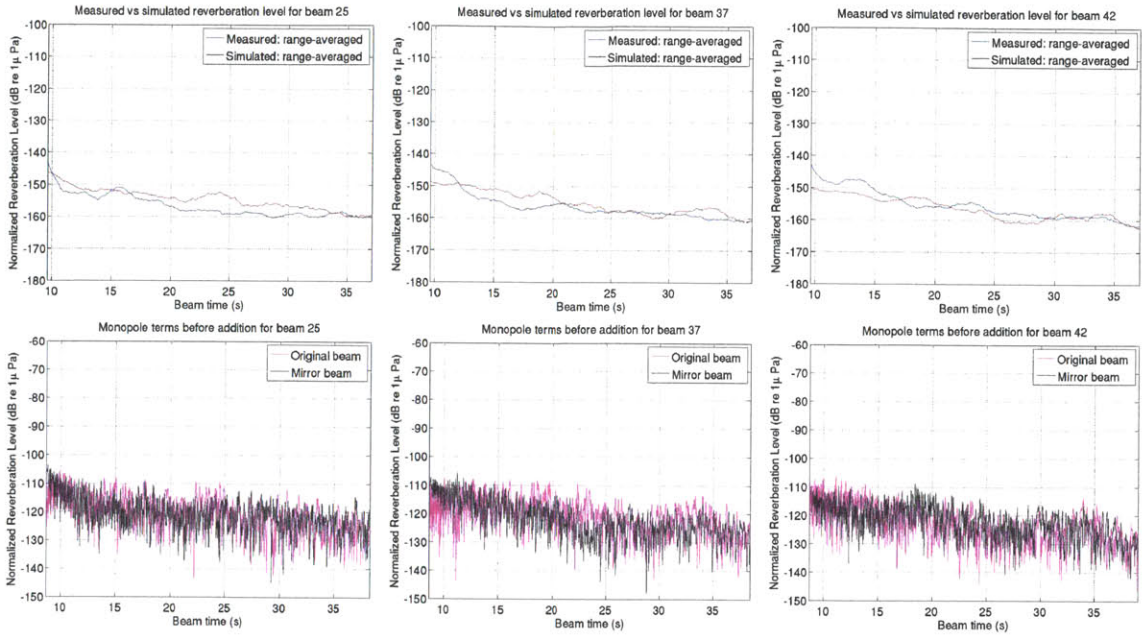

Figure C-22: For the same beams as in the previous figure C-21: comparison of measured and simulated reverberation time series after range/time averaging (top); comparison of the monopole term before adding the reverberation intensities for the original and mirror beams (bottom).

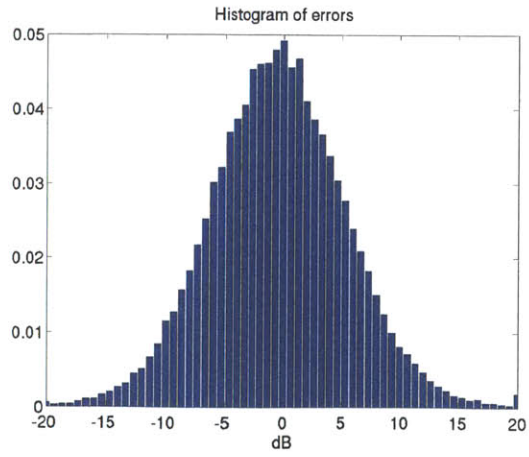

Figure C-23: Histogram of data-model differences for Figure C-24.

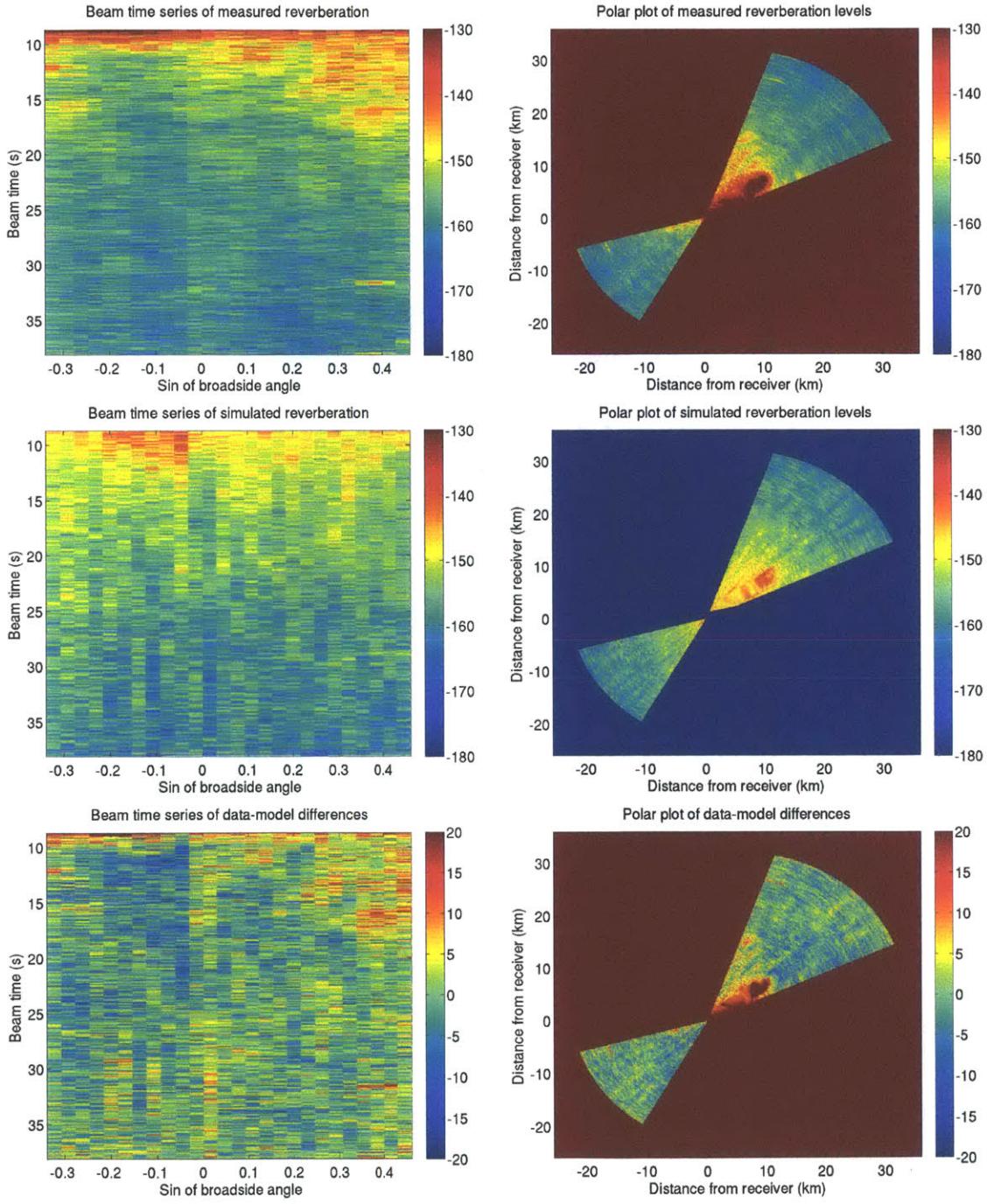

Figure C-24: Beam time (left) and polar (right) plots of measured reverberation level (top), simulated reverberation level (middle) and their difference (bottom).

C.5 Georges Bank, 950 Hz

Implementation to Georges Bank data, 950Hz, ping fora2006jd278t025345.

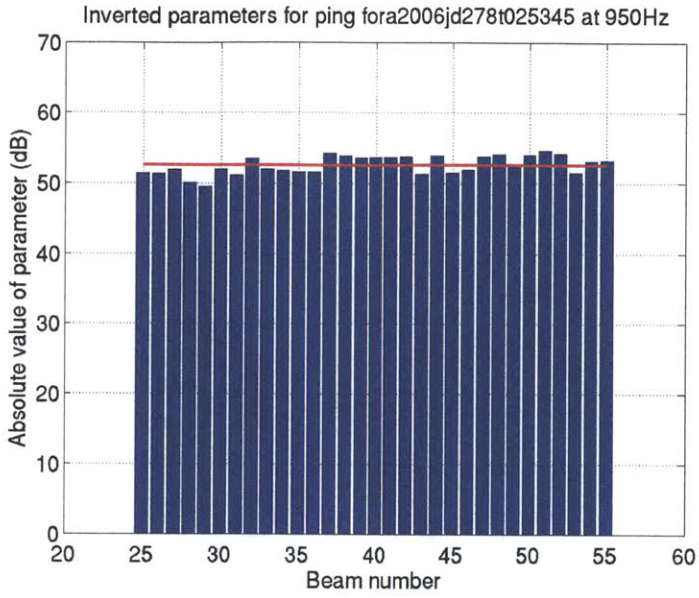

Figure C-25: Parameters obtained after fitting the model to the data for each beam, in log scale. The red horizontal line indicates the mean of the parameter values (log scale). Only beams corresponding to relatively flat or downward sloping bathymetry were included in the analysis. Endfire beams as well as beams contaminated by clutter were also excluded. The second half of the data and model time series were chosen for calibration, as the model fails to predict well the data for small ranges.

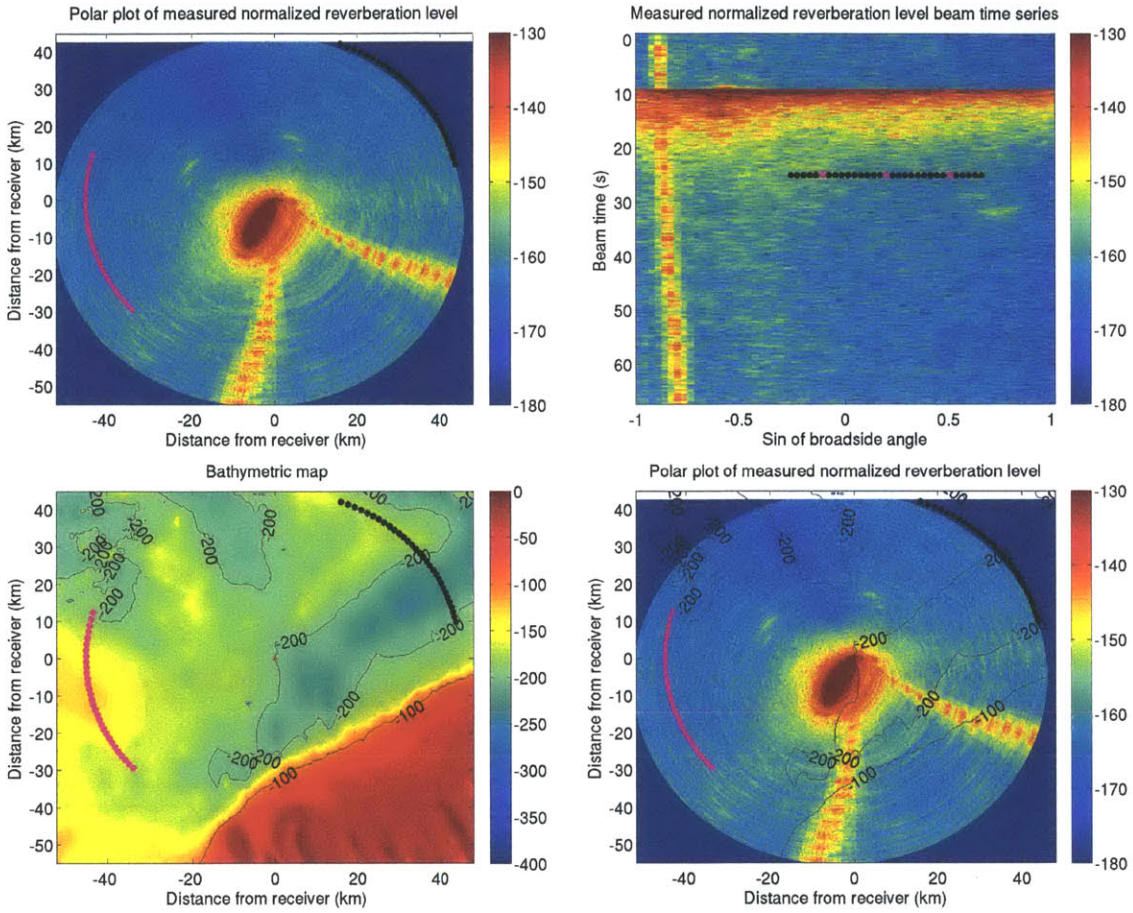

Figure C-26: Northern flank of Georges Bank in the Gulf of Maine: (top left) Polar plot of received normalized pressure level by OAWRS at 22:53 EDT, on 4 October 2006. The grey diamond indicates the source, located at 41.9696N, 68.3507W and operating at 925-975 Hz. The black diamond indicates the receiver, the coordinate origin, located at 42.0776N, 68.2707W, with heading 153°E. The black and magenta stars indicate the beams chosen for analysis, corresponding to the original and mirror beams, respectively. (top right) Received normalized pressure level as beam time series. The black stars indicate the beams chosen for analysis. The three magenta stars correspond to the beams analyzed in Figures C-27 and C-28. (bottom left) Bathymetric map of the region with depth contours at 100, 200 and 300m. The grey and white diamonds correspond to the source and receiver, respectively. The black and magenta stars indicate the beams chosen for analysis. (bottom right) Polar plot of received normalized pressure with overlain bathymetric contours.

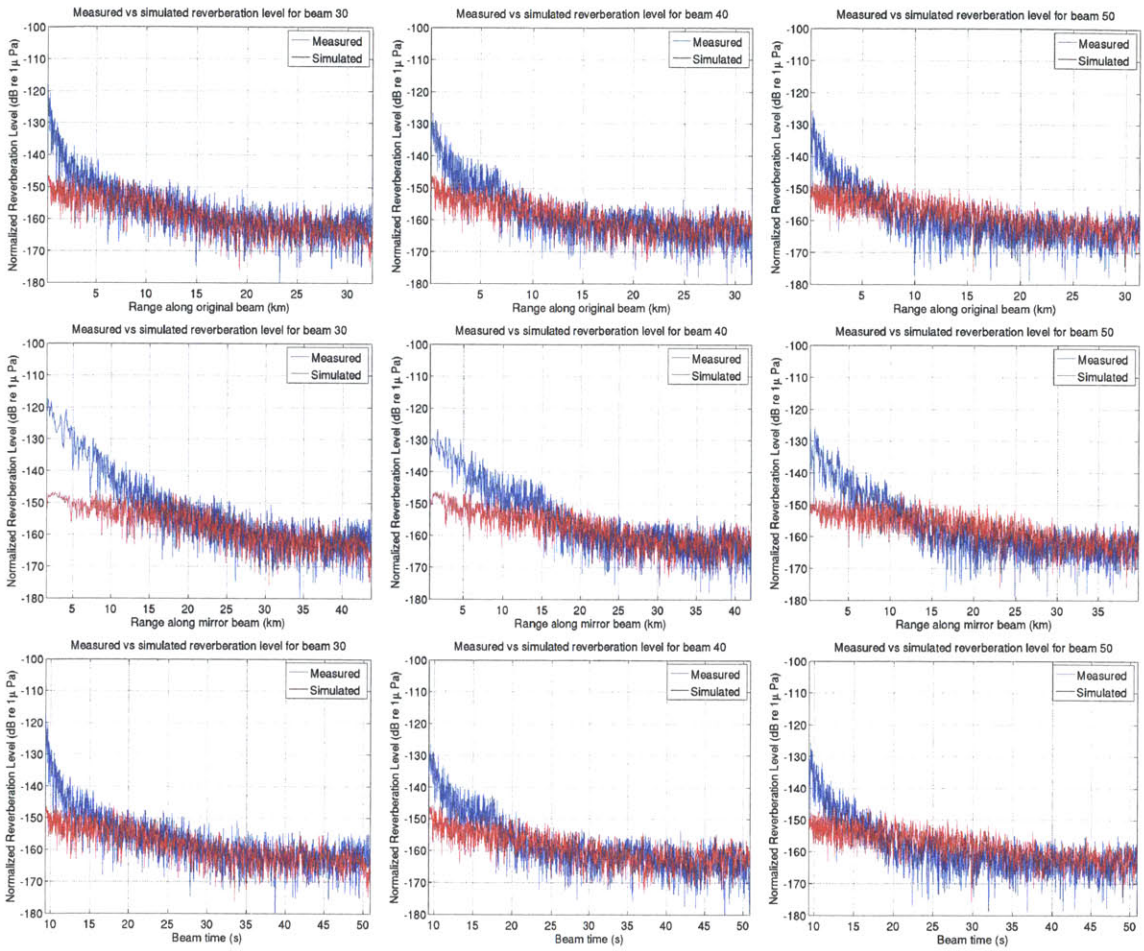

Figure C-27: Comparison of measured and simulated reverberation levels plotted against: beam time (top), range from the receiver along the original beam (middle), range from receiver along the mirror beam (bottom), for beams 35, 45 and 50, indicated by magenta stars in Figure C-26 (top right).

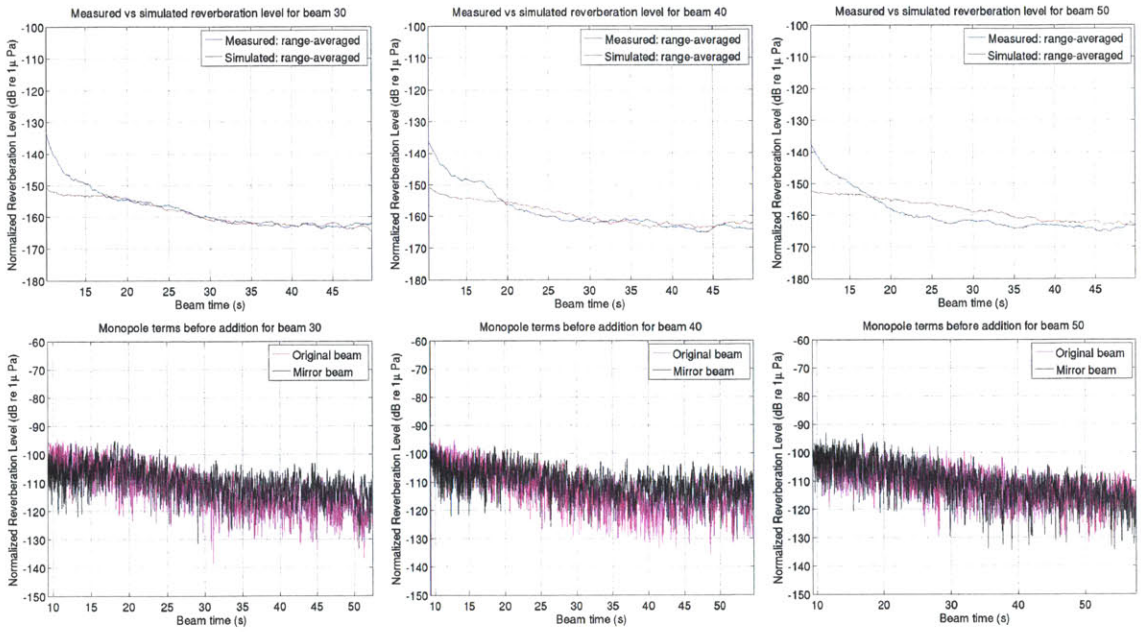

Figure C-28: For the same beams as in the previous figure C-27: comparison of measured and simulated reverberation time series after range/time averaging (top); comparison of the monopole term before adding the reverberation intensities for the original and mirror beams (bottom).

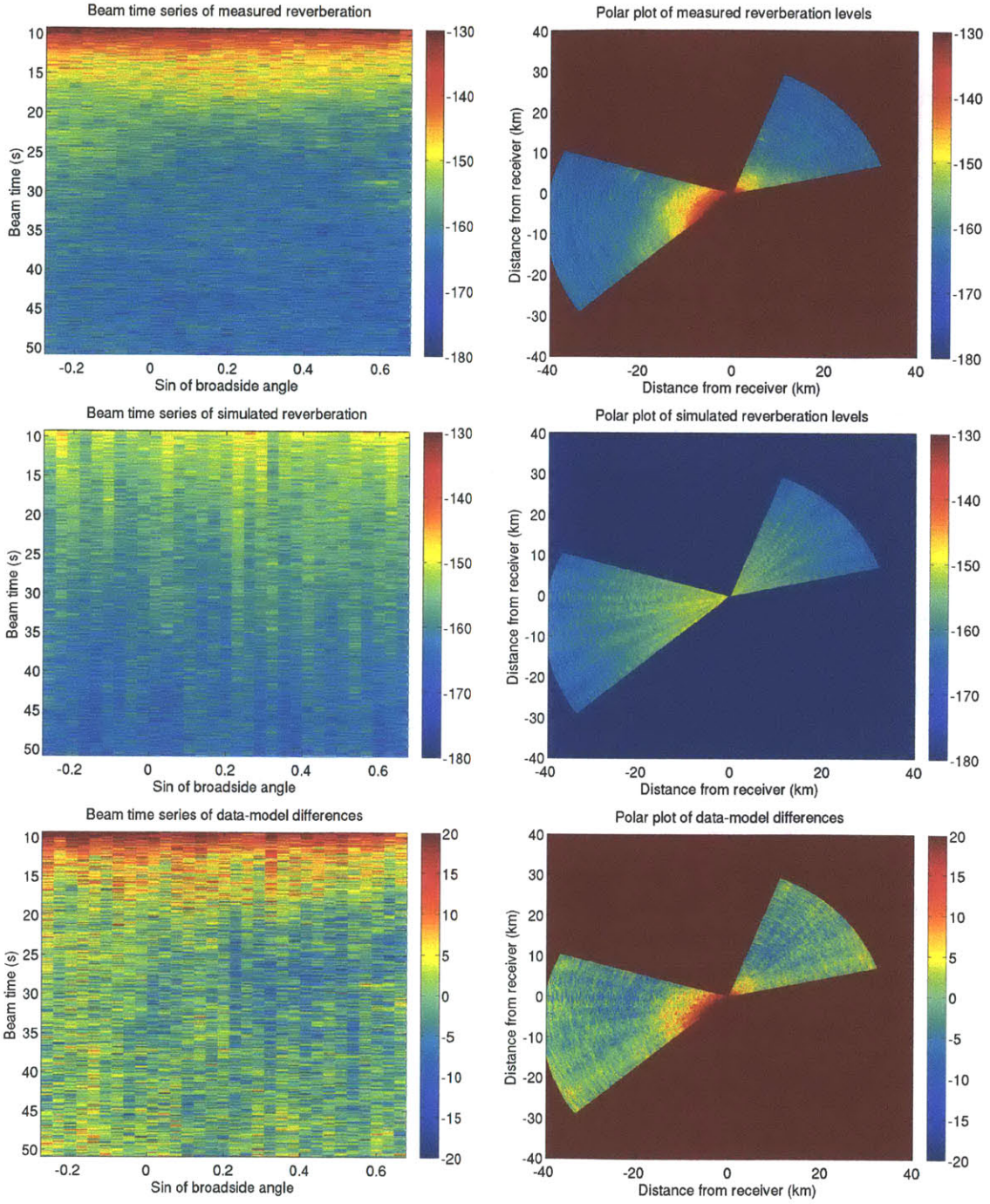

Figure C-29: Beam time (left) and polar (right) plots of measured reverberation level (top), simulated reverberation level (middle) and their difference (bottom).

C.6 Georges Bank, 1125 Hz

Implementation to Georges Bank data, 1125Hz, ping fora2006jd276t223615.

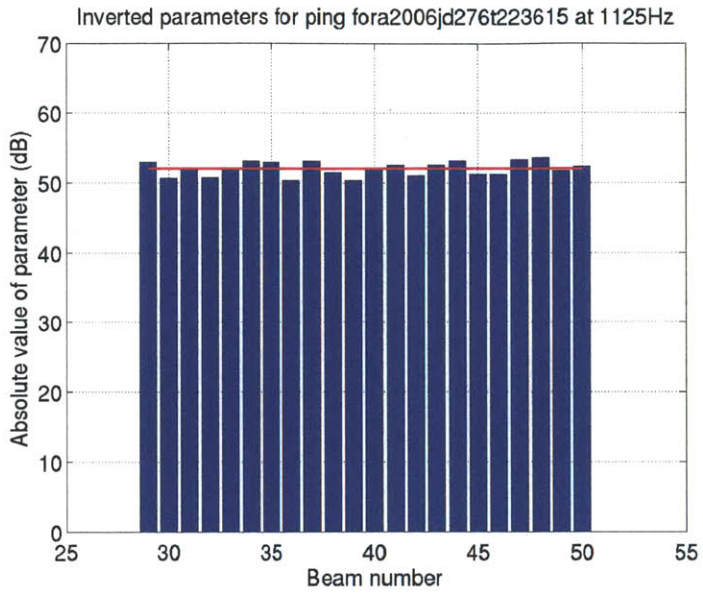

Figure C-30: Parameters obtained after fitting the model to the data for each beam, in log scale. The red horizontal line indicates the mean of the parameter values (log scale). Only beams corresponding to relatively flat or downward sloping bathymetry were included in the analysis. Endfire beams as well as beams contaminated by clutter were also excluded. The second half of the data and model time series were chosen for calibration, as the model fails to predict well the data for small ranges.

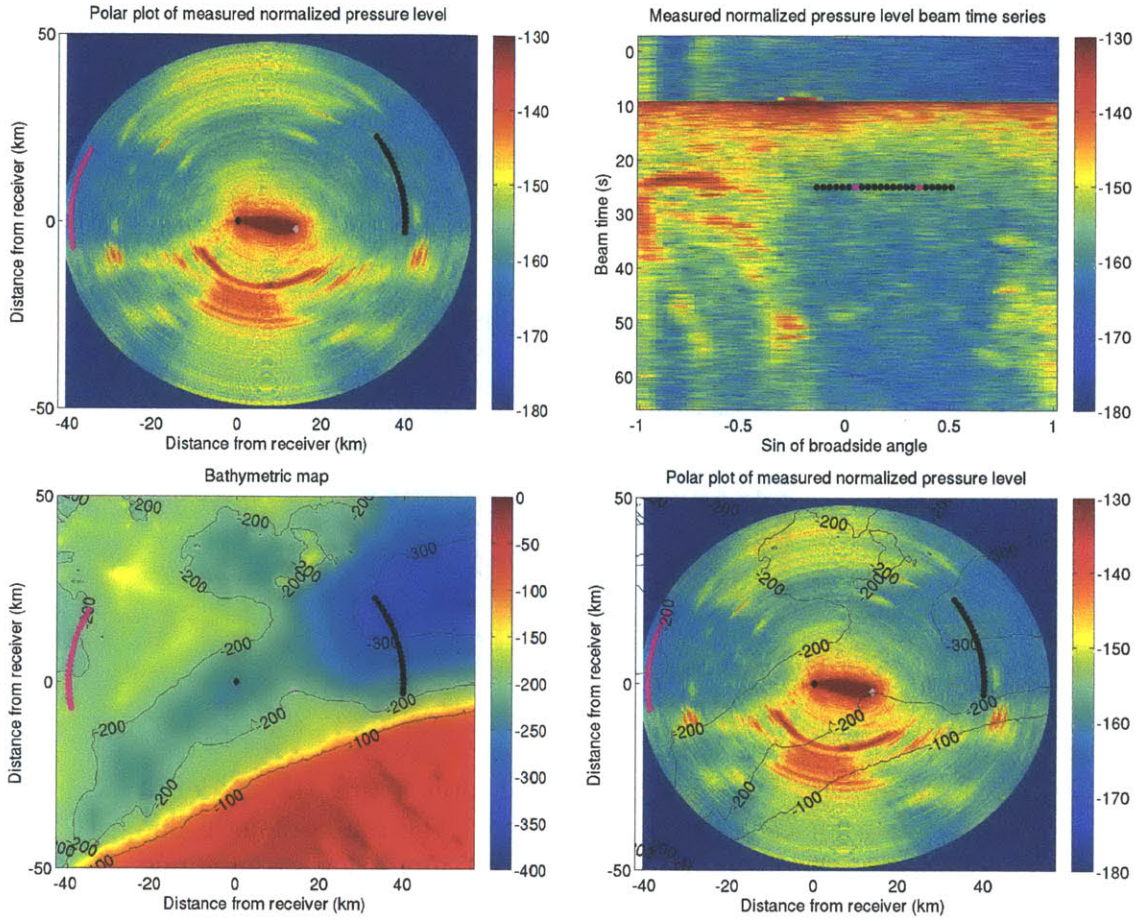

Figure C-31: Northern flank of Georges Bank in the Gulf of Maine: (top left) Polar plot of received normalized pressure level by OAWRS at 18:36 EDT, on 3 October 2006. The grey diamond indicates the source, located at 42.2088N, 67.6892W and operating at 1100-1150 Hz. The black diamond indicates the receiver, the coordinate origin, located at 42.2305N, 67.8553W, with heading 177°E. The black and magenta stars indicate the beams chosen for analysis, corresponding to the original and mirror beams, respectively. (top right) Received normalized pressure level as beam time series. The black stars indicate the beams chosen for analysis. The two magenta stars correspond to the beams analyzed in Figures C-32 and C-33. (bottom left) Bathymetric map of the region with depth contours at 100, 200 and 300m. The grey and white diamonds correspond to the source and receiver, respectively. The black and magenta stars indicate the beams chosen for analysis. (bottom right) Polar plot of received normalized pressure with overlain bathymetric contours.

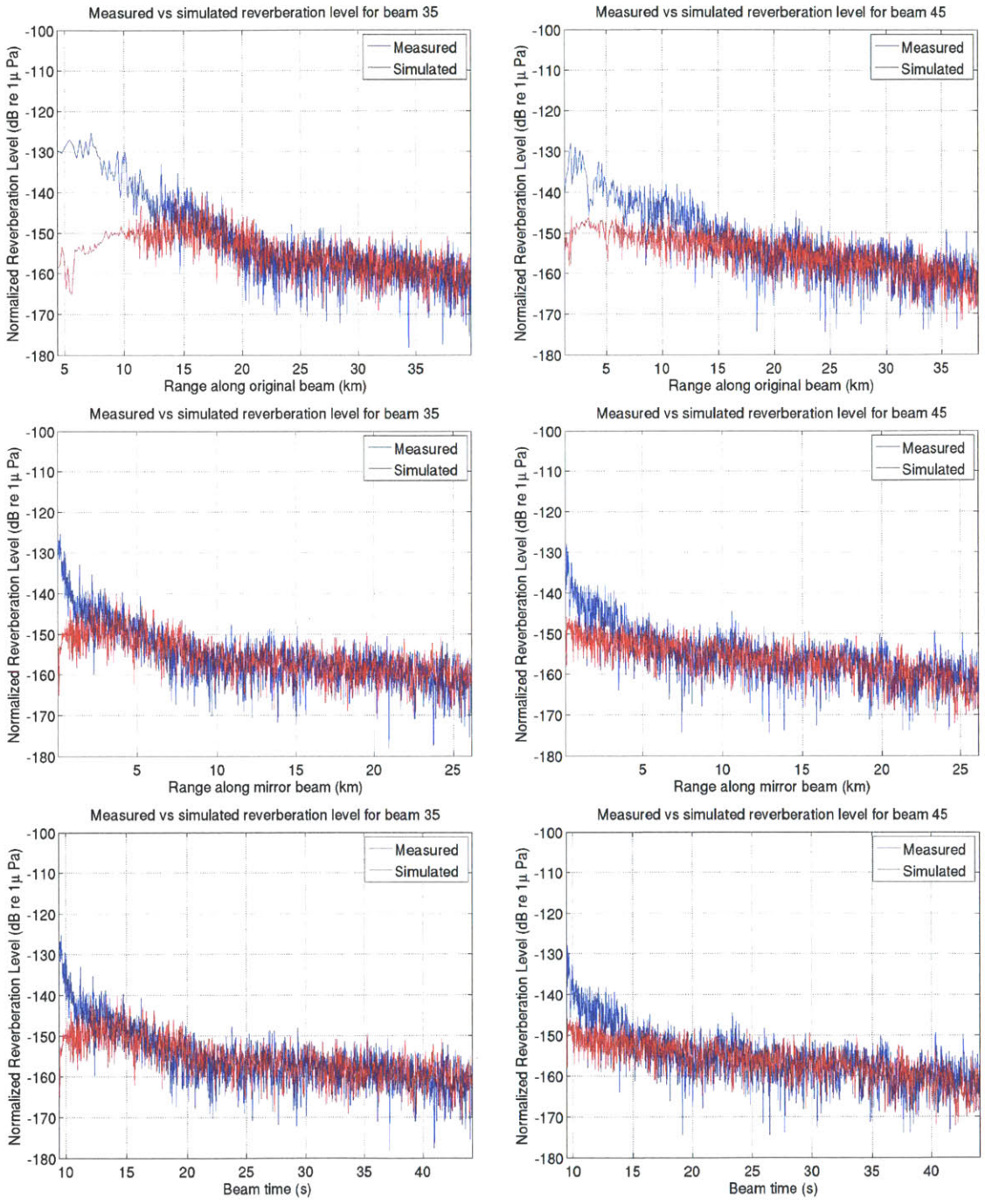

Figure C-32: Comparison of measured and simulated reverberation levels plotted against: beam time (top), range from the receiver along the original beam (middle), range from receiver along the mirror beam (bottom), for beams 35 and 45, indicated by magenta stars in Figure C-31 (top right).

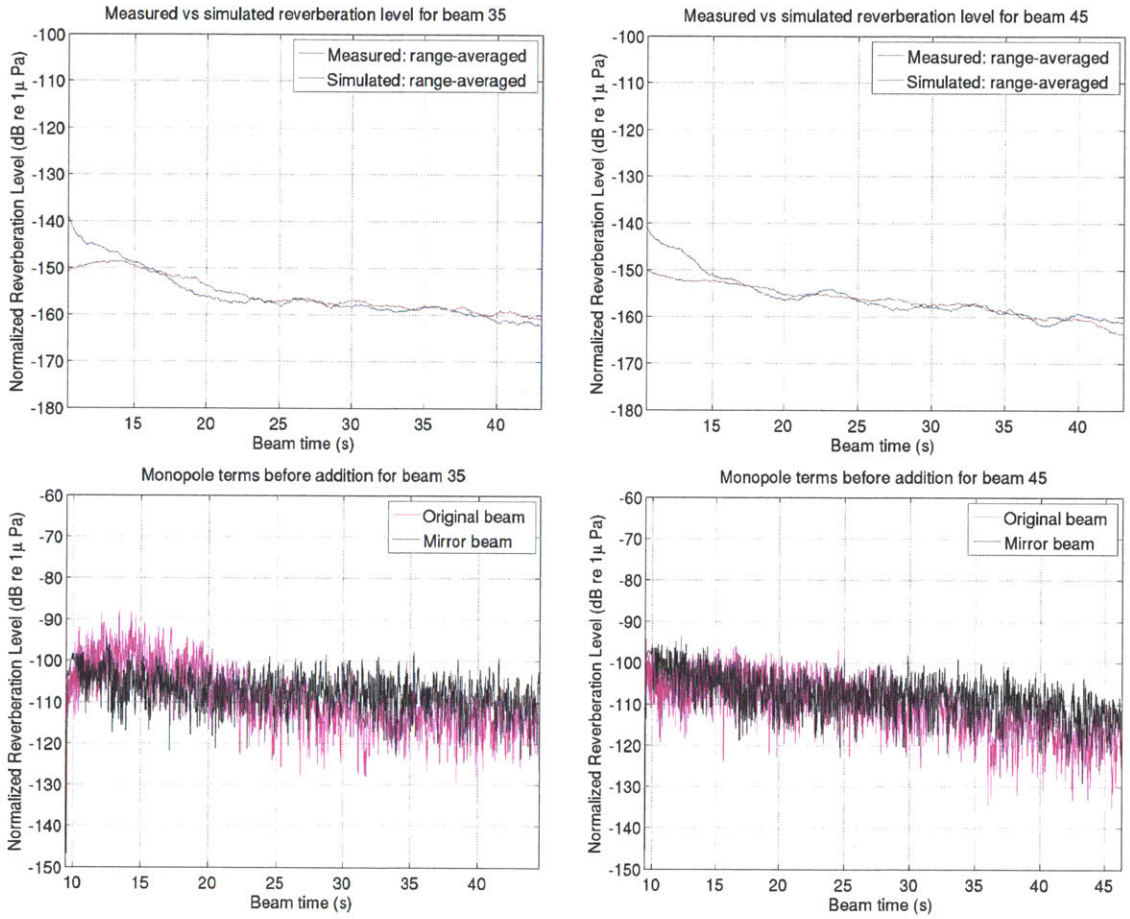

Figure C-33: For the same beams as in the previous figure C-32: comparison of measured and simulated reverberation time series after range/time averaging (top); comparison of the monopole term before adding the reverberation intensities for the original and mirror beams (bottom).

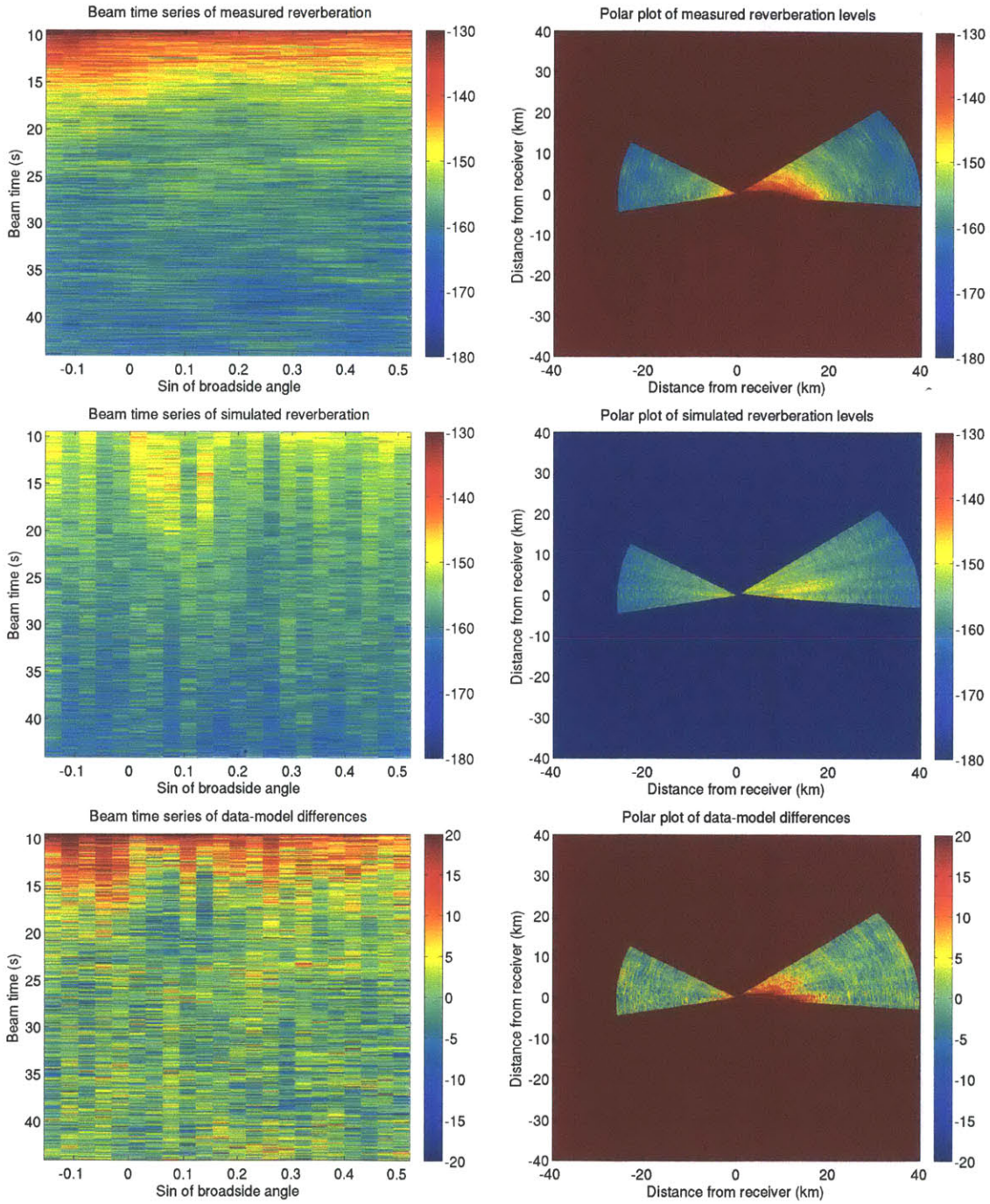

Figure C-34: Beam time (left) and polar (right) plots of measured reverberation level (top), simulated reverberation level (middle) and their difference (bottom).

Bibliography

[1] Mark Andrews. *Enabling high resolution population density imaging of random scatterer groups in a fluctuating range-dependent ocean waveguide with the matched filter variance.* PhD dissertation, Northeastern University, The Department of Electrical and Computer Engineering, December 2009.

[2] Mark Andrews, Tianrun Chen, and Purnima Ratilal. Empirical dependence of acoustic transmission scintillation statistics on bandwidth, frequency, and range in new jersey continental shelf. *The Journal of the Acoustical Society of America*, 125(1):111–124, 2009.

[3] Mark Andrews, Zheng Gong, and Purnima Ratilal. High resolution population density imaging of random scatterers with the matched filtered scattered field variance. *The Journal of the Acoustical Society of America*, 126(3):1057–1068, 2009.

[4] Homer P. Bucker. Wave propagation in a duct with boundary scattering (with application to a surface duct). *The Journal of the Acoustical Society of America*, 68(6):1768–1772, 1980.

[5] Michael D. Collins. A split-step pad[e-acute] solution for the parabolic equation method. *The Journal of the Acoustical Society of America*, 93(4):1736–1742, 1993.

[6] Ameya Galinde, Ninos Donabed, Mark Andrews, Sunwoong Lee, Nicholas C. Makris, and Purnima Ratilal. Range-dependent waveguide scattering model calibrated for bottom reverberation in a continental shelf environment. *The Journal of the Acoustical Society of America*, 123(3):1270–1281, 2008.

[7] John A. Goff, Barbara J. Kraft, Larry A. Mayer, Steven G. Schock, Christopher K. Sommerfield, Hilary C. Olson, Sean P. S. Gulick, and Sylvia Nordfjord. Seabed characterization on the new jersey middle and outer shelf: correlatability and spatial variability of seafloor sediment properties. *Marine Geology*, 209(1-4):147 - 172, 2004.

[8] Zheng Gong, Mark Andrews, Srinivasan Jagannathan, Ruben Patel, J. Michael Jech, Nicholas C. Makris, and Purnima Ratilal. Low-frequency target strength and abundance of shoaling atlantic herring (clupea harengus) in the gulf of maine

during the ocean acoustic waveguide remote sensing 2006 experiment. *The Journal of the Acoustical Society of America*, 127(1):104–123, 2010.

[9] Joseph Goodman. Speckle phenomena in optics. Roberts and Company Publishers, 2009.

[10] Paul C. Hines. Theoretical model of in-plane scatter from a smooth sediment seabed. *The Journal of the Acoustical Society of America*, 99(2):836–844, 1996.

[11] Kevin D. LePage and Henrik Schmidt. Spectral integral representations of monostatic backscattering from three-dimensional distributions of sediment volume inhomogeneities. *The Journal of the Acoustical Society of America*, 113(2):789–799, 2003.

[12] Dan Li, George V. Frisk, and Dajun Tang. Modeling of bottom backscattering from three-dimensional volume inhomogeneities and comparisons with experimental data. *The Journal of the Acoustical Society of America*, 109(4):1384–1397, 2001.

[13] N. C. Makris. Geoclutter acoustics experiment 2003 cruise report. Technical report, MIT, 2003.

[14] Nicholas C. Makris. The effect of saturated transmission scintillation on ocean acoustic intensity measurements. *The Journal of the Acoustical Society of America*, 100(2):769–783, 1996.

[15] Nicholas C. Makris, Purnima Ratilal, Srinivasan Jagannathan, Zheng Gong, Mark Andrews, Ioannis Bertsatos, Olav Rune God, Redwood W. Nero, and J. Michael Jech. Critical population density triggers rapid formation of vast oceanic fish shoals. *Science*, 323(5922):1734–1737, 2009.

[16] Nicholas C. Makris, Purnima Ratilal, Deanelle T. Symonds, Srinivasan Jagannathan, Sunwoong Lee, and Redwood W. Nero. Fish population and behavior revealed by instantaneous continental shelf-scale imaging. *Science*, 311(5761):660–663, 2006.

[17] H. M. Merklinger. Bottom reverberation measured with explosive charges fired deep in the ocean. *The Journal of the Acoustical Society of America*, 44(2):508–513, 1968.

[18] P. M. Morse and K. U. Ingard. Theoretical acoustics. Princeton University Press, NJ, 1986.

[19] Pierre D. Mourad and Darrell R. Jackson. A model/data comparison for low-frequency bottom backscatter. *The Journal of the Acoustical Society of America*, 94(1):344–358, 1993.

[20] Zhaohui Peng, Jixun Zhou, and Renhe Zhang. In-plane bistatic backward scattering from seabottom with randomly inhomogeneous sediment and rough interface. *Science in China Series G: Physics Mechanics and Astronomy*, 47:702–716, 2004. 10.1007/BF02687341.

[21] Purnima Ratilal and Nicholas C. Makris. A unified model for reverberation and submerged target scattering in shallow water. *The Journal of the Acoustical Society of America*, 107(5):2920–2920, 2000.

[22] R. J. Urick. Principles of underwater sound. McGraw Hill, New York, 1983.

[23] Tokuo Yamamoto. Acoustic scattering in the ocean from velocity and density fluctuations in the sediments. *The Journal of the Acoustical Society of America*, 99(2):866–879, 1996.